CUKUROVA UNIVERSITY
INSTITUTE OF NATURAL AND APPLIED SCIENCES

PhD THESIS

Ziyafer Gizem PORTAKAL

GEL-PHANTOM STUDY FOR TARGET VOLUME OPTIMIZATION IN HDR AND/OR LDR BRACHYTHERAPY USING ADVANCED IMAGING TECHNIQUES

DEPARTMENT OF PHYSICS

ADANA-2018

CUKUROVA UNIVERSITY
INSTITUTE OF NATURAL AND APPLIED SCIENCES

GEL-PHANTOM STUDY FOR TARGET VOLUME OPTIMIZATION IN HDR AND/OR LDR BRACHYTHERAPY USING ADVANCED IMAGING TECHNIQUES

Ziyafer Gizem PORTAKAL

PhD THESIS

DEPARTMENT OF PHYSICS

We certify that the thesis titled above was reviewed and approved for the award of degree of the Doctor of Philosophy by the board of jury on 21/09/2018.

……...	……...	……...
Prof.Dr. Mustafa TOPAKSU	Prof.Dr. Şule AYTAŞ	Prof.Dr. Ayşe POLATÖZ
SUPERVISOR	MEMBER	MEMBER
……...	……	
Prof.Dr. Sefa ERTÜRK	Prof.Dr. Eyyüp TEL	
MEMBER	MEMBER	

This PhD Thesis is performed in Department of Physics of Institute of Natural and Applied Sciences of Çukurova University.
Registration Number:

Prof. Dr. Mustafa GÖK
Director
Institute of Basic and Applied Sciences

This Study was supported by Çukurova University Scientific Research Fund.
Project Number: FDK-2014-2709

DEDICATION

This PhD thesis is dedicated to my late grandfather Hasan Vecihi BAĞRIYANIK who was my first teacher, idol and the person I love most. Maybe he could not see but if he is watching me somewhere up there, I would like to say him; "Grandpa, I am not a student anymore! I made it!"

ABSTRACT

PhD THESIS

GEL-PHANTOM STUDY FOR TARGET VOLUME OPTIMIZATION IN HDR AND/OR LDR BRACHYTHERAPY USING ADVANCED IMAGING TECHNIQUES

Ziyafer Gizem PORTAKAL

ÇUKUROVA UNIVERSITY
INSTITUTE OF NATURAL AND APPLIED SCIENCES
DEPARTMENT OF PHYSICS

Supervisor : Prof.Dr. Mustafa TOPAKSU
Co. Supervisor : Assoc.Prof.Dr. Nina TUNÇEL
Year: 2018, Pages: 117
Jury : Prof.Dr. Mustafa TOPAKSU
Prof.Dr. Ayşe POLATÖZ
: Prof.Dr. Şule AYTAŞ
: Prof.Dr. Eyyüp TEL
: Prof.Dr. Sefa ERTÜRK

In this thesis, agar, agarose, and polyvinyl alcohol cryogel phantoms with concentrations ranging from 1.0% to 3.5%, 0.5% to 3.0%, and 10% to 20%, respectively, were prepared to create tissue-mimicking gel phantoms convenient for Diffusion Kurtosis Imaging (DKI) in order to develop proper sequences for target volume optimization in High Dose Rate (HDR) and/or Low Dose Rate (LDR) brachytherapy. The kurtosis values of the gels increased with the concentration but they were too low to mimic values for various tissues when created purely. Therefore, glass microspheres were added into the gels at different concentrations to create tissue-mimicking phantoms with more realistic kurtosis values. Diffusion coefficients (ADC or $D_{(1)}$ and $D_{(2)}$), excess kurtosis (K) values, and relaxation parameters were experimentally determined and the kurtosis values for the plain gels ranged from 0.05 (0.029, 0.071) to 0.216 (0.185, 0.246) with 95% confidence interval (CI). Inclusion of glass microspheres increased the kurtosis with values up to 0.523 (0.465, 0.581) observed for gels with the highest concentration of microspheres. The presence of glass microspheres reduced ADCs and increased the transverse and longitudinal relaxation rates. Phantoms were also evaluated for the further physical parameters using X-ray Computed Tomography (CT) and Ultrasound (US) elastography. The study shows that agar gels including glass microspheres in particular are encouraging materials as low-cost and durable phantoms for Diffusion Weighted-Magnetic Resonance Imaging (DW-MRI) and DKI with tuneable diffusion and relaxation properties.

Keywords: Magnetic Resonance Imaging, Diffusion Kurtosis Imaging, Non-Gaussian Diffusion, Gel Phantom, Brachytherapy.

ÖZ

DOKTORA TEZİ

İLERİ GÖRÜNTÜLEME TEKNİKLERİ KULLANARAK HDR VE/VEYA LDR BRAKİTERAPİDE HEDEF HACİM OPTİMİZASYONU İÇİN JEL FANTOM ÇALIŞMASI

Ziyafer Gizem PORTAKAL

ÇUKUROVA ÜNİVERSİTESİ
FEN BİLİMLERİ ENSTİTÜSÜ
FİZİK ANABİLİM DALI

Danışman : Prof.Dr. Mustafa TOPAKSU
İkinci Danışman : Doç.Dr. Nina TUNÇEL
Yıl: 2018, Sayfa: 117
Jüri : Prof.Dr. Mustafa TOPAKSU
Prof.Dr. Ayşe POLATÖZ
: Prof.Dr. Şule AYTAŞ
: Prof.Dr. Eyyüp TEL
: Prof.Dr. Sefa ERTÜRK

Bu tez çalışmasında, Yüksek Doz Hızlı (HDR) ve/veya Düşük Doz Hızlı (LDR) brakiterapide hedef hacim optimizasyonunu sağlamada uygun sekanslar geliştirmek amacıyla Difüzyon Kurtosis Görüntülemeye (DKI) uygun doku benzeri jel fantomları oluşturmak için konsantrasyonları sırasıyla %1,0 ile %3,5; %0,5 ile %3,0 ve %10 ile %20 arasında değişen agar, agaroz ve polivinil alkol kriyojel fantomlar hazırlanmıştır. Jellerin kurtosis değerleri konsantrasyonla artsa da saf olarak hazırlandıklarında çeşitli doku değerlerini yansıtmada oldukça düşük kalmıştır. Bu nedenle, daha gerçekçi kurtosis değerleri ile dokuyu yansıtan fantomlar oluşturmak için farklı konsantrasyonlardaki jellere cam mikroküreler eklenmiştir. Difüzyon katsayıları (ADC ya da $D_{(1)}$ ve $D_{(2)}$), ilave kurtosis (K) değerleri ve relaksasyon parametreleri deneysel olarak belirlenmiş ve katkısız jeller için kurtosis değerleri %95 güven aralığıyla 0,05 (0,029; 0,071) ile 0,216 (0,185; 0,246) aralığında çıkmıştır. Cam mikrokürelerin eklenmesi kurtosis değerini, en yüksek mikroküreler içeren jeller için gözlenen 0,523 (0,465; 0,581) değerine kadar arttırmıştır. Cam mikrokürelerin varlığı ADC değerlerini azaltmış, boylamsal ve enine relaksasyon hızlarını arttırmıştır. Fantomlar ayrıca X-ışını Bilgisayarlı Tomografi ve Ultrason elastografi kullanılarak fiziksel parametreleri açısından değerlendirilmiştir. Çalışma, cam mikrokürelere sahip agar jellerinin, ayarlanabilir difüzyon ve relaksasyon özelliklerine sahip Difüzyon Ağırlıklı Manyetik Rezonans Görüntüleme (DW-MRI) ve DKI için ucuz ve dayanıklı fantomlar olarak ümit verici materyaller olduğunu göstermektedir.

Anahtar Kelimeler: Manyetik Rezonans Görüntüleme, Difüzyon Kurtosis Görüntüleme, Gaussian Olmayan Difüzyon, Jel Fantom, Brakiterapi.

EXTENDED SUMMARY

During the past several years, imaging has been the most important influence enabling the development of better Brachytherapy (BT) treatments. Since MRI, CT, and US techniques are used before and during the treatment, great importance is attached to the development of these techniques in increasing target volume and organ at risk (OAR) optimization. DKI provides more information on tissue structure since it uses a polynomial model rather than monoexponential Gaussian model used as in standard DW-MRI.

First, it is essential to prepare tissue-mimicking, durable, simple, and feasible phantoms to carry out quality assurance studies and to develop and evaluate novel pulse sequences in DW-MRI and DKI. To investigate the adaptability of the developed and investigated techniques to BT patients, different MR devices, magnetic field strength, and scaning protocols should be tested beforehand. Additionally, DKI is sensitive to the impact of signal noise by caused by strong diffusion weightings and higher order modelling of the diffusion-weighted signal, which must be considered to obtain accurate values. It is crucial to prevent artificially magnified kurtosis estimates by avoiding the noise floor, which is called pseudo-kurtosis. Therefore, noise reduction studies should be carried out. Finally, physical parameters of phantoms should be determined by examining their usability in other advanced imaging techniques (US, CT, etc) used in BT.

In this thesis, agar, agarose, and polyvinyl cryogel (PVA-C) phantoms were manufactured in various concentrations, volumes and forms to mimic different tissues. Furthermore, in order to prepare more realistic tissue-mimicking phantoms, kurtosis values, diffusion coefficients and relaxation parameters were obtained and the effects of glass microspheres on diffusion were evaluated by creating agar and agarose gel phantoms with glass microsphere addition. An antimicrobial preservative (diazolidinyl urea) was added to increase the durability of the phantoms, and endurance and homogeneity tests were performed.

Subsequently, new sequences were prepared and evaluated for each phantom. The noise level is identified by determining the Signal-to-Noise Ratio (SNR) to avoid noise floor. All DW-MRI and DKI measurements were performed by Siemens 3T Magnetom Skyra and GE 1.5T Optima MR450w using a single-shot spin-echo echo-planar-imaging (SS-SE-EPI) sequence and a version of the Stejskal-Tanner spin-echo (ST-SE) sequence, which does not use single short EPI readout. To assess the relaxation properties of the phantoms, vendor-supplied SE sequences with different echo (T_E) and repetition (T_R) times were used respectively. Finally, the mechanical properties of phantoms have been examined by US/Elastography method, which has been recently applied during BT treatment as another advanced imaging technique. Each phantom was scaned in CT and Hounsfield Unit (HU) values were determined.

In the first stage, as the concentration of gel phantom prepared increased, diffusion coefficients of $D_{(1)}$ (or ADC) and $D_{(2)}$ showed a tendency to decrease or stay constant but kurtosis values increased. Maximum kurtosis values obtained in prepared homogeneous plain phantoms were found as 0.216, 0.137, and 0.207 for agar, agarose, and PVA-C, respectively and these values were inadequate and low when compared with the actual patient data in the literature. Although, it is likely that some of the values reported were artificially inflated due to pseudo-kurtosis. Significant decreases in $D_{(1)}$ and $D_{(2)}$ diffusion coefficients were observed with the addition of glass microspheres at different concentrations to the gels prepared with different concentration of gelling agent, whereas significant increases were observed in kurtosis values up to 0.523 for agar and 0.289 for agarose. While natural materials, such as agar and agarose, do not interact with glass microspheres, PVA-C phantoms have not been used for the further investigation phase since the artificial material PVA interacts with the glass microspheres by forming a different structure. Comparing kurtosis values achieved in this study with published kurtosis values for healthy and deceased tissue, agar with suitable additives seems to be the most appropriate gelling agent.

Characterization of the gel phantoms using relaxometry to quantify the effect of the glass microspheres on the T_1 (spin-lattice) and T_2 (spin-spin) times suggested that high microsphere concentrations tend to modify the relaxation times/rates slightly. The relaxation times were appropriate for tissue-mimicking phantoms and they could easily be controlled by varying the concentration of gelling agents or the addition of T_1 or T_2 contrast agents. T_1 decreased almost linearly with the concentration of the gelling agent for all plain phantoms. T_2 also decreased in a non-linear fashion as a function of the concentration for each gel phantom. Thus, R_2 ($1/T_2$) plots were drawn to evaluate the data and it was seen that R_2 increases almost linearly for each gelling agent, as expected. While T_2 decreased for each gelling agent, T_1 decreased for agar but increased only slightly for agarose gel phantoms as a function of glass microsphere concentration. The observed range of T_2 times are appropriate to model a range of tissue. However, it was seen that T_1 times were found close to the soft tissue with agar and PVA gels but very different for agarose gels.

The "wave propagation speed (m/s)" and "Young Module (kPa)" of agar, agarose and PVA-C phantoms were determined by US/Elastography technique, which provides qualitative and quantitative analysis as one of the advanced technologies used during the application of BT treatment. Firstly, plain phantoms were investigated and the agar phantoms were found to give better results than the others. As the concentration increases, both wave propagation speed and Young Module increase. One prepared agar phantom with glass microspheres was also evaluated and it was found that the addition of glass microspheres did not affect numerical data. On the other hand, neither the image quality nor the elasticity values showed successful results in other gel phantoms. For this reason, a new heterogeneous agar test phantom with 2.0% agar background and 3.5% agar cylindrical inclusion was created to evaluate its visualization and usability for ultrasonic modalities and a successful scan image was taken.

Each phantom was scanned by two different CTs and their Hounsfield Unit (HU) values were analyzed using ImageJ software. When each geling agent was evaluated separately, HU values increased as the concentration increases. HU values of agar and agarose gels were very close to water, since they are natural materials (obtained from the cell wall of algae) and can be used in small quantities to form gels. However, since PVA-C is an artificial gelling agent and used in relatively large quantities, HU values were higher but similar to many soft tissues. The aim of this study is not to represent these HU values for a specific tissue or organ, but to determine how HU values change depending on the concentration of gelling agent and microspheres when microspheres are added. Likewise, HU values are significantly reduced and in fact negative with the addition of microspheres because the majority of the microsphere volume is air.

When the durability of the gel phantoms was examined, the results also showed that agar and agarose phantoms are successful materials as gelling agents. PVA-C phantoms have an important disadvantage in terms of their usage availability since they release water at room temperature (RT) during the process.

To increase the success of methods based on the use of advanced imaging techniques such as focused/focal BT, tissue-mimicking gel phantoms especially specific for DKI were designed and this study suggest that agar phantoms give the best results for this purpose. In this thesis, it can be easily seen that the produced phantoms can serve multiple purposes for multimodal imaging techniques since they are cheap, simple to prepare, and durable. This allows the development of imaging techniques to better identify the organs at risk and diseased tissue for the application of the treatment techniques such as HDR or LDR Brachytherapy. The phantoms developed and characterized in this thesis are novel and can be used for the development of new puls sequences and diagnostic techiques.

GENİŞLETİLMİŞ ÖZET

Geçtiğimiz bir kaç yıl boyunca, brakiterapi (BT) tedavilerindeki gelişmelerin hızlanmasını sağlayan en önemli etki görüntüleme olmuştur. Tedavi öncesinde ve sırasında MRI, CT ve US teknikleri kullanıldığı için, hedef hacim ve kritik organ (OAR) optimizasyonunun arttırılmasında bu tekniklerin geliştirilmesine büyük önem verilmektedir. DKI, bir polinom modeli kullanarak standart DW-MRI'da kullanılan tekil eksponansiyel Gauss modeline göre doku yapısı hakkında daha fazla bilgi sağlamaktadır.

Öncelikle, DW-MRI ve DKI'da kalite kontrol çalışmaları, yeni puls sekanslarını geliştirme ve değerlendirme çalışmaları yapabilmek için dokuyu temsil edebilecek, dayanıklı, basit ve pratik fantomların hazırlanması gerekmektedir. Geliştirilen ve incelenen tekniklerinin BT hastalarına adapte edilebilirliğini irdelemek için bu aşamada farklı cihaz, manyetik alan şiddeti, tarama protokolleri uygulanarak test edilmelidir. Ek olarak, DKI doğru değerleri elde etmek için dikkate alınması gereken difüzyon ağırlıklı sinyalin daha yüksek düzeyli modellemesi ve güçlü difüzyon ağırlıklarına bağlı olarak sinyal gürültüsünün etkilerine duyarlıdır. Psödo (sahte)-kurtosis olarak adlandırılan, yapay olarak şişirilmiş kurtosis tahminlerini önlemek için gürültü tabanından uzak durmak önemlidir. Bu nedenle de, gürültü giderme çalışmaları yapılmalıdır. Son olarak ise, BT'de kullanılan diğer görüntüleme tekniklerinde kullanılabilirliklerini inceleyerek (US, CT, vb) fiziksel parametreleri belirlenmelidir.

Bu tezde, farklı dokuları temsil edebilmeleri amacıyla çeşitli konsantrasyonlar, hacim ve şekillerde agar, agaroz ve polivinil alkol kriyojel (PVA-C) fantomları oluşturulmuştur. Ayrıca daha gerçekçi doku benzeri fantomların hazırlanabilmesi amacıyla farklı konsantrasyonlarda cam mikrokürecik ilaveli agar ve agaroz jel fantomları da hazırlanarak kurtosis değerleri, difüzyon katsayıları ve relaksasyon (gevşeme) parametreleri elde edilmiş ve mikroküreciklerin difüzyon üzerindeki etkileri değerlendirilmiştir. Fantomların

dayanıklığını arttırabilmek amacıyla antimikrobiyal koruyucu (diazolidinil üre) eklenmiş, ayrıca fantomların dayanıklılık ve homojenite testleri yapılmıştır. Akabinde, yeni sekans hazırlanarak karakterize edilen her bir fantom için değerlendirilmiştir. Gürültü duvarının fitlenmesinden kaçınmak için gürültü seviyesi sinyal-gürültü oranı (SNR) belirlenerek karakterize edilmiştir. Tüm DW-MRI ve DKI ölçümleri Siemens 3T Magnetom Skyra ve GE 1,5T Optima MR450w cihazlarında single-shot spin-echo Echo-planar-imaging (SS-SE-EPI) sekansı ile tek ve kısa EPI okumasını kullanmayan Stejskal-Tanner spin-echo (ST-SE) sekansının bir uyarlaması kullanılarak gerçekleştirilmiştir. Fantomların relaksasyon özelliklerini değerlendirmek için sırasıyla farklı eko (T_E) ve tekrarlanma (T_R) süreleri olan SE sekansları kullanılmıştır. Son olarak da diğer bir gelişmiş görüntleme tekniği olarak BT tedavisi esnasında yeni uygulanmaya başlayan US/Elastografi yöntemi ile fantomlarının mekanik özelliklerine bakılmıştır. Her bir fantomun CT'de görüntüsü alınarak Hounsfield Unit (HU) değerleri belirlenmiştir.

Ilk etapta gözlenen, hazırlanan jel pantomun konsantrasyonu arttırıldıkça $D_{(1)}$ (ya da ADC) ve $D_{(2)}$ difüzyon katsayılarının düşme ya da sabit kalma eğilimi gösterirken kurtosis değerlerinin artması olmuştur. Sade olan fantomlarda maksimum kurtosis değeri agar için 0,216; agaroz için 0,137 ve PVA-C için 0,207 olarak bulunmuştur ve bu değerler literaturdeki gerçek hasta verileriyle karşılaştırıldığında oldukça yetersiz ve düşük kalmışlardır. Fakat literatürdeki bu verilerin genellikle psedö-kurtosis'e maruz kaldığı da göz ardı edilmemelidir. Farklı konsantrasyonlardaki jellere yine farklı konsantrasyonlarda cam mikrokreciklerin ilavesiyle birlikte $D_{(1)}$ ve $D_{(2)}$ difüzyon katsayılarında ciddi düşüşler gözlemlenirken, kurtosise bakıldığında agar için 0,523; agaroz için 0,289 değerine kadar artışlar gözlenmiştir. Agar ve agaroz doğal malzemeleri cam mikrokürecikle etkileşmezken, yapay bir malzeme olan PVA etkileşerek farklı bir yapı oluşturduğundan ilave araştırma aşamasında kullanılmamıştır. Literatürdeki sağlıklı ve hastalıklı dokuların kurtosis değerlerine bakıldığında, DKI için agarın

diğer iki malzemeye göre fantom ana malzemesi olarak daha kullanışlı olduğu söylenebilmektedir.

Cam mikroküreciklerin T_1 (spin-örgü) ve T_2 (spin-spin) relaksasyon zamanları üzerindeki etkisini ölçmek için relaksometri kullanılarak jel fantomlar karakterize edildiğinde, yüksek mikrokrecik konsantrasyonunun gevşeme sürelerini/hızlarını hafifçe değiştirmeye eğilimli olduğu görülmüştür. Gevşeme süreleri dokuyu taklit eden fantomlar için uygundur ve jelleştirici madde konsantrasyonu veya kullanılan katkı maddelerinin düzenlenmesiyle kolaylıkla kontrol edilebilmektedir. T_1, tüm sade fantomlar için jelleştirici maddenin konsantrasyonu ile neredeyse doğrusal olarak azalmıştır. T_2 de, her bir jel fantomu için konsantrasyonun bir fonksiyonu olarak, doğrusal olmayan bir şekilde azalmıştır. Bu nedenle, verileri değerlendirmek için R_2 ($1/T_2$) grafikleri çizilmiş ve R_2'nin, beklendiği gibi her bir jelleştirme maddesi için neredeyse doğrusal olarak arttığı görülmüştür. Her bir jelleştirme maddesi için cam mikrokürecik konsantrasyonunun bir fonksiyonu olarak T_2 azalırken, T_1 agar için azalmış, ancak agaroz için artarmıştır. Tüm jel fantomların T_2 zaman aralığı yumuşak dokuyu temsil edebilmektedir. Bununla birlikte, agar ve PVA jellerinin T_1 sürelerinin yumuşak dokuya yakın olduğu, ancak agarozunkilerin çok farklı olduğu görülmüştür. BT tedavisinin uygulanması esnasında kullanılan ve gelişmiş teknolojilerden biri olarak kalitatif ve kantitatif analiz yapma olanağı sunan US/Elastografi tekniği ile agar, agaroz ve PVA-C fantomlarının “dalga yayılma hızı (m/s)” ve “Young Modülü (kPa)” belirlenmiştir. Öncelikli olarak ilavesiz hazırlanmış fantomlar değerlendirilmiş ve diğerlerine göre agar fantomların daha iyi değerler verdikleri görülmüştür. Konsantrasyon arttıkça hem dalganın yayılma hızı hem de Young Modülü artmıştır. Hazırlanan bir cam mikrokürecikli agar fantom da değerlendirilmiş ve cam mikroküre ilavesinin sayısal verileri etkilemediği bulunmuştur. Diğer fantomlarda ise gerek görüntü kalitesi gerekse sayısal veriler başarılı sonuçlar vermemiştir. Bu nedenle ilave test etmek amacıyla dış yüzeyi %2,0 agar ve içinde %3,5 konsantrasyonunda silindirik agar yapı içeren

yeni bir heterojen agar fantom hazırlanmış ve başarılı bir tarama görüntüsü alınmıştır. Her bir fantom iki farklı CT'de taranmış ve HU değerleri ImageJ yazılımı kullanılarak analiz edilmiştir. Her bir jel malzemesi için ayrı ayrı değerlendirildiğinde konsantrasyon arttıkça HU değerleri de yükselmiştir. Agar ve agaroz doğal malzemeler (alglerin hücre duvarından elde edilirler) olduklarından ve jel oluşturmak için az miktarda kullanımlarının yeterli olmasından dolayı HU değerleri suya çok yakın çıkmıştır. Fakat PVA-C yapay bir malzeme ve nispeten daha fazla miktarda kullanıldığından HU değerleri de daha yüksek ve hatta pek çok yumuşak dokuya benzer çıkmıştır. Burada amaç bu değerlerin spesifik bir doku ya da organı temsil etmesi değil, konsantrasyon ve mikrokürecik kullanımına bağlı olarak HU değerlerinin ne ölçüde değiştiğini belirlemektir. Keza mikrokürecik ilavesi ile HU değerleri oldukça azalmış (eksilere düşmüş) bunun nedeninin de küreciklerin hacminin büyük bir çoğunluğunun hava olduğu ifade edilmiştir.

Fantomların dayanıklılık özellikleri de incelendiğinde, özellikle agar ve agaroz fantomların başarılı malzemeler olduklarını göstermiştir. PVA-C fantomlarının zamana bağlı olarak su salınımı yapmaya başlamaları kullanılabilirlikleri açısından bir dezavantaj olmaktadır. Odaklı BT tedavisi gibi ileri görüntüleme tekniklerinin kullanımına dayanan yöntemlerde başarıyı arttırabilmek amacıyla özellikle DKI tekniğine spesifik dokuyu temsil edebilecek jel fantomlar tasarlanmış ve en başarılı sonuçları agar fantomlarının verdiği bulunmuştur. Bu tez çalışmasında, üretilen fantomların ucuz, basit hazırlanabilir ve dayanıklı olmaları nedeniyle pek çok görüntüleme tekniği için çoklu amaçlara hizmet edebileceği gösterilmiştir. Bu da HDR veya LDR brakiterapi gibi tedavi tekniklerinin uygulanmasında gerek kritik organ gerekse hedef hacmin daha iyi teşhis edilebilmesine olanak sağlayan görüntüleme tekniklerin geliştirilmesine olanak sağlamaktadır. Bu çalışma ile literatürde ilk defa DKI ve diğer gelişmiş görüntüleme tekniklerine uyumlu jel fantomlar hazırlanmış olup, karakterize edilmiş ve sekans geliştirilmesi sağlanarak gerçek hasta teşhisinde kullanılmak üzere ileri çalışmalar yapılmasına olanak sağlanmıştır.

ACKNOWLEDGMENTS

I would like to thank my PhD supervisors, Prof. Dr. Mustafa Topaksu and Assoc. Prof. Dr. Nina Tunçel, for supporting me during this thesis period. Dr. Topaksu is a person you will immediately love and never forget once you meet him. He is one of the most positive, knowledgeable, helpful and understanding academician I know. Dr. Tunçel has been supportive and has given me the freedom to pursue this work without objection. I am also very grateful to Dr. Tunçel for her scientific advice and knowledge.

I also have to thank the members of my PhD committee, Professors Ayşe Polatöz and Şule Aytaş for their helpful career advice and suggestions in general. I will forever be thankful to Dr. Aytaş being my best role model for a scientist, mentor, and teacher. I would like to thank Prof. Dr. Sefa Ertürk helping me during my thesis writing for his valuable support. I thank Prof. Dr. Zehra Yeğingil for the opportunities she provided when I entered this field thanks to her.

I am grateful to my international advisor for this thesis project, Dr. Emiliano Spezi for accepting me as a Visiting Research Scholar at Velindre Cancer Centre during a year enable me to work on medical imaging and brachytherapy. I owe a great debt of gratitude to all the mentors, contributors, and colleagues, Dr. Jon Phillips and Dr. Sophie Shermer, Teresa Perrett, Jane Flewitt, Dr. Leo James Garcia, Andrew Edwards, Dr. Jacqueline Shipley and Prof. Dr. Geraint Lewis. Dr. Phillips and Dr. Shermer have worked with me without a break during the day and night and even on weekends so that the thesis work could be successfully completed. I am grateful for their patience and belief. I have learned a lot from them.

A good working group is of great importance during an academic life and I was lucky to be a part of one with Dr. Tamer Doğan, Dr. Mehmet Yüksel, Dr. Sibel Akça and Sümeyra Balcı-Yegen under the direction of Dr. Topaksu. Sibel is an excellent, honest and helpful friend who has been through a lot and I am amazed of her positive outlook and ability to smile despite the situation. I can never skip the moral support of my dear friends, Dr. Serdal Damarseçkin, Dr. Nur Kıcır, Dr. Neslihan Sarıgül, E. Burçin İspir-Aydınlıoğlu, and lovely Diray Oran-Önçağ.

I would like to thank the Scientific and Technological Research Council of Turkey (TUBITAK) for supporting me under 2214/A program during the visiting period in Cardiff, Wales and Research Funding Projects Unit in Çukurova University for their support to this PhD thesis under the project no. FDK-2014-2709.

Finally yet importantly, I would like to express my deepest thanks to my family, Berna, Ümit, and Görkem Portakal for their endless love and support.

CONTENTS **PAGE**

LIST OF TABLES **PAGE**

LIST OF FIGURES **PAGE**

ABBREVIATIONS

2D	: Two dimensional
3D	: Three dimensional
ADC	: Apparent diffusion coefficient
BT	: Brachytherapy
CI	: Confidence interval
CT	: X-ray computed tomography
DICOM	: Digital imaging and communications in medicine
DWI	: Diffusion weighted imaging
DW-MRI	: Diffusion weighted – magnetic resonance imaging
DKI	: Diffusion kurtosis imaging
DTI	: Diffusion tensor imaging
DU	: Diazolidinyl urea
EPI	: Echo planar imaging
FOV	: Field of view
FT	: Freeze-thaw
GRE	: Gradient-echo
HDR	: High dose rate
K	: Kurtosis
LDR	: Low dose rate
MRI	: Magnetic resonance imaging
NMR	: Nuclear magnetic resonance
OAR	: Organ at risk
PGSE	: Pulsed gradient spin-echo
PVA-C	: Polyvinyl alcohol cryogel
QA	: Quality assurance
QC	: Quality control

RF	: Radio frequency
RT	: Room temperature
ROI	: Region of interest
SD	: Standard deviation
SE	: Spin-echo
SNR	: Signal to noise ratio
SS	: Single-shot
SWE	: Shear wave elastography
TE	: Echo time
TR	: Repetition time
US	: Ultrasound

1. INTRODUCTION

1.1. General Remarks

Cancer management has been used successfully giving great advantages since the 1960s and the importance of brachytherapy has increased gradually since then. Brachytherapy used to be unpopular for many years, mainly due to radiation hazards to users and those associated with the treatment of patients before 1960s, but since then important progress was made with the development of afterloading machines. There have been major advances in imaging technologies and computerized planning parallel to the technological advances in afterloading machines (Joslin et al., 2001).

For safe and accurate brachytherapy treatment, the most important part is to define the tumour accurately. Identifying the location of the tumour within the organ would provide better targeting of the tumour for treatment. Thus far, the application of the advanced imaging techniques has been confined to use at the time of diagnosis but it is the intention of this thesis study to look at the feasibility of evaluating these modalities to increase image quality. Using advanced imaging techniques during the brachytherapy procedure itself can aid the delineation of the target volume and identifying the tumour within it.

Present accord recommendations for High Dose Rate (HDR) (Erickson et al., 2011) and Low Dose Rate (LDR) (Davis et al., 2012; Rosenthal et al., 2011) brachytherapy include Magnetic Resonance Imaging (MRI) alongside Transrectal Ultrasound (TRUS) and X-ray Computed Tomography (CT). Obtaining a 3D data set using CT and/or MRI has provided better dose specification and more precise planning to the volumes of both the organs at risk (OARs) and the tumour. MRI has the advantage of having good soft tissue contrast and thus can distinguish between tumour and normal tissue (Lee, 2014) as a useful diagnostic tool for staging and selection of convenient therapies for cervical cancers, prostate, etc (Stafford et al., 2016; Tanderup et al., 2014). As an integral component of the multi

parametric MRI examination, Diffusion Weighted MRI (DW-MRI) examines the tissue structure at the microscopic scale of water self-diffusion (Brownian motion). Furthermore, Diffusion Kurtosis Imaging (DKI) potentially supplies more information on tissue structure by using a better model for the characteristic signal attenuation in DWI (Jensen et al., 2005). Since DKI was introduced, it has been applied in vivo in many cases compared to standard DW-MRI (Barrett et al., 2017; Raab et al., 2010; Jansen et al., 2010; Nogueira et al., 2014; Trampel et al., 2006). The application of such a new and promising model for the treatment will increase the accuracy of both diagnosis and treatment.

The assessment of the appropriate scanning sequence for DKI involves the construction of gel phantoms. It is easier and more practical to design the optimal phantom to be able to represent the patient before implementing the best model. As with all quantitative imaging modalities, it is important to use tissue-mimicking and durable phantoms for quality control assessments and examining the utility of novel pulse sequences for DW-MRI and DKI as well as validating their effectiveness at high field strengths (Phillips and Charles-Edwards, 2015; Lavdas et al., 2013). Imaging phantoms are useful for calibration and checking of equipment, development of new systems and sequences, and training of operators.

It is also necessary to test the physical properties of imaging phantoms to determine their suitability for the purpose of usage. Elastic parameters and CT numbers of the phantoms can be useful to include in a detailed characterization. Although there are many methods to determine elastic parameters, the recent developments of ultrasonography make it one of the preferred methods especially since it can also be used during brachytherapy treatment (e.g., prostate). Ultrasound (US) Elastography is another unique modality being the subject of active research for clinical applications, primarily prostate and breast lesion imaging before and during the brachytherapy treatment. It is used to measure relative tissue stiffness exploiting tha fact that tumours are usually stiffer (Ginat et al., 2009).

1.2. The Purpose of the Thesis

The purpose of this study is to create tissue-mimicking gel phantoms convenient especially in DKI by characterizing and optimizing the apparent diffusion coefficients (ADCs) and kurtosis values of agar, agarose and polyvinyl alcohol cryogel (PVA-C) phantoms for cancer patients treated by HDR and LDR BT. Characterization, protocol optimization, and sequence development studies on phantoms were executed to increase target volume optimization for BT patients as well as using other imaging modalities (CT and US/Elastography).

In brief, it is aimed to prepare phantoms suitable for advanced imaging techniques used for diagnostic purposes prior to BT treatment and to provide more accurate dose delivery by optimizing the target volume during the treatment.

1.3. Background Information

1.3.1. HDR and LDR Brachytherapy

Radiotherapy is one of the most effecient methods used in combination with surgery and chemotherapy in cancer treatment. It is applied as "external beam radiation therapy (EBRT)" or "internal radiation therapy, brachytherapy (BT)". EBRT is a technique that uses high-energy photon, electron or proton/carbon beams directed to the patient in many directions from outside, while brachytherapy is a technique based on treating the tumour with permanent implants, temporary applicators, or radioactive sources placed with afterloading catheters inside the body of the patient (Joslin, 2001). Brachy means “short-distance” as a Greek word. BT is divided into various sub-treatment modalities depending on the type and application of treatment, as well as being used commonly in the treatment of prostate, breast and gynecological cancers.

These types of BT can be classified according to the chacteristics of source placement, duration and dose rate (Nath, 2005; Holm, 2013; Brady et al., 2016).

- According to source placement; intracavitary, interstitial, intraluminal, intravascular BT, surface molds and plaques for BT.
  I. *Intracavitary BT*: radioactive sources and the applicators are placed into an existing body cavity (e.g. vagina, Fig 1.1a).
  II. *Interstitial BT*: radioactive sources and the applicators are placed directly into tissue by needles or wires (e.g. prostate, Fig 1.1b and breast).
  III. *Intralumenal BT*: radioactive sources and the applicators are placed into a lumen (e.g. oesophagus).
  IV. *Intravascular BT*: radioactive sources and the applicators are placed into an artery.
  V. *Surface molds and plaques*: radioactive sources and the applicators are placed onto a surface to enable uniform dose distribution to the engaged surface area (e.g. sinuses, nasal cavity, and orbit).

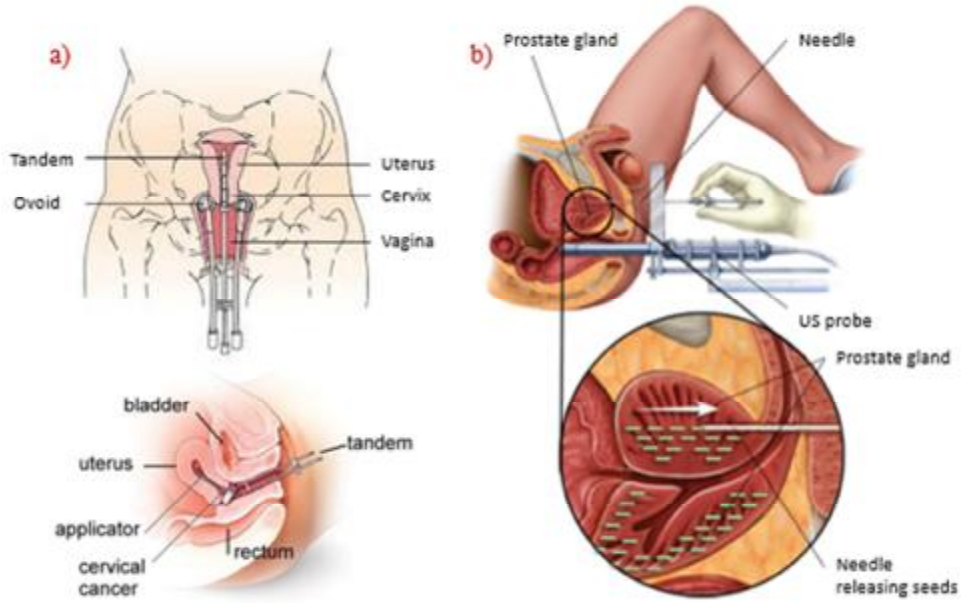

Figure 1.1. a. Intracavitary BT for cervical cancers (web1, 2018), b. Interstitial BT for prostate cancer (web2, 2018)

- According to duration; temporary and permanent BT.
  I. *Permanent*, LDR small radioactive seeds are inserted into the treatment area and left to decay. After a while, they decay to zero by emitting radiation and does not have a permanent effect (e.g. ^{125}I seeds for prostate BT).
  II. *Temporary*, Radioctive source is removed after the treatment taking time generally between several minutes and a day.

- According to dose rate; low, medium, and high dose rates (ICRU38, 1985).
  I. *Low Dose Rate (LDR):* 0.4 – 2 Gy/h
  II. *Medium Dose Rate (MDR):* 2 – 12 Gy/h
  III. *High Dose Rate (HDR):* More than 12 Gy/h

Additionally, pulsed dose rate (PDR) BT is a specific technique in which HDR 'pulses' (mostly the durations of 5-10 minutes) are replicated at short intervals (mostly once per hour).

In radiotherapy, the absorbed dose is used as an elementary quantity to measure the absorbed energy, which is the amount of deposited energy per unit mass of absorbent material (i.e. tissue) by ionizing radiation and defined as Gray (Gy). Thus, dose refers to as absorbed dose in this part. Another term, dose rate, is absorbed dose per time unit.

The selection of treatment or combination of treatments is based on various aspects such as the stage of the cancer, the age and medical/physical condition of the patient, patient predilections and quality of life (Picard et al., 2012; Holm, 2013).

In general, the half-life of the radioactive sources is important the choice of radioisotopes used in LDR or HDR BT. We can shortly summarize most commonly used radioisotopes including their properties below (Yang et al., 2016);

High Energy Sources

^{226}Ra (γ-ray, 1600y half-life, 0.83 MeV average energy, interstitial BT)

^{137}Cs (γ-ray, 30y half-life, 0.662 MeV average energy, intracavitary BT)

^{60}Co (γ-ray, 5.26y half-life, 1.17 MeV average energy, intracavitary BT)

^{192}Ir (γ-ray, 73.8d half-life, 0.38 MeV average energy, interstitial, intraluminal BT)

^{198}Au (γ-ray, 2.7d half-life, 0.412 MeV average energy, interstitial BT)

Low Energy Sources

^{125}I (X-ray, 59.4d half-life, 0.028 MeV average energy, interstitial BT)

^{103}Pd (X-ray, 17d half-life, 0.021 MeV average energy, interstitial, plaque BT)

^{131}Cs (γ-ray, 9.7d half-life, 0.03 MeV average energy, interstitial BT)

^{32}P (β-ray, 14.3d half-life, 0.695 MeV average energy, intravascular, plaque BT)

^{90}Sr (β-ray, 28.9d half-life, 0.196 MeV average energy, plaque BT)

^{90}Y (β-ray, 64.1h half-life, 0.933 MeV average energy, plaque BT)

1.3.2. Imaging in Brachytherapy

During the past several years, imaging has been the most important influence that allows gradual improvement for the developments in BT treatments. Modern 3D imaging techniques have become an integral part of the planning process for various treatment areas, made possible with the increasing availability of high-quality imaging equipment (Lee, 2014). Since MRI, CT, and US techniques are used before and during the treatment, great importance is attached to the development of these techniques in increasing target volume and OAR optimization.

While X-ray imaging, CT, and US have been the preferred imaging modalities for cervix and prostate brachytherapy treatment plans for many years, technological developments in MRI have begun to increase rapidly with the increase in the use of MRI for brachytherapy treatment planning in the last two decades (Tanderup et al., 2014). The superior ability of MRI to visualize soft tissues when compared to CT,

MRI an important part of the imaging process, which is the most remarkable modality in tumour definition.

Furthermore, different imaging modalities provide different information for treatment planning, and the need to incorporate image data sets within the same data plan has led the development of image registration and fusion techniques. These modalities display the same tissues and provide complex tools that help differentiate between tomour and normal tissue (Lee, 2014).

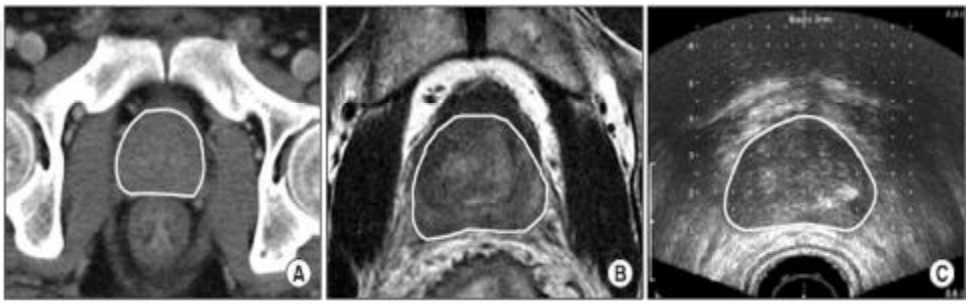

Figure 1.2. Prostate contours based on different modalities a. CT, b. MRI, and c. TRUS (Park et al., 2011)

In order to compare the above imaging techniques, prostate is given as an example (Fig 1.2). Advanced imaging modalities play a critical role, especially in the treatment of prostate patients with BT. For early stage prostate cancer patients, the whole prostate is generally prescribed as the target volume and would be treated to the prescribed dose but often the tumour is only present in one lobe of the prostate. Identifying the location of the tumour within the prostate would allow better targeting of treatment.

In addition to this, literature shows that some methodologies may fail to distinguish cervical tumour from surrounding normal tissues such as small bowel.

1.3.2.1. Computed Tomography

CT imaging includes detection of the X-rays passing through the sample and the projection of X-rays through tissue at various angles. A reconstructed map of x-ray attenuation coefficients in tissue uses the detected X-ray fluence at varying projection angles. CT scans acquired with a fan-beam geometry are important for certain radiotherapy planning techniques by providing accurate electron density information and high spatial resolution required for EBRT dose calculations and treatment planning (Seco and Evans, 2006; Hrinivich, 2017). CT is one of the important techniques used to determine the volume of the treatment area prior to brachytherapy treatment.

Another important role of X-ray CT is providing information on the attenuation of radiation by the tissues in a form of CT numbers, expressed in Hounsfield Units (HU) as in the following equation (Skrzyński et al., 2010):

$$HU_{tissue} = \left[\left(\frac{\mu_{tissue}(E_{CT}) - \mu_{water}(E_{CT})}{\mu_{water}(E_{CT})}\right)\right] x1000 \quad (1.1)$$

where μ is the linear attenuation coefficient of water and of tissue at the effective energy (E_{CT}). HU for a given tissue is related with the quality of the X-ray beam and different values can be obtained by different scanners. In addition, CT numbers for the same tissue are related with the kV setting and on beam filtration for a single scanner as well (Constantinou et al., 1992; Cozzi et al., 1998).

HU values also play a crucial role in determining the physical parameters of the material prepared when phantom studies are performed in multimodal imaging techniques. Conversion factors categorize materials into either having a HU<0 (water–air assumption) or having a HU>0 (water–bone assumption) for example HU value of the air, water, and cortical bones are -1000, 0, >1000, respectively (Brown et al., 2008). HU values of some tissues were given in Fig 1.3.

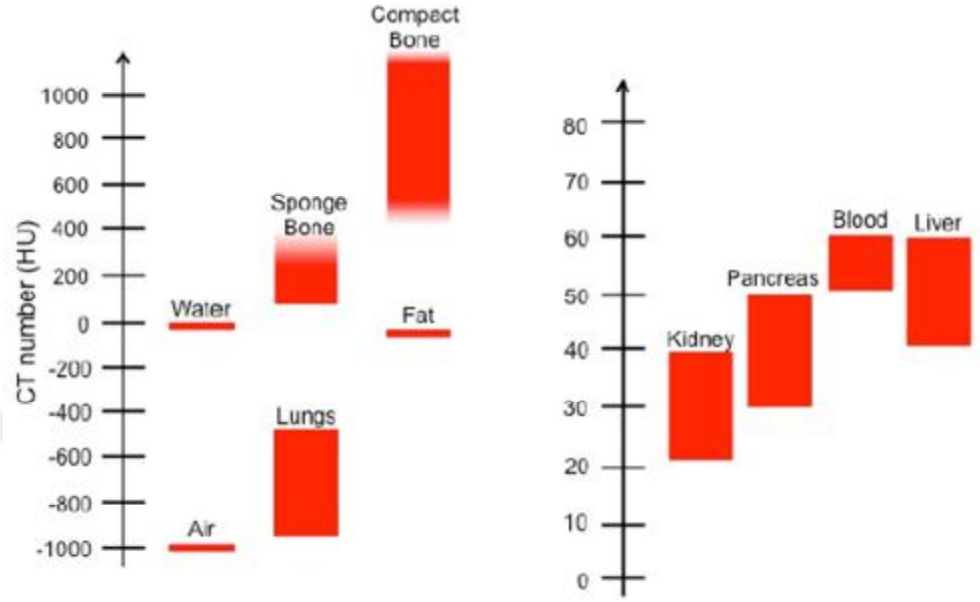

Figure 1.3. HU values of some important organs (In, 2016)

1.3.2.2. Ultrasound

Ultrasonography is simple, portable, and inexpensive image guidance modality in BT allowing precise, conformal, quotable, and adaptive treatments. US is of great importance by assisting four different steps as I) prepatory treatment planning, II) application, III) conclusive treatment planning, IV) quality control. Thus, it has widespread use in prostate BT and increasing role in gynecological and breast BT (Banerjee et al., 2017).

Short pulses of high frequency pressure waves are propagated into tissue by piezoelectric elements acoustically connected to the tissue in diagnostic US imaging. These piezoelectric elements are arranged as an array in a “probe” or “transducer”. Regional spatial discrepancies in tissue acoustic impedance cause partial scattering and pulse energy to be reflected back to the piezoelectric elements, which then converts the mechanical energy taken into an electrical signal. By measuring the time between transmission and reception of echo signals, the distance to the point where each scattering event occurs can be calculated under

the assumption of the speed of sound in the tissue. An amplitude "*A-line*" occurring after each signal is registered is also recorded sequentially along the image plane forming a 2D "Brightness mode (*B-mode*)" image. A grayscale value related with the echo signal amplitude at the point in the scan plane assigns a pixel in the B-mode image. Thus, low amplitude echoes appear darker while high aplitude echoes appear brighter (Garcia, 2011).

As an advantage of US technique, these B-mode images are obtained in "real-time" at a high frame rate, typically 15 Hz or greater at 10-30 frames per second. Higher spatial resolution is provided by higher US frequencies however, it cause greater signal attenuation as well. A specific technique, trans-rectal ultrasound (TRUS) is used for prostate volume measurement in clinical routine (Hrinivich, 2017; Hu et al., 2003). Another technique, trans-abdominal ultrasound (TAUS) allows precise 3D measurement of uterine wall thickness at multiple anatomical levels by an insertion of uterine applicators (Rao and Gohosh, 2015).

1.3.2.2.(1). US/Elastography

Despite first recorded demonstrations almost 25 years ago, US/Elastography is still considered a novel tecknique and not routinely used in clinical imaging. It can provide more detailed information about the area being imaged using the B-mode US image (Gennisson et al., 2013). Colour map information on tissue elasticity in real time on B-mode US image is provided both qualitatively and quantitatively by shear wave elastography (SWE) and only qualitatively by strain elastography. Elastography can be used to demonstrate relative tissue stiffness or displacement (strain) in response to an aplied force as a non-invasive imaging technique. Stiff tissues reveal less strain than soft ones, when the same force is applied (Lerner et al., 1990; Ginat et al., 2009).

From a physics point of view, elastography is a technique measuring tissue stiffness in terms of its Young's modulus (*E*). *E* demonstrates significant variations between different tissues to characterize with a successful contrast (see Fig 1.4).

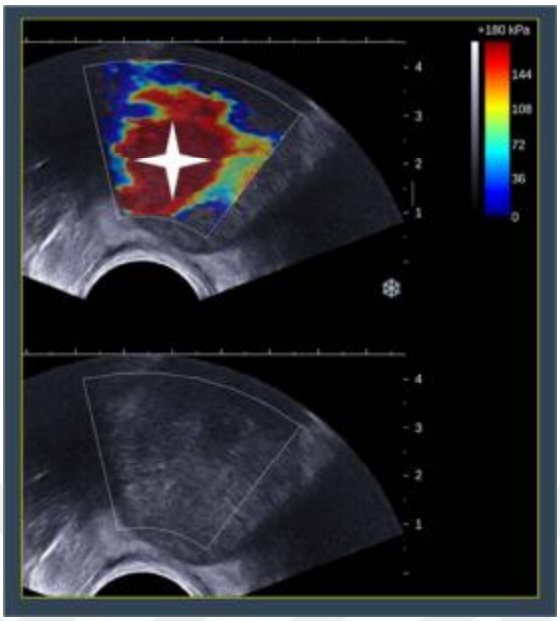

Figure 1.4. Patient with no detected nodule on B-mode imaging (bottom) and SWE image exhibiting stiffness values over 180 kPa and the colour difference within the entire prostate (top) (Correas et al., 2011)

E (Pa) can be calculated with the following equation using Hooke's law;

$$E = \frac{\sigma}{\varepsilon} \qquad \varepsilon = \frac{\Delta L}{L} = \frac{l-L}{L} \tag{1.2}$$

where σ is stress value (Pa) and ε is strain, which is dimensionless. L is the length prior to the applied stress, and l is the length after the applied stress (Garcia, 2011).

The shear wave is the resulting disturbance that affects the surrounding tissue, in a direction parallel to the probe. Propagation and elasticity maps are formed when shear wave propagation speed is parallel to the direction of applied pulses. Maps allow real-time visualization and quantification of shear wave propagation in a user-defined region of interest (ROI). Both dynamic propagation speed and elasticity displays for visual assessment and quantification can be selected during the scan.

1.3.2.3. Magnetic Resonance Imaging

MRI is the most convenient radiological imaging method for soft tissue contrast resolution in which the patient is not exposed to ionizing radiation. If we look briefly at the history of MRI (Ai et al., 2012);

- In 1924, Pauli explained that some atomic nuclei have spin and magnetic moment properties and therefore, they are separated into energy levels when subjected to a magnetic field.
- In 1946, Bloch and Purcell proved that nuclei absorb electromagnetic radiation in a strong magnetic field by being separated into energy levels with the influence of magnetic field.
- In 1965, Stejskal and Tanner suggested a sequence to obtain diffusion sensitization using short-duration gradient pulses that formes the basis for image acquisition strategies used in clinical DW-MRI today.
- In 1966, Ernst and Anderson applied Fourier Transform to NMR.
- At the end of 1960s, Waugh et al. developed NMR imaging technique because of solid-state NMR studies.
- In 1971, Damadian indicated the difference of nuclear magnetic relaxation times of tissues and tumours.
- In 1973, 2D image was created by Lauterbur.
- In 1977, Echo-planar imaging (EPI) as a rapid imaging technique was developed by Mansfield.
- In 1980, Hawkens revealed multiplanar feature of MRI and made the first lesion imaging.
- In 1984, first clinical DW-MRI was used and diffusion coefficients were calculated by Bihan in 1986.
- In 1985 and 1998, MR systems of 1.5 and 3T were introduced.
- In 2005, DKI was suggested by Jensen et al.

MRI devices consist of three main components as magnets (permanent, resistive, and superconductive), coils (shim, gradient, radiofrequency, and patient), and computer. However, one of the most important developments in the history of MRI has been the development and use of superconductors, since the magnetic field used in MRI is generated by superconductors.

MRI images are created by image processing from digitized values such as CT and these digital images can be processed by computer technology to create 3D images. Normally the human body is insensitive to radiofrequency (RF) energy used in MRI devices. First, it is necessary to ensure that protons, which are data sources, are stimulated by RF energy. For this purpose, the patient is placed in a strong magnetic field (e.g., 3T MRI magnets is about 10^5 times stronger than the magnetic field of the earth). Protons are alligned to the magnetic field by the magnetic field and become ready to be excited. RF energy is transmitted to the section to be scanned. Protons absorb this energy and become excited related to the amount of energy. After cutting the energy, protons return to their former positions and emit the received energy in the form of an energy signal. MRI images are composed of these signals (Çelik and Elmaoğlu, 2012; web3, 2018). A k-space (k is the symbol for wave number) is a voxel matrix where the raw imaging data is stored in MRI system (Twieg, 1983). Frequency is mostly represented by the horizontal axis (x-axis) of the matrix and the vertical axis (y-axis) is usually the phase. The raw display data in k-space must be Fourier transformed to get the final image (Bitar et al., 2006). The meaning of the gray tones in images depends on the scanning protocol used. White-light tones signify increased signal areas and dark-black tones signify areas with little or no signal at the final image.

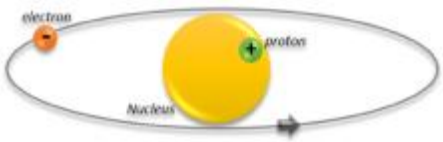

Figure 1.5. Composition of an atom

The basic structures of the atomic nucleus, protons and neutrons, rotate around their axis, which is called "*spin motion*". Due to this motion, protons act like a magnetic rod, and a magnetic field naturally occurs in their surroundings. Hydrogen atoms have a strong magnetic field because its nucleus contains only one proton as seen in Fig 1.5.

Thus, hydrogen is ideal as a signal source and it is abundant in the human body. However, protons are randomly arranged in the tissues such as to remove the effects of each other normally as seen in Fig 1.6a. Therefore, the magnetism of the human body is zero. When the body part to be examined is placed in a strong magnetic field, the protons become parallel or antiparallel (Fig 1.6b).

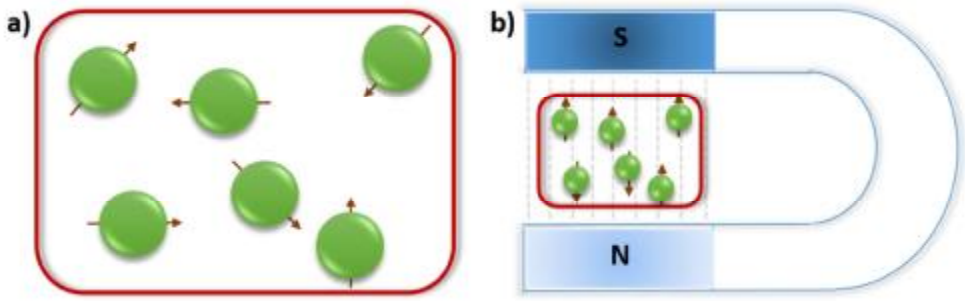

Figure 1.6. a. Oriantations of magnetic vectors of protons when there is no external static field present, b. Parallel or antiparallel oriantations of magnetic vectors of protons to main magnetic field

After protons are positioned, this parallelism is not a stationary posture, but a rotation like a spinning top around the magnetic field, which is called a "*precession motion*" shown in Fig 1.7. Precession is the base of the MR phenomenon because only protons precessing can resonate with a radio wave (with RF) at the precession frequency to be transmitted from the outside. Protons excited by the radio wave deviate from their position parallel to the magnetic field vector and make an angle with the vector.

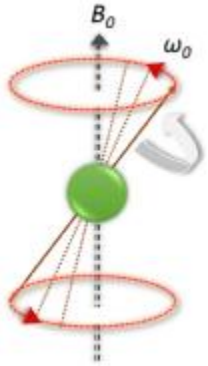

Figure 1.7. Precession motion of spins in applied B_0 magnetic field

When the applied RF is interrupted, protons return to their previous positions. The alternative current produced by this precession motion is the MR signal used in the image.

Main physical terms used and evaluated in this part;

As abovementioned, spin vectors of protons are not exactly parallel or antiparallel and make an angle with magnetic field axis. Components that are parallel to and in the same direction as the magnetic field are "*longitudinal*", perpendicular ones are defined as "*transverse*" components. Spin vectors precess at a characteristic frequency called the "*Larmor frequency"* (ω_0) proportional to the magnetic field B_0 in the nuclei region as summarized in the Eqs below,

$$\omega = \gamma . B_0 \qquad \omega = 2\pi f \qquad f = \frac{\gamma}{2\pi} B_0 \tag{1.3}$$

where γ is gyromagnetic ratio, specific value related to the size of nuclei (for ^{1}H γ=2.677522 x 10^8 1/sT). Thus, f is equal to 42.577 B_0 (MHz/T), which means that spin vectors of protons in a 1T magnetic field rotate at a frequency of 42.577 MHz. Consequently, the transmitted RF has to be commensurate with Larmor frequency of protons.

Under the influence of the RF induced magnetic field vector (B_1), the net magnetic field vector shows two independent motions at the same time (see Fig 1.8a). The net magnetization (M_0) vector rotates both around the magnetic field vector B_1 belonging to RF and the magnetic field B_0.

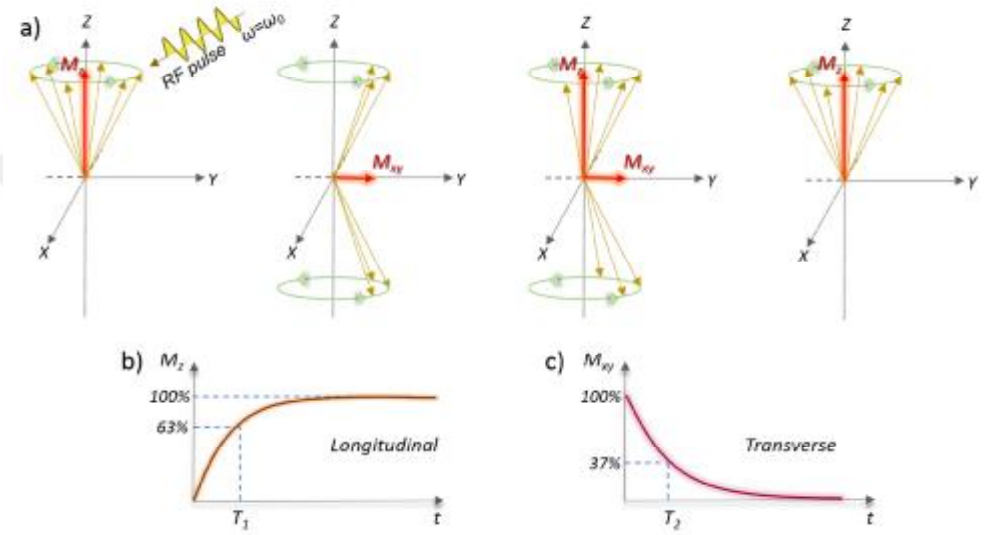

Figure 1.8. a. Position of the net magnetism vector before and after the RF pulse, b. T_1, and c. T_2 times depending on the net magnetism vector

As shown above, when the RF pulse is applied, there will be a deviation towards the transverse surface (x-y plane). This fliping angle (φ) is found as;

$$\varphi = \gamma . B_1 . \Delta t \quad (1.4)$$

where Δt is RF pulse duration. If the RF pulse diverts the magnetism vector to the x-y plane, it is defined as "90°*pulse*". If the magnetic field vector B_1 is doubled, the magnetism vector is formed in the opposite direction to the magnetic field. This RF pulse is called as "180°*pulse*".

After a certain period, the excited spin system returns to its original position and the magnetization vector is again aligned with the direction of the magnetic field. There are two processes involved in the return to equilibrium:

I. Spin – Lattice Relaxation (T_1 time)

$$M_z = M_0(1 - e^{-t/T1}) \tag{1.5}$$

II. Spin – Spin Relaxation (T_2 time)

$$M_{xy} = M_0\, e^{-t/T2} \tag{1.6}$$

T_1 relaxation is the process whereby the net magnetization (M_0) returns to its initial maximum value (M_z) parallel to B_0. It is similar to a charging capacitor, where T_1 is the time required for the magnetization to return to 63% of its equilibrium value (see Fig 1.8b). At least two measurements must be applied to measure T_1 time. Every measurement starts with 180° pulses reversing the measurement magnetism vector. ***T_2 relaxation*** is the process whereby the transverse components of magnetization (M_{xy}) dephase or decay. Protons interact with each other due to their magnetic moments, which is called spin-spin interaction, but as the spin vectors begin to lose phase coherence, the amplitude of the transversal component gradually decreases. T_2 is the time when the signal amplitude decreases to its 37% original value (see Fig 1.8c). In fact, since there is no homogeneous magnetic field, the magnetism vector rotates at different frequencies. The loss of phase coherence of the magnetism vectors also affects the signal amplitude and T_2 time.

Table 1.1 shows some T_1 and T_2 relaxation times of the real tissues obtained by using 1.5 and 3T, respectively.

Table 1.1. Relaxation times of some tissues obtained at 1.5 and 3T (Stanisz et al., 2005; de Bazelaire et al., 2004)

Tissue	T_1 (ms)		T_2 (ms)	
	1.5T	3.0T	1.5T	3.0T
Liver	576 ± 30	812 ± 64	46 ± 6	42 ± 3
Muscle	1008 ± 20	1412 ± 13	44 ± 6	50 ± 4
Heart	1030 ± 34	1471 ± 31	40 ± 6	47 ± 11
Kidney	690 ± 30	1194 ± 27	55 ± 3	56 ± 4
White matter	884 ± 50	1084 ± 45	72 ± 4	69 ± 3
Gray matter	1124 ± 50	1820 ± 114	95 ± 8	99 ± 7
Optic nerve	815 ± 30	1083 ± 39	77 ± 9	78 ± 5
Spinal cord	745 ± 37	993 ± 47	74 ± 6	78 ± 2
Blood	1441 ± 120	1932 ± 85	290 ± 30	275 ± 50
Endometrium	1274 ± 64	1453 ± 123	101 ± 21	59 ± 1
Cervix	1135 ± 154	1616 ± 61	58 ± 20	83 ± 7
Prostate	1317 ± 85	1597 ± 42	88 ± 0	74 ± 9

There are only two fundamental MRI pulse sequences, spin-echo (SE) and gradient-echo (GRE), and other MRI sequences are modifications of them by including divergent parameters (Bitar et al., 2006). By the SE technique, it is possible to achieve phase difference of the magnetism vectors at a certain point of the time (*echo time*, T_E). It is necessary to apply an 180̊ pulse for a certain time ($T_E/2$) after 90̊ pulse. T_E implies the time from the center of the RF pulse to the center of the echo. "*Repetition time*" (T_R), is time length between equivalent sequential points on a repetitious series of pulses and echoes (see Fig 1.9).

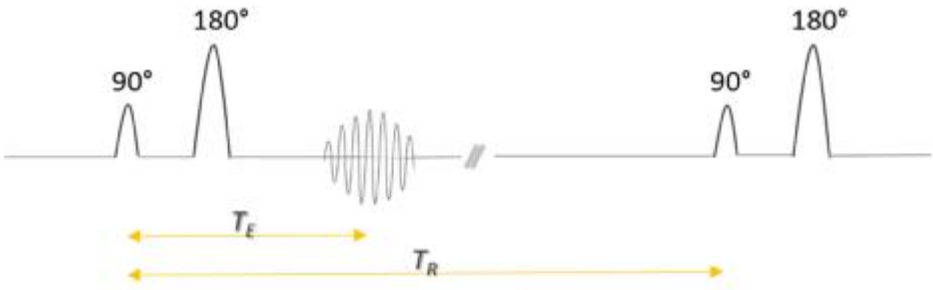

Figure 1.9. SE pulse sequence representing T_E and T_R times

SE is obtained by a pair of RF pulses, while a GRE is obtained by a single RF pulse with a gradient return, which refocuses only spins dephased by action of the gradient itself. Thus, T_E and T_R are generally shorter with GRE sequences than SE ones because the echo can be recorded much faster when only one RF pulse is applied. Multi-echo technique can be used to measure the T_2 time of an object, with a 90° pulse followed by at least two 180° pulses. The maximum amplitudes of the echo signals are related to the signal width in a homogeneous magnetic field. The T_2 time of an object can be determined with the decreasing curves obtained in this manner. However, the time obtained from the fact that the magnetic field is not homogeneousis expressed as T_2*. R_1, R_2, and R_2* relaxation rates are found in proportion to the reversal of T_1, T_2, and T_2* relaxation times, respectively.

After Hahn (1950) discovered the nuclear magnetic resonance spin echoes, Stejskal and Tanner (1965) developed “pulsed gradient spin echo (PGSE)” sequence depending on a pair of dephasing/rephrasing gradient pulses. During the first diffusion gradient, spins of water molecules start to dephase after 90° RF pulse (Andre, 2014) (see Fig 1.10).

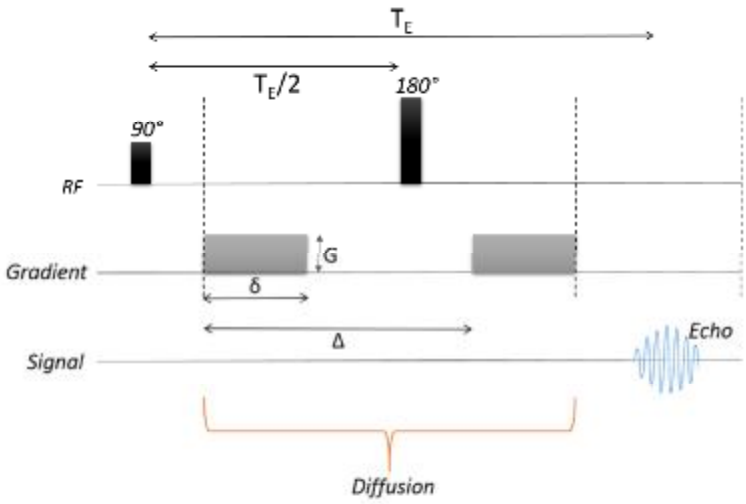

Figure 1.10. PGSE sequence for water diffusion (δ is the gradient duration, Δ the diffusion time, and G the gradient strength)

Echo planar imaging (EPI) sequence, which is the main sequence of DW-MRI, uses rapidly varying gradients to obtain the entirety of the k-space in a spin echo. Multiple GREs are produced in the single SE. Phase encoding steps were obtained using various gradient strengths.

1.3.2.3.(1). Diffusion-Weighted Magnetic Resonance Imaging

DW-MRI is an elemental constituent of the multi parametric MRI examination due to its unique susceptibility to the microscopic structure of the tissue by measuring the apparent diffusion coefficient (ADC) (Panagiotaki et al., 2015). DW-MRI is performed as the tissue is serially imaged while changing the degree of water diffusion sensitization. The images are achieved at different b-values (unit: s/mm^2), the degree of diffusion sensitization, to compute a parametric map (ADC map) allowing quantitative evaluation of the water diffusion behaviour of the tissue. Diffusion is a random process and is termed “reflected Brownian motion” (Grebenkov, 2007; Le Bihan, 2013; Rosenkrantz et al., 2015) (Fig 1.11).

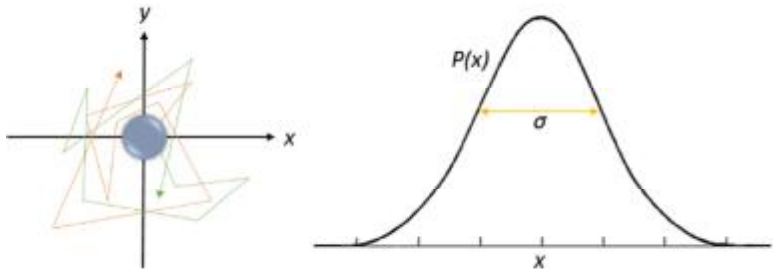

Figure 1.11 Brownian motion of molecules and the probability of the molecule following Gaussian distribution with standard deviation σ

Gaussian distribution is the simplest model to explain water diffusion in the tissue (Stejskal and Tanner, 1965), increasing the degree of diffusion weighting (b-value) results in a linear decay of the natural logarithm of the DW-MRI signal intensity (I). ADC is obtained using standard monoexponential analysis as;

$$\log\left(\frac{I}{I_0}\right) = -(\gamma\delta G)^2.\left(\Delta - \frac{\delta}{3}\right).ADC = -b.ADC \quad (1.7)$$

where I_0 represents the predicted I at a b-value of 0 s/mm^2. As seen above (Fig 1.10), the b-value is dependent on the amplitude of the diffusion gradients (G), the duration of these gradients (δ), and the time between the starting points of the two diffusion gradient pulses (Δ) (Bibic, 2006).

Diffusion gradients, G are not necessarily rectangular but also it is possible to use trapezoidal or half-sinusoidal gradient pulses. The reason for the use of these pulses is the significant deceleration of the entering and trailing edges, small eddy currents close to the conductive materials and significant reduction in the deformations of the magnetic field gradients (Marcon et al., 2011). In conventional pulse sequences, gradient pulses are trapezoidal in shape with a sloping rise, followed by a flat plateau and a sloping fall. For trapezoidal gradient pulses with rise (fall) time t_{rise} (t_{fall}) and flat top time t_{flat}, the duration δ is defined as t_{rise} + t_{flat} instead of the total pulse length t_{rise} + t_{flat} + t_{fall}. Therefore, the gradient moment for a symmetric trapezoidal gradient with t_{fall}= t_{rise} is δ times the gradient amplitude G (McRobbie et al., 2006; Portakal et al., 2018) (Fig 1.12).

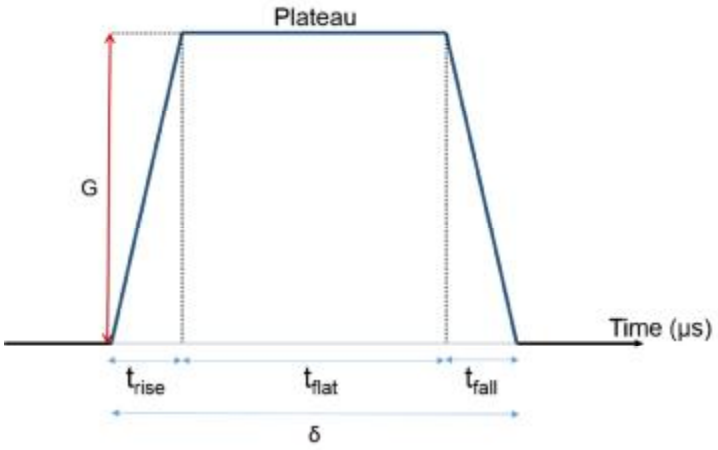

Figure 1.12. Trapezoidal gradient pulse

The ADC must be expressed in tensor form to characterize the directional dependence of diffusion and its vector can be created with the calculation an ADC map for each direction. At least six directions are imperative to fully describe the 3 x 3 diffusion tensor matrix.

$$ADC = M^{-1}\begin{bmatrix} ADC_{110} \\ ADC_{101} \\ ADC_{011} \\ ADC_{-110} \\ ADC_{-101} \\ ADC_{0-11} \end{bmatrix} = \begin{bmatrix} ADC_{xx} & ADC_{xy} & ADC_{xz} \\ ADC_{yx} & ADC_{yy} & ADC_{yz} \\ ADC_{zx} & ADC_{zy} & ADC_{zz} \end{bmatrix} \quad (1.8)$$

where M is a transformation matrix that depends on the applied diffusion directions only. Off-diagonal elements are identical; $ADC_{xy} = ADC_{yx}$, $ADC_{xz} = ADC_{zx}$, $ADC_{yz} = ADC_{zy}$. If the average diffusivity is necessary, it can be expressed as;

$$< ADC > = \frac{ADC_{xx}+ADC_{yy}+ADC_{zz}}{3} \quad (1.9)$$

Note that, only one diffusion direction is used in situations, in which the diffusion process is the identical in all spatial directions, i.e., an isotropic environment (Phillips and Charles-Edwards, 2015).

1.3.2.3.(2). Diffusion Kurtosis Imaging

Biological tissues contain complex microstructures and cellular forms such as membranes and organels and water diffusion intra/inter-cellularly does not conform the displacement probability in Gaussian form (Phillips and Charles-Edwards, 2015). The disrupted diffusion is assigned to non-Gaussian diffusion (Jensen et al., 2005; Jensen and Helpern, 2010).

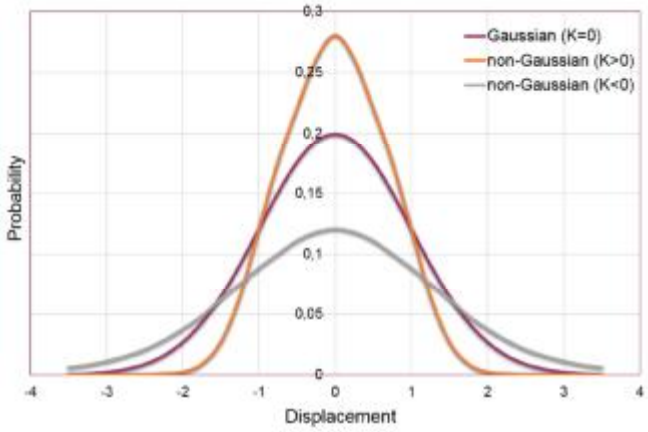

Figure 1.13. Probability density function for Gaussian and non-Gaussian diffusion

- There are several ways to determine whether the data come from a normal distribution. Especially, skewness and kurtosis statistics give us information about the shape of distribution, the data. More clearly, skewness is a measure of symmetry and kurtosis is a measure of the flatness of the distribution (Fig 1.13). Therefore, the absolute value of the kurtosis or kurtosis squared can be used to measure the non-Gaussian distribution (DeCarlo, 1997).

If M_n is the nth moment of a distribution, then K may be defined as;

$$K = \frac{M_4}{M_2^2} - 3 = \frac{\int r^4 P(r) dr}{(\int r^2 P(r) dr)^2} - 3 \qquad (1.10)$$

where P(r) is the probability density function describing displacement r.

For Gaussian distributions, K is 0. K becomes smaller than 0, if a distribution has less weight on its center and tails compared to a Gaussian with the same variance and K becomes greater than 0 if has more weight on its center and tails (Jensen and Helpern, 2010).

DKI is intended to represent the degree of such non-Gaussian diffusion processes by replacing the monoexponential fitting of the signal with a quadratic one. A dimensionless coefficient quantifying the kurtosis, K is included.

$$\log\left(\frac{I}{I_0}\right) = -b.D + \frac{1}{6}b^2D^2K + O(b^3) \quad (1.11)$$

This equation (Eq 1.11) consist of two variables *D* and *K* in comparison with the monoexponential model when *D* is the diffusion coefficient (unit: mm^2/s) and *K* is kurtosis (unitless) which reflects the deviation of tissue diffusivities from Gaussian behavior (Fig 1.14) (Jensen et al., 2005; Rosenkrantz et al., 2015).

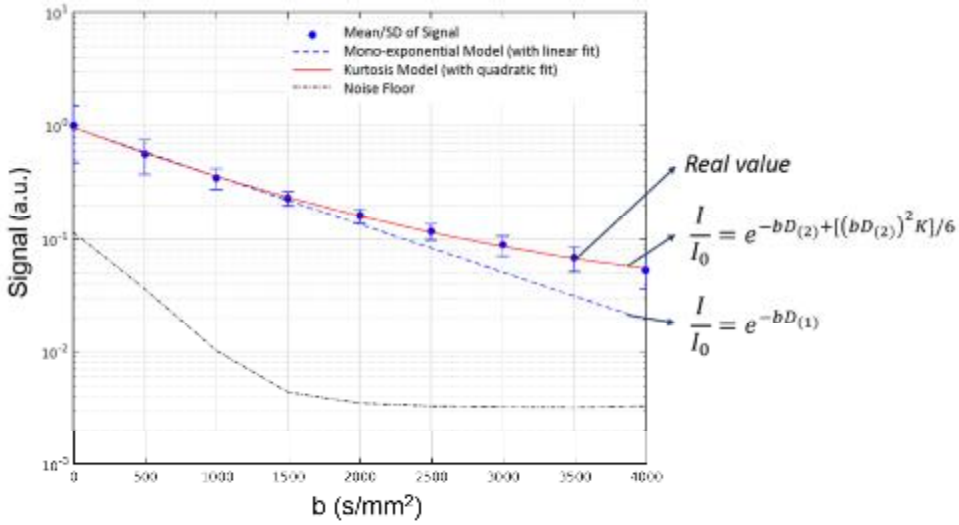

Figure 1.14. Comparison of monoexponential model with kurtosis model

Table 1.2. Reported *in vivo* kurtosis values of some tissues with their SDs

Tissue	Kurtosis	References
Healthy prostate (peripheral zone)	0.57 (0.07)	Rosenkrantz et al., 2012
Diseased prostate	0.96 (0.24)	Rosenkrantz et al., 2012
Healthy lung	0.34 (0.03)	Trampel et al., 2006
Diseased lung	0.22	Trampel et al., 2006
Gray matter (brain)	0.41	Minati and Weglarz, 2007
White matter (brain)	0.70	Minati and Weglarz, 2007
Healthy breast	0.65 (0.11)	Sun et al., 2015
Diseased breast	1.05 (0.22)	Sun et al., 2015
Cervical tumour	0.86 (0.13)	Wang et al., 2018

Typically, the ADC (which we will refer to as $D_{(1)}$) obtained from the monoexponential model deviates from the exact value of the diffusion coefficient (we will define it as $D_{(2)}$) (see Fig 1.14). Non-Gaussian diffusion, quantified by the kurtosis, is acquired at least three b-values mostly using a maximum value of at least about 1500 s/mm^2. Reported *in vivo* kurtosis values are summarized in Table 1.2.

It is crucial to give weight to the noise floor to inhibit artificially exaggerated kurtosis estimates due to pseudo-kurtosis (Portakal et al., 2018). When we look at the Fig 1.14, it is seen that the fits do not hit to the noise floor, which will help us to find the accurate results. The main problem is DW-MRI is a technique sensitive to noise. Thus, the estimated diffusion parameters gradually deviates from the true values when SNR in the images is too low (Scheel et al., 2015).

1.3.3. Imaging Phantoms

The development and confirmation of imaging protocols and sequences used in advanced imaging modalities such as DKI are of great significance. It is necessary to develop experimentally well-characterised tissue-mimicking phantoms that can be used for testing, development, quality assurance (QA), calibration, and understanding the physics governing the imaging observations. Phantoms can be tissue-mimicking in various aspects related to the imaging modality to be used. In general, density, homogeneity and relaxation times similar to those of the tissues being modelled are desirable for MRI phantoms when electron density and efficient atomic number (Z_{eff}) for CT and elasticity for US/Elastography. These phantoms must represent similar properties at RT comparable to those of benign or malignant tissue at body temperature and be stable over time (Portakal et al., 2018).

Aqueous solutions and gels are the main phantoms types generally used in MRI studies. Although it is quite easy to prepare aqueous solutions, they are not tissue-mimicking in many aspects. Unlike human tissue, their T_1 and T_2 relaxation times are nearly identical, for which the T_1 values are typically much longer than

T_2. On the other hand, gel phantoms can be created to mimic the T_1 and T_2 values of human tissues (Hattori et al., 2013). They are substantially easy to prepare and use, cost-effective, reusable, less prone to leakage, durable, and have a long lifetime when a preservative material is added to prevent bacterial growth. Additionally aqueous solutions are not useful for ultrasonic measurements although they can be used in CT. Another advantage is gel phantoms can model shape of organs.

Agar, agarose and carrageenan as the most common source of biological gelling agents are obtained from algae while there are also synthetic gelling agents used in various imaging purposes such as polyvinyl alcohol (PVA). Other preferred biological gelling agent is gelatin but it is not used in this study.

1.4. Thesis Statement

This thesis is organized as follows;

In this Chapter, the theoretical background on BT, CT, US/elastography and MRI modalities are summarized with the importance of creating phantoms, especially gel phantoms, to develop new sequences and protocols for multimodal imaging purposes.

Chapter 2 provides literature summary on multimodal phantoms and phantoms for quantification of kurtosis in particular. Additionally, characteristic properties of certain phantom and patient data using advanced imaging modalities are stated.

In Chapter 3, materials and methods on how the phantoms were created, characterized and used in multimodal imaging modalities are presented. Computational details of the development and implementations are described.

Chapter 4 gives the results and examinations of the successes of the gel phantoms created with the obtained characteristics in their use in advanced imaging techniques.

Conclusions and planned future studies are drawn in Chapter 5.

2. LITERATURE REVIEW

2.1. Imaging Gel Phantom Studies

There are many commercial gel phantoms used in clinics for multimodal imaging modalities. However, they are quite expensive and mostly special purpose with limited applications. Thus, it is more practical to prepare proper gel phantoms suitable for sequence and protocol development studies. Prior to the start of the phantom study, the most preferred materials for various imaging methods used were selected based on areview of the existing literature.

Huber et al. (2010) manufactured a tissue-mimicking MRI-PET-CT-TRUS phantom including two-regions (cylinderical "prostate" part within a "pelvis" rectangular cuboid) with mixtures of gelatin, agar, $BaSO_4$, EDTA-tetra Na Hydrate, NaCl, formalin, $CuCl_2$-$2H_2O$, Germall-Plus^{TM} (preservative), glass beads, and deionized water (see Fig 2.1). They stated that the phantom could be used qualitatively to approve interventional procedures such a brachytherapy. They stated that the phantom was quite useful for US-MRI-CT modalities as shown below.

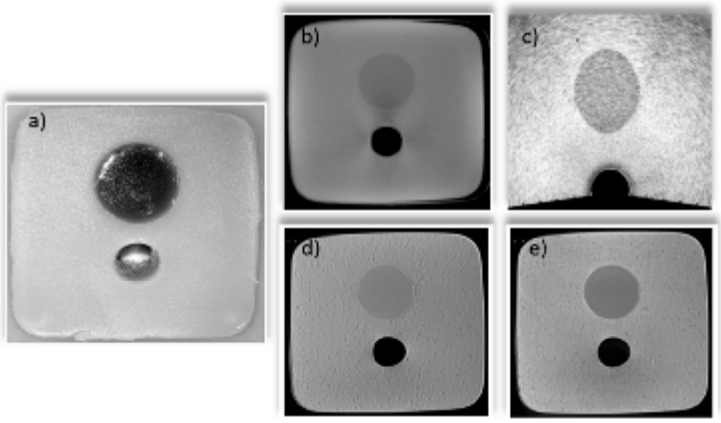

Figure 2.1. a. Photograph of a custom phantom, b. Coronal CT image, c. US image using TRUS probe, d. coronal MRI T_1–weighted image, and e. coronal MRI T_2–weighted image of the phantom (Huber et al., 2010)

Similarly, D'Souza et al. (2001) prepared a multi-imaging modality prostate phantom compatible with MRI, US, and CT using the materials of water, agarose, lipid particles, protein, Cu^{2+}, ethylenediaminetetraacetic acid (EDTA), glass beads, and thimerosal (preservative). They represented quantitative results of the modalities used. The primary features of the attention were given to T_1 and T_2 relaxation times for MRI, propagation speed and attenuation coefficient for US, and X-ray attenuation for CT. T_2 Relaxation times were obtained by 1.5T GE Signa MRI scanner using Carr–Purcell–Meiboom–Gill (CPMG) SE puls sequence with T_R=2000ms and TE=20, 40, 60, and 80ms. Six T_1-weighted images were acquired to get T_1 relaxation times with T_E=15ms and T_R=116, 250, 500, 1000, 2000, and 4000ms. They stated that the HU of *in vivo* prostate is estimated as 45±17 and they found the HU of the phantom as 43±12. Additionally, they represented the similar results of the phantom as the prostate tissue for MRI relaxation times and US characteristics as well.

Cannon et al. (2011) created tissue-mimicking agar based anthropomorphic breast phantoms that were clinically relevant and could be used for QA. The goal of their study was to mimic the properties of the breast tissue parts, malign and benign lesions, pectoral muscle, primarily glandular tissue, subcutaneous fat, and areola. They obtained the acoustic characteristics of the phantoms fabricated with a mixture of silicon carbide, agar, and aluminum oxide in deionized water. They stated that agar was the material of choice as it is easy to manipulate and elastic properties smilar to those of tissue.

Laubach et al. (1998) developed a phantom for DW-MRI purposes to mimic tissue parameters of normal gray matter (GM) and acute stroke using agar gels. As the main idea of the study, they emphasized the importance of phantom studies for the early detection of ischemic injury since an ADC reduced immediately after initiation in acute stroke ares could be found. They have created agar gels with various concentrations of 0.25 to 5% (w/v) and determined T_1, T_2, and ADC values using EPI sequence. An increase in agar concentration decreased

T_2 values from 238 ± 4.3 to 37 ± 2.7 ms. ADC has remained almost constant in the range of 0.25 to 2% as 2.153×10^{-3} mm^2/s but the ADC decreased to around 1.750×10^{-3} mm^2/s for concentrations greater than 2% (see Fig 2.2). Similarly, T_1 values decreased from 1,980.2 ± 58.2 to 1,612.9 ± 71.9 ms with increasing agar concentration. According to their findings, they claimed that 1.5% (w,v) agar gel mimics normal GM. The final phantom including 1.5% agar gel and sucrose solution mimics ADC, proton density (PD), and T_2 variations observed in acute stroke.

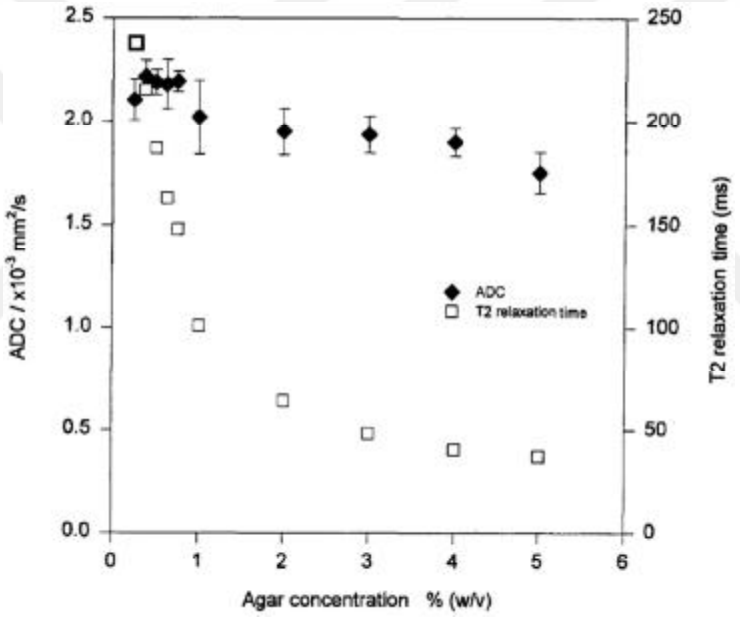

Figure 2.2. ADC and T_2 relaxation time versus the concentration of agar

Lavdas et al. (2013) built a spherical diffusion phantom with nickel-doped agarose/sucrose gels. Phantom includes different compartments to represent healthy, malignant tissues, air, and fat. Thus, different concentrations of agarose gels as well as other materials were prepared. DW-MRI images were obtained using a SS-EPI sequence using five b-values of 0, 150, 400, 750, and 1000 s/mm^2. They analyzed the results as both qualitatively and quantitatively. They have

calculated T_1, T_2, and ADC values as well as their coefficient of variation (CV) values for each compartment. Results showed good repeatability of ADC measurements obtained by the protocol used. They emphesized that the gels were made of easily available, inexpensive, and nontoxic materials. They have also shown that the gels having relaxation and diffusion properties very close to the healthy and diseased tissues could be created. Furthermore, the short-term temporal stability of the gels relating to diffusion properties were found to be excellent.

Sack et al. (2004) manufactured an agarose (1.5 wt%) sol-gel phantom to explore phase transitions using the imaging modalities of DW-MRI and magnetic resonance elastography (MRE). This study is interesting because it enables to build a model based on the underlying physical principles rather than the assumptions about the dynamics of elasticity and diffusion. DW-MRI images were obtained using five b-values of 0, 232, 511, 736, and 1001 s/mm^2 using EPI acquisition. They have found that the calculated images showed good agreement with the experimentally observed MRE wave patterns. ADCs for each pixel were calculated by fitting the logarithm of the signal intensity using a straight function.

In prostate BT, postimplant dosimetry is mostly performed by CT or MR images. De Brabandere et al. (2006) evaluated the reconstruction of the seeds accurately by creating a CT and MRI compatible phantom using agarose gel (4 wt%) in a PMMA [Poly(methyl methacrylate)] container shown in Fig 2.3. The phantom was used for quality control (QC) measurements to visualize seed positions after the implantation. They checked the density of the phantom and stated 1.032 ± 0.011 for agarose versus 1.036 ± 0.022 for prostate. They also claimed that agarose has similar imaging properties as prostate tissue on MRI. T_1=1207±168 ms and T_2=66±9 ms were measured for the agarose gel and T_1=1074±117 and T_2=104±14.6 were measured for a human prostate using the same technique. They have stated that the values they found were very close to the ones reported in literature for prostate tissue as T_1=1317±85 ms and T_2=88±0 ms at 1.5T.

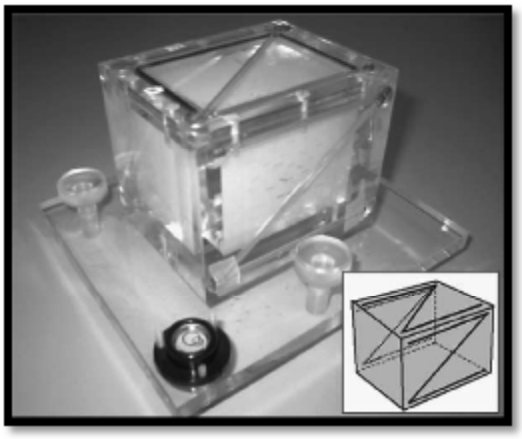

Figure 2.3. PMMA container filled with agarose gel as a prostate phantom (De Brabandere et al., 2006)

Earle et al. (2016) found that agar gel phantoms were the most appropriate option especially for US studies in their evaluation for the most economical, practical and useful gel phantom. They have prepared agar gels with different concentrations as 2.5%, 5.0%, 7.5%, and 10.0%. They compared the physical properties of the gels with gelatin and ideal tissue. They defined these physical properties as density, opacity, echogenicity, reverberation, artefacts, compressibility, and durability (Table 2.1). As a result, they stated that agar gels were durable, cost-effective, not requiring refrigeration, forming gel structure very fast, having a long lifetime, and showing similar acoustic results as the tissue.

Table 2.1. Physical properties of different agar gels compared to gelatin and tissue (Earle et al., 2016)

Model	*10.0% Agar*	*7.5% Agar*	*5.0% Agar*	*2.5% Agar*	*5.0% Gelatine*	*10.0% Gelatine*	*Tissue*
Density	++++	+++	+++	+	+	++	++
Opacity	+++	+++	++	+	+	+	++++
Echogenicity	++	++	++	+	+	+	+++
Reverberation	++	++	+	+	+	+	-
Artefacts	Base/cap layer	Base/ cap layer	Base/ cap layer	Bubbles base/cap layer	Base/cap layer	Base/cap layer	-
Compressibility	++	++	+++	++++	+++++	+++++	++++
Durability	++++	++++	+++	++	+	++	++++

Surry et al. (2004) designed PVA-C phantoms with the concentration of 10% to use in MRI and US. As they have also mentined, the physical properties of the PVA-C phantoms were directly related with the number of “freze-thaw (ft)” cycles applied. US parameters (velocity of sound, attenuation coefficient, etc) were found similar in the range of human tissue. As shown in Fig 2.4, measured T_1 and T_2 times were found in the range of 718–1034ms and 108–175ms, respectively. They also presented additional applications of PVA-C used in breast biopsy phantoms, anthropomorphic brain phantom, and vessel phantom.

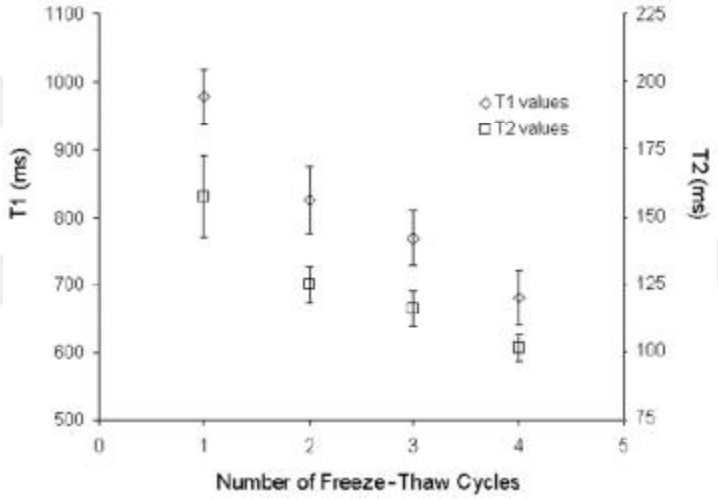

Figure 2.4. T_1 and T_2 relaxation time dependence on “ft” cycle of 10% PVA-C

Dwihapsari et al. (2012) manufactured 10, 12.5, and 15 wt% PVA hydrogels and obtained cryogel forms after applying two to four “ft”. They scanned the phantoms using EPI sequence with a 1.5T GE Signa MRI scanner. Both the concentration and “ft” effects on ADC were evaluated in detail (see Fig 2.5).

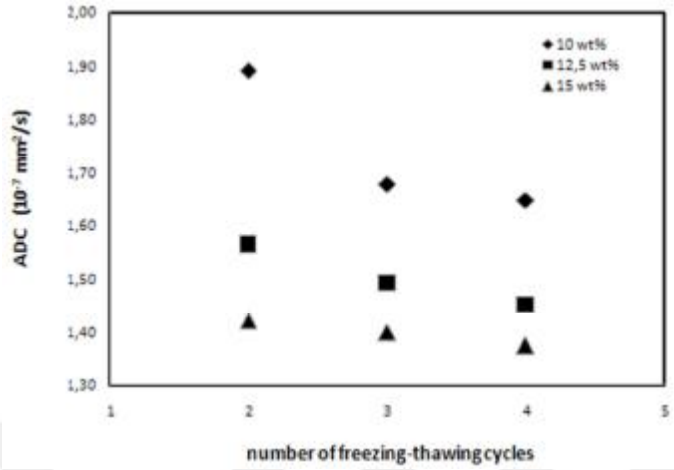

Figure 2.5. ADC values of PVA-C phantoms as a function of "ft" cycle

In (2016) manufactured several polymer-based phantoms including lesion particles mimicking human liver tissue in her PhD thesis study for multimodal imaging. Mixture of carregenan and agar gave smilar HU values as the liver. However, T_1 and T_2 times were obtained lower than the value stated for the liver.

Cao et al. (2013) prepared a tissue-mimicking prostate gel phantom including agar, polyacrylamide, and silicone to check its mechanical properties by using SWE. They stated that Young's Modulus results showed an increase in stiffness with agar concentration. They found the Young's Modulus values of 86.2 ± 4.5 kPa for the phantom compared to it is 90.5 ± 4.5 for the cancerous tissue in the prostate. Barr et al. (2012) reported the value as 58.0 ± 20.7 kPa for prostate cancer while Zhai et al. (2010) measured as 8.0 kPa. Zhang et al. (2008) found as 15.9 ± 5.9 kPa and 40.4 ± 15.7 kPa for normal and cancerous prostate.

Duboeuf et al. (2009) tested and validated the Young's Moduli of four samples of PVA cryogels having different elasticity values to represent those of stiffer soft biological tissues. They stated that measured Young's moduli varied from 70 to 180 kPa depending on the number of "ft" cycles.

2.2. DKI Phantom Studies

Jansen et al. (2010) prepared phantoms containing either Gd-DTPA-doped water or homogenized asparagus to invastigate the use of DKI for head & neck squamous cell carcinoma. They used 4- and 8-channel neurovascular array coils on a 1.5T GE scanner. Seven b-values of 0, 50, 100, 500, 750, 1000, and 1500 s/mm^2 were arranged with the choice of three diffusion sensitization directions using SS SE EPI. A phantom containing Gd-DTPA-doped water demonstrated an excellent Gaussian behaviour with the vaues of $D_{(1)}$= 2.29±0.01 10^{-3} mm^2/s, $D_{(2)}$=2.31±0.02 10^{-3} mm^2/s, and K=0.02±0.02. However, a phantom containing homogeneous asparagus exhibited non-Gaussian behaviour with the values of $D_{(1)}$=1.55±0.07 10^{-3} mm^2/s, $D_{(2)}$=1.75±0.08 10^{-3} mm^2/s, and K= 0.28±0.05. Longterm use and the applications were limited with these phantoms.

Fieremans et al. (2012) used a simple, isotropic and cheap test phantom suitable for DKI data acquisition and postprocessing. Heavy cream (~36% w/w fat) as a phantom material (Fig 2.6) was obtained from a local market and prepared for the scans on a 3T Siemens Verio system with body and 12-chanel head coil. A twice-refocused SE EPI was applied with 3 b-values of 0, 1000 and 2000 s/mm^2.

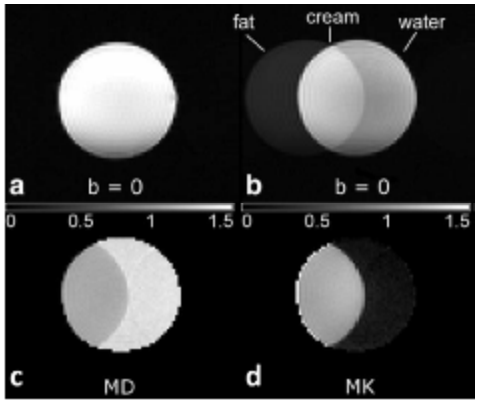

Figure 2.6. b=0 image of the cream phantom a. before and b. after heating for T_E=105 ms, c. parametric maps of mean diffusivity (MD) coefficient, and d. mean kurtosis (MK)

As seen in Fig 2.6, there is a visible separation of the water and fat component due to the difference in resonance frequency between fat and water. Fig 2.7 shows the DKI fits, both the water and fat signal decay non-Gaussian while fat is constant for increasing b-value. K_{cream} is calculated as 1.18±0.04 and reported useful for the DKI purposes while K_{water} is 0.15±0.07 (K_{fat} is zero as expected). However, cream materials are not suitable for longterm use and multimodal imaging modalities and K_{water} should be 0, so a value of 0.15 suggest significant pseudo-kurtosis in their measurement.

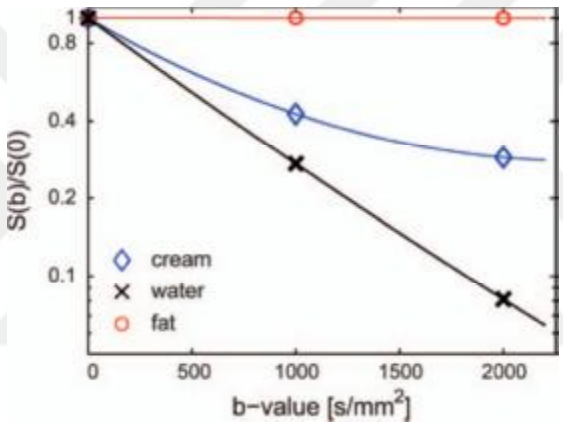

Figure 2.7. Signal decay curves versus b-value within the chosen ROIs including fat only, water only, and cream voxels

Another test object for DKI is colloidal dispersions of colloidal polyethelene particles with a nonionic surfactant and emulsifier (see Fig 2.8) reported by Phillips and Charles-Edwards (2015). A 3T Phillips scanner was used with a loop coil using SS EPI. b-values between $0 \leq b \leq 4500$ s/mm^2 by 500 s/mm^2 intervals were applied. Colloidal phantoms displayed kurtosis values in the range of $0 \leq K \leq 0.62$ including a large range of healthy and pathological tissues. This work is important for the relationship between barrier concentration and kurtosis. Thus, a reliable and robust test object for the assessment of isotropic diffusion kurtosis of those found in vivo was demonstrated by using colloidal dispersions.

While these colloids with a range of concentrations were suitable for long-term use, they did not have the similar relaxation rates as tissue.

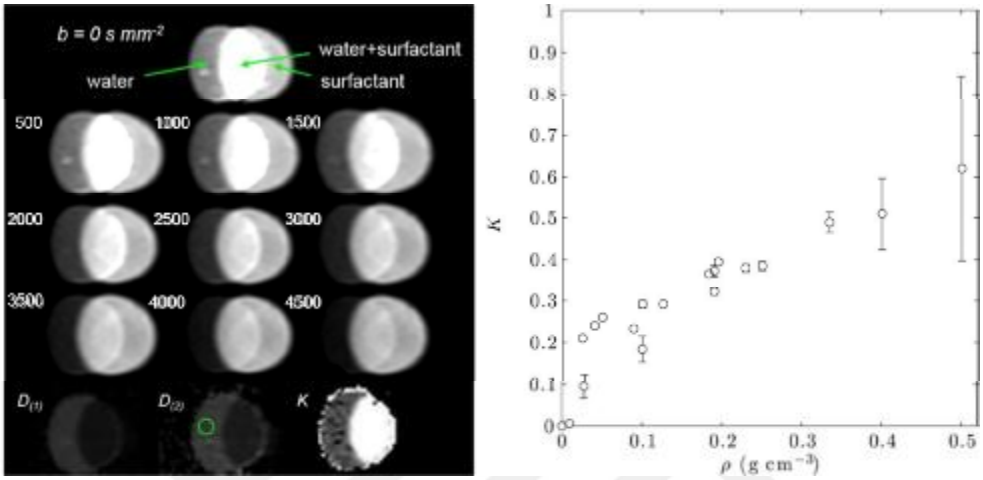

Figure 2.8. DW-MRI images of one sample including $D_{(1)}$, $D_{(2)}$, and *K* maps (right) and *K* values as a function of concentration (right)

Orsingher et al. (2016) obtained the DKI parameters of isotropic aqueous-test solutions using ordinary least squares (OLS), weighted linear least squares (WLLS), and nonlinear least squares (NLS) algorithms with a twice-refocused spin-echo (TRSE) diffusion sequence. They also used asparagus stems as biological anisotropic phantom with different b-values from 800 to 3000 s/mm^2 using a 3T MR system. They demonstrated that pseudo-kurtosis effect could be observed even in free water. Thus, they suggested using of homemade simple phantoms for quality control, sequence optimization and fitting methods comparison. WLLS was given the best results to obtain correct DKI parameters.

Glenn et al. (2015) also reduced noise bias in DKI data with WLLS fitting together with a voxel-wise, subtraction-based noise correction from multiple, independent acquisitions in a dairy cream phantom and human brain using a SS-SE-EPI sequence in 3T device. The method included computational simplicity and convenience of integration into standard WLLS DKI post-processing algorithms.

3. MATERIAL AND METHOD

This study mainly consists of three parts in terms of the methodologies.

First, ideal gel phantoms suitable for various imaging methods were designed and manufactured. Material flow and the methodology of this part are summarized in Section 3.1.

Second, their sufficiency and basic physical parameters as well as quality of the images were determined by using CT, US/Elastography and MRI expressed in Section 3.2, 3.3, 3.4.1., and particially 3.4.2.

Last, the possibility to use of these phantoms for DKI for quality assurance, protocol optimization, and sequence development was invastigated using various protocols. Section 3.4.3 represents the properties of selected and written sequences, features of the MRI devices and the analysis techniques used.

3.1. Phantom Preparation

First, multiple plain and homogeneous gel phantoms with different concentrations and properties were manufactured using different gelling agents, two natural (agar and agarose) and one synthetic (PVA), at Cancer Research Wales Laboratories in Velindre Cancer Centre. Table 3.1 summarizes the preparation method for agar, agarose, and PVA-C phantoms.

While it was quite easy and fast to produce plain agar and agarose gel phantoms, manufacturing PVA-C was a time-consuming process involving two to five “ft” cycles for gelation. After preparing the required PVA mixtures, they were placed in a freezer at -20°C for 10 h and then left at RT for 14 h. This was called as a “freeze-thaw cycle” and repeated at least two times to obtain a proper cryogel. The importance of the number of cycles applied and their effect on on imaging properties were discussed in the literature (Surry et al., 2004; Dwihapsari et al., 2012). The most recommended concentration 10% weight by volume (w,v) was prepared four times and all suggested “ft” cycles were evaluated.

Table 3.1. Preparation method of the desired gel phantoms

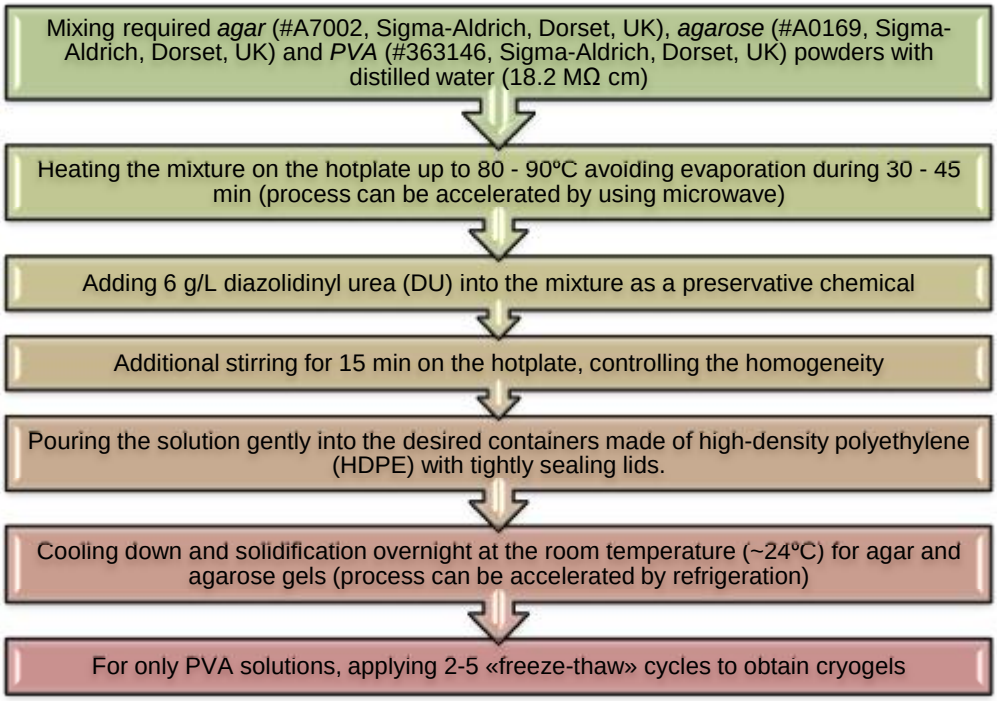

As mentioned above, we initially characterized (obtaining relaxation, diffusion, elasticity, and HU parameters of the phantoms) plain gel phantoms with the concentrations shown in Table 3.2.

Table 3.2. Concentrations of prepared plain gel phantoms

Phantom	**Concentration**					
Agar	1.0% w,v	1.5% w,v	2.0% w,v	2.5% w,v	3.0% w,v	3.5% w,v
Agarose	0.5% w,v	1.0% w,v	1.5% w,v	2.0% w,v	2.5% w,v	3.0% w,v
PVA-C	10% w,v (2ft)	10% w,v (3ft)	10% w,v (4ft)	10% w,v (5ft)	15% w,v (4ft)	20% w,v (4ft)

In the following chapter, the results will show that 4 “ft” cycle was most appropriate for the purpose and further concentrations were prepared with 4 “ft”.

In this thesis, the most suitable concentrations were evaluated for the gelation of small (100 ml) and large (1000 ml) volumes. The gelation process was difficult when the concentration was too low and high. Air bubbles, which must be prevented for the imaging, become a problem with high concentrations during the pouring part. Consequently, eighteen homogeneous and plain phantoms were prepared as 100 and 1000 ml (see Fig 3.1). Additionally the effect of the preservative chemical was investigated.

In the second phase, glass microspheres (gm) (#K20, 3M microspheres, Easy Composites Ltd., Staffordshire, UK) within the size range of 30 μm ≤ 2R ≤ 90 μm were also added into some gel solutions by changing the gm weight per sample (Fig 3.1). New phantoms were created with various additions of gm.

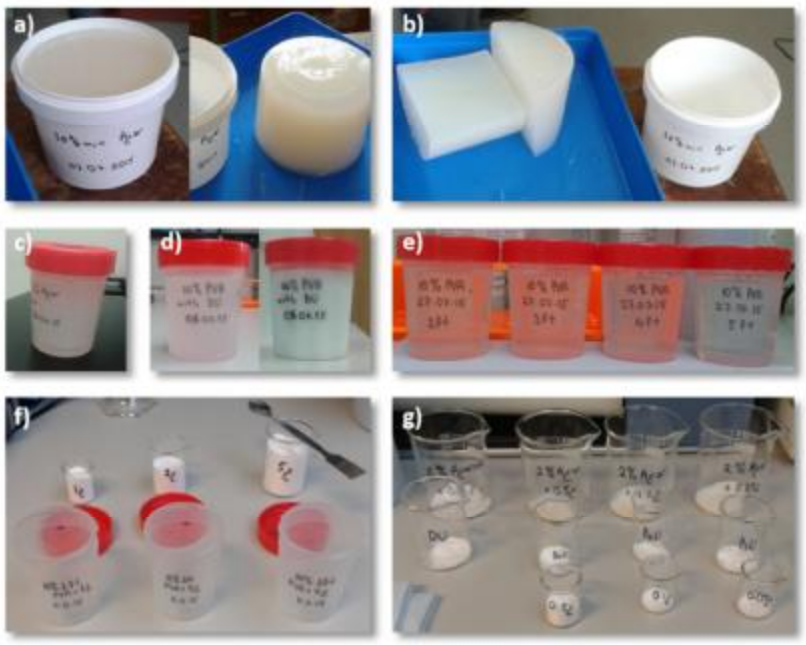

Figure 3.1. a. 1000 ml agar gel sample, b. an example for the durability of the gels, c. 100 ml agar gel sample, d. 100 ml PVA phantom before and after “ft” cycles, e. 100 ml PVA solutions before “ft” cycles, f-g. “gm” addition into the homogeneous gel solutions with different concentrations

Since the densitiy of the added gm (0.2 g/cc) was less than that of the gel solutions, gm is inclined to accumulate at the top. Great importance was given to the homogeneity during the gelification process; it should occur fast enough to avoid the separation of gm. Finally, the imperfections were separated and not used for the further investigations (Fig 3.2).

Figure 3.2. Left: uniform, Right: failed gel phantoms including gm

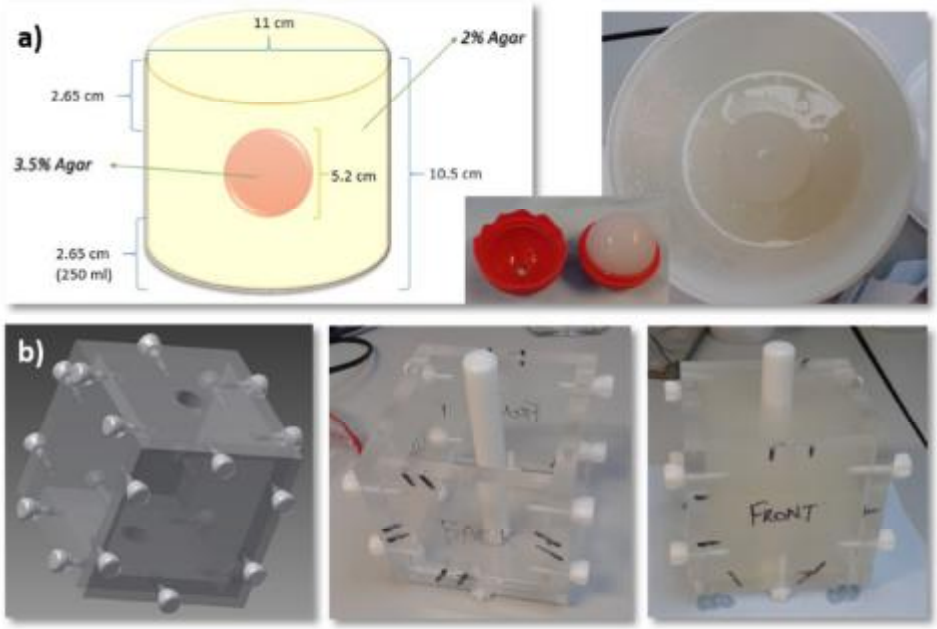

Figure 3.3. Inhomogeneous agar gel phantom with 2.0% background and 3.5% inclusion as a. cylindrical and b. cubical

Efforts to create PVA-C phantoms with the desired microsphere material were abandoned because they resulted in a newly formed viscous material since the gm reacted with the PVA solution. Thus, further investigations were carried out using agar and agarose gels by including gm in various concentrations.

Eighteen 100 ml plain gels and twenty-two gels with gm of dimensions R = 5 cm, h = 5 cm were prepared and scanned by MR and CT. The proper 1000 ml ones were characterized using US/Elastography to check gelling agents qualitatively and quantitatively (the surface of the 100 ml phantoms were too small for the scanning probe). It should be noted that both 100 and 1000 ml samples were prepared with the same properties in the same conditions. Additionally, two different inhomogeneous agar test phantoms were prepared as seen in Fig 3.3 to check qualitatively using multimodal methods.

3.2. CT Measurements

Two CT scanners (Siemens SOMATOM Sensation 64, Fig 3.4a) in Velindre Cancer Centre and (Siemens SOMATOM Definition AS, Fig 3.4b) in Institute of Life Science, Swansea University were used at 120 kVp and 250 mA with 5 mm slice thickness to measure HU values of gel phantoms.

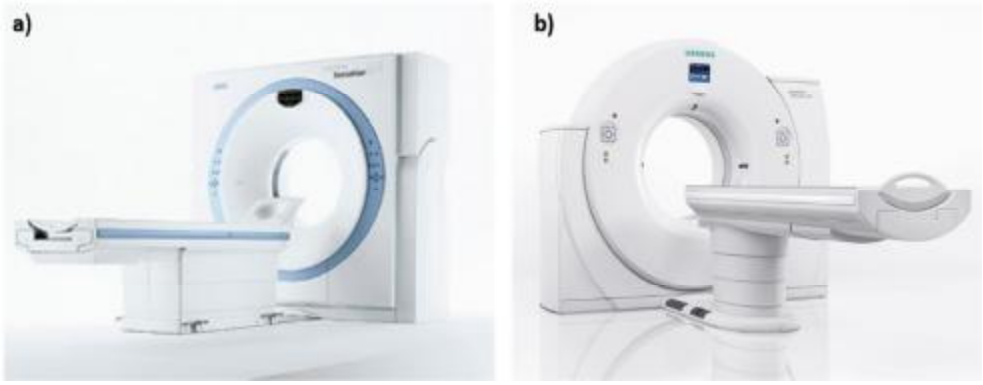

Figure 3.4. a. Siemens Somatom Sensetion 64, b. Siemens Somatom Definition AS CT scanners (web4, 2018)

Clinically, the CT number of a tissue-mimicking material may be of more relevance than the effective X-ray linear attenuation coefficient, μ_{eff}, for characterizing the phantoms (D'Souza et al., 2001).

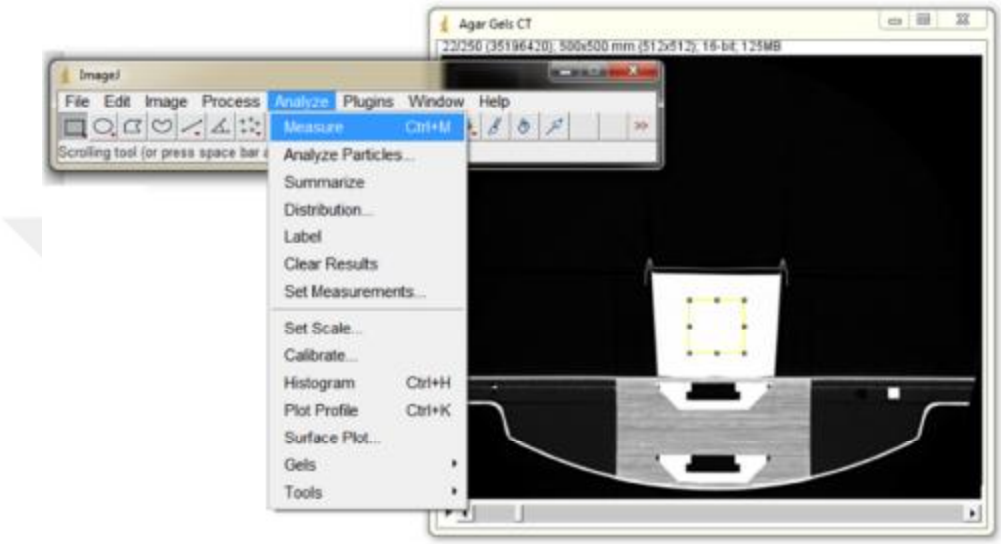

Figure 3.5. ImageJ software to analyze HU values of each gel phantom

To characterize the attenuation properties of gels prepared by using different gelation materials and additives, and to assess the consistency and stability of the compounds over time, CT scans were performed and repeated four times over the period of the study. Mean HU determined over an area of approximately 5 cm^2. ImageJ software was used to analyse HUs on each CT image (see Fig 3.5).

3.3. US/Elastography Measurements

US scanner (Aplio 500, Toshiba, Tokyo, Japan) was used to obtain "strain" and "shear wave" elastography images of the gel phantoms at the Royal National Hospital for Rheumatic Diseases in Bath, UK.

Figure 3.6. US/Elastography device with a linear transducer

The data were acquired with a linear transducer (14L5) having a frequency range between 5 and 14 MHz with a 5cm wide footprint providing a wide range of depth and coverage (see Fig 3.6).

Propagation speed and elasticity maps were obtained for each gel phantom with associated “shear wave speed (m/s)” and “Young’s Modulus (kPa)” information. Propagation maps allow visualization and quantification of shear wave propagation in a user-defined ROI in real-time. The user can select both dynamic propagation speed and elasticity displays for visual assessment and quantification during the scanning (Fig 3.7).

There are two modes of SWE, “continuous” and “one shot”. With continuous mode, we can optimize our skin window and transducer position using the live update in colour maps. Once the optimal window is found, it is suggested to choose one shot mode for best image quality and most accurate shear wave quantification. Thus, images were obtained using one shot mode for each phantom.

All measurements were repeated. Inhomogeneous agar gel phantoms were also scanned using both elastography techniques to check the quality of the images.

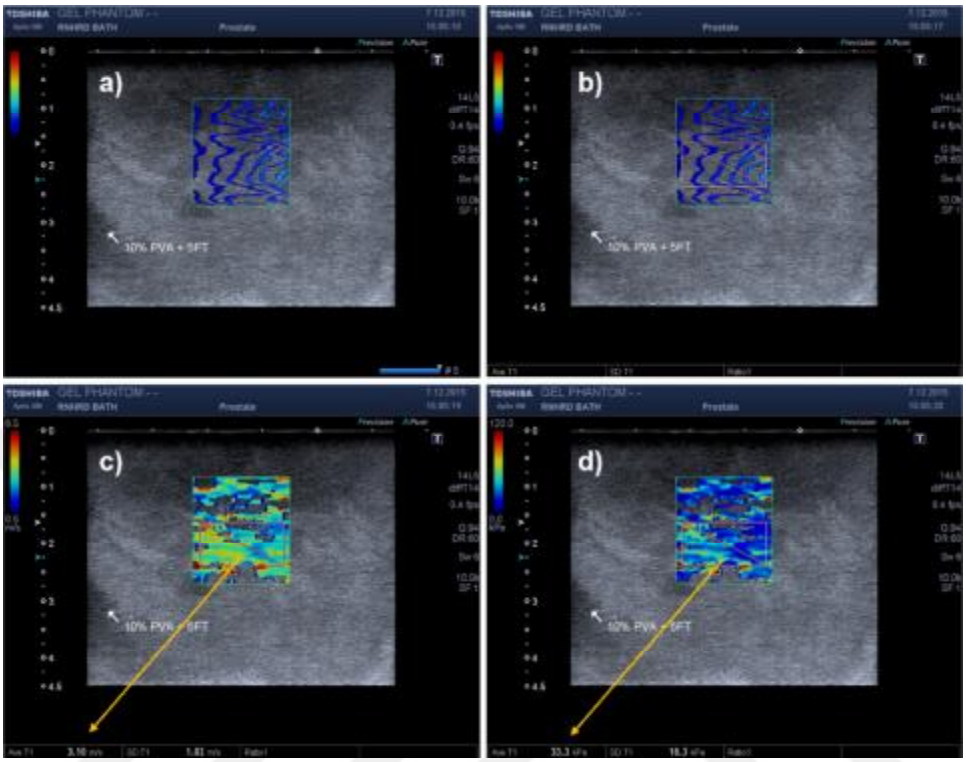

Figure 3.7. a. Propagation distribution, b. ROI selection on the propagation distribution, c. Propagation map, and d. Elasticity map allowing both qualitative and quantitative evaluation

3.4. MRI Measurements

All the gel phantom images were analyzed on a pixel-by-pixel basis using in-house software written by Dr. Shermer in MATLAB (Mathworks, Inc.) including automatic ROI selection for both relaxometry and diffusion studies. To identify the sample and select a ROI approximately about 80% of the sample diameter, which is defined as ROI_1, tresholding was used as seen in Fig 3.8.

The reason to choose 80% of the maximum sample diameter instead of higher percentage was to prevent the interface region of the container being used. Avoidance of noise floor fitting was curicial as will become clear in the following sections. Thus, phantom-air contrast, where the “air” ROI is defined as ROI_2, was stated as all voxels outside a circle around 1.2 times of the sample (Fig 3.8).

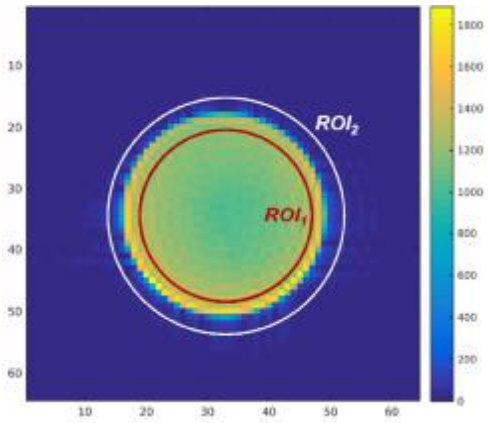

Figure 3.8. Sample image with automatic ROI selection (ROI_1) and background selection (ROI_2) for noise signal estimation

3.4.1. Relaxometry Measurements

Relaxation time (T_1 and T_2) measurements were performed on a Siemens 3T Magnetom Skyra (Erlangen, Germany) scanner in this work with a four-channel spine coil (SP2) element using SE sequences with different chosen T_E and T_R times. In addition, relaxation rates of R_1 ($1/T_1$) and R_2 ($1/T_2$) were determined using the protocols summarized in Table 3.3.

Table 3.3. Relaxation rate protocols used to characterize gel phantoms

Relaxation time (ms)	T_1	T_2
Sequence	Vendor-suplied SE	Vendor-suplied multi SE
T_E ***(ms)***	12	n·15 (n=1 to 32)
T_R ***(ms)***	125, 250, 500, 1000, 2000, 3000, 4000, 6000, and 7000	6000
FOV (mm)	100 x 100	100 x 100
Matrix size (pixels)	128 x 128	128 x 128
Readout bandwidth (Hz/Pixel)	130	130

As seen in Table 3.3, T_1 was determined by a saturation recovery protocol, which includes repeated scans consisting of a 90° excitation pulse and a 180° refocusing pulse using a fixed T_E and different T_R values. To determine T_2, a long-fixed T_R value was used to ensure adequate longitudinal magnetization recovery and to prevent stimulated echo effects, with a 10 mm slice thickness.

After the automatic ROI selection mentioned above, the mean and SD of the signal over the ROI were obtained for each image of the gel phantoms. The following equations were used to determine T_1 and T_2 relaxation times, respectively;

$$I(T_R) = I_0 \left[1 - e^{\left(-\frac{T_R}{T_1}\right)}\right] \tag{3.1}$$

$$\log I(T_E) = -\frac{T_E}{T_2} + a_0 \tag{3.2}$$

a_0 is the constant parameter defined as $a_0 = \log(I_0)$, where I_0 is constant associated with the spin density, coil sensitivities, and equilibrium magnetization.

3.4.2. DW-MRI and DKI Measurements

DW-MRI experiments were performed on a Siemens 3T Magnetom Skyra (Erlangen, Germany) scanner at Swansea University with a combination of a 7 cm diameter (medium) loop and a four-channel spine coil element (SP2) to boost the diffusion-weighted Signal (Fig 3.9a).

Different coil combinations as well as single coils were tested by evaluating the SNR of DW-MRI scans at the beginning of the study. The spine and loop coil (Fig 3.9b) combination provided the best results with the highest SNR on each image at 3T MRI scanner. All gel phantoms were located in the center of the loop coil, which was placed on the spine coil (Fig 3.9c).

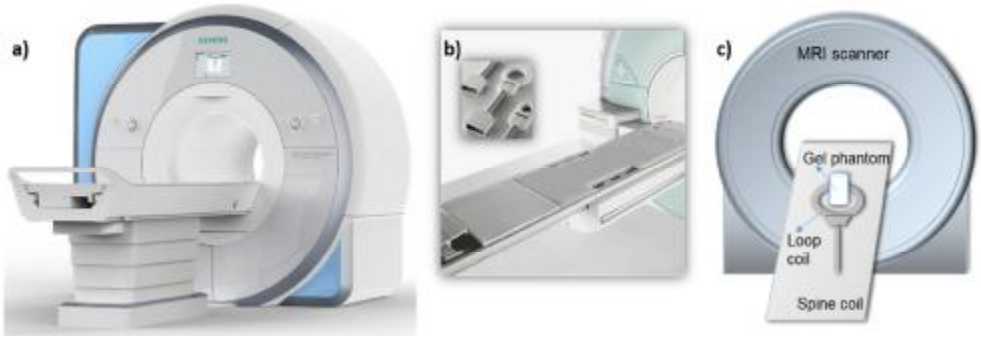

Figure 3.9. a. Siemens Magnetom Skyra 3T scanner, b. Loop and spine coils of the scanner (web4, 2018), c. Location of gel phantoms with coils

DW-MRI images were performed using an in-house version of the Stejskal–Tanner (PGSE) sequence (Stejskal and Tanner, 1968). The sequence was written by Dr. Shermer in the Siemens IDEA C++ programming environment. While the sequence parameters were defined, "*G*" was calculated for each required b-value because δ and Δ were fixed. For hydrogen nuclei, $\gamma/2\pi$ = 42.576 MHz/T and thus γ = 267.5 MHz/T. The gradient parameters used were similar to those used in the vendor-supplied product sequence, specifically δ = 33 ms, Δ = 71 ms, and t_{rise} = 500 μs, and the gradient amplitudes calculated related to the b-value (between 0 and 4000 s/mm^2 in intervals of 500) required (Table 3.4). The details of the set parameters of the sequence using Eq. 3.3 is summarized below;

$$b = (\gamma G \delta)^2 \left(\Delta - \frac{\delta}{3}\right) \qquad G = \frac{1}{\gamma\delta}\sqrt{\frac{b}{(\Delta - \delta/3)}} \tag{3.3}$$

Table 3.4.Calculated gradient amplitudes for PGSE sequence

b-value (s/mm^2)	G (mT/m)	b-value (s/mm^2)	G (mT/m)
500	10.34	*2500*	23.12
1000	14.63	*3000*	23.98
1500	17.91	*3500*	25.33
2000	20.68	*4000*	29.25

The reason for not using a vendor-suplied diffusion sequence was the priority of data quality over rapid acquisition. To prevent effects such as image blurring, localized signal loss, image distortions caused by eddy currents (Farzaneh et al., 1990; Bammer et al., 2009; NEMA MS 1-2001), and other artifacts observed with the standard EPI diffusion sequence, the scans were performed using normal Cartesian k-space readout rather than SS-SE-EPI.

The parameters for the PGSE phantom scans were;

FOV	:	100 x 100 mm
Matrix size	:	64 x 64
TE	:	120 ms
TR	:	3000 ms
Bandwidth	:	130 Hz/pixel
Slice thickness	:	20 mm

The first four b-values of 0, 500, 1000, 1500 s/mm^2 were used for the linear fit only, while all nine b-values were used for the quadratic fit. Note that the parameters chosen were identified as an optimum in preliminary test studies.

In MRI, the SNR can be improved by choosing SE sequences rather than GRE, increasing the number of excitations (NEX), T_R, field of view (FOV), and slice thickness, and decreasing T_E, matrix size, and bandwidth. FOV specifies area covered by an MR image, usually specified in mm x mm and subdivided into several hundred picture elements (pixels). This image area consists of two factor as the number of pixels (rows x columns) is the matrix and the depth is the slice thickness (Fig 3.10). The range of radiofrequencies or wavelengths that can be transmitted or received within a limited time is the bandwidth (cycles per second or Hertz per pixel). The receiver bandwidth explains the MRI signal quality. Decreasing the bandwidth extends the sampling time. Therefore, signal amplitude increases and the noise level in pixels decreases resulting in an increase in SNR.

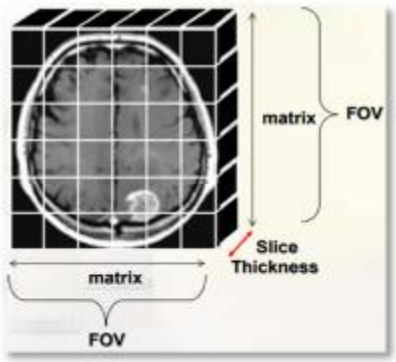

Figure 3.10. Definition of FOV, matrix size, and slice thichness on MRI image (web5, 2018)

NEX, also known as number of averages (N_A), is generally proportional to the square of the SNR. However, imaging time is also directly proportional to N_A and thus, we chose only one average for our isotropic and homogeneous gel phantoms. Shorter T_E is preferable to minimize signal loss due to T_2 decay, while long T_R is preferable to maximize magnetization recovery between acquisitions. SNR can be expressed as follows (web6, 2018);

$$SNR \propto \Delta V . \sqrt{\frac{N_{PE} . N_A}{BW}} \tag{3.4}$$

$$\Delta V = \left(\frac{FOV_x}{N_x}\right) . \left(\frac{FOV_y}{N_y}\right) . \Delta z \tag{3.5}$$

$$N_{PE} = \begin{matrix} N_y & (Multislice) \\ N_y . N_z & (3D) \end{matrix} \tag{3.6}$$

where N_x is frequency encoding (readout) and N_y is in-plane phase matrix size, N_z is number of slices, Δz is slice thickness. The FOVs in the x, y, and z directions represent FOV in the readout, phase encoding and slice directions, respectively.

SNR is used to describe the performance of MRI system. Thus, SNR values were examined to decide the set parameters explained above in detail. NEMA guidelines (2001) provide four different methods to compute SNR. The preferred choice is method 1, which requires the acquisition of two images with the same acquisition parameters and computation of a difference image. However, it is not practical to acquire dublicate images for every single gel and diffusion weighting. Thus, method 4 was chosen by measuring signal in ROI_1 within the object and the noise in ROI_2 within the background of the MRI image. Then, SNR is equal to the ratio of signal over noise using Eq. 3.7.

$$SNR \pm SD = \frac{Signal \pm SD}{Noise \pm SD} \tag{3.7}$$

3.4.3. Comparing the Use of Different Pulse Sequences for DKI

Comparison experiments were performed in two clinical MRI systems. In addition to 3T scanner, a GE Optima MR450w 1.5T (Waukesha, WI) scanner at Velindre Cancer Centre was also used with a birdcage head coil (see Fig 3.11).

Figure 3.11. GE Optima MR450w 1.5T scanner with birdcage coil (web7, 2018)

In the second phase, plain and gm included agar gel phantoms were scanned using vendor-suplied SS-SE-EPI sequence by both 1.5 and 3T scanners.

Table 3.5. Imaging protocols for the DKI scans

MRI scanner	**GE 1.5T**	**Siemens 3T**	**Siemens 3T**	**Siemens 3T**
Sequence	***SS-SE-EPI***	***SS-SE-EPI***	***SE-ST (PGSE)***	***SE-ST (PGSE)***
FOV (mm) *Field of View*	100	100	100	64
Matrix size *(Rows x columns)*	256 x 256	64 x 64	64 x 64	64 x 32
Slice thickness (mm)	20	10	20	10
T_R/T_E ***(ms)*** *Repetition/Echo time*	5000/130	5000/130	3000/120	3000/120
Bandwidth (Hz/px) *Receiver bandwidth*	1000	1000	130	130
N_A *Number of averages*	8	8	1	1
b-values (s/mm^2) *Degree of dif. weighting*	9 b-values	9 b-values	9 b-values	9 b-values
T_A ***(min)*** *Acquisition time*	6.45	6.07	27.81	11.97
Coil *Receiver array coils*	Birdcage	Spine, loop	Spine, loop	Spine, loop

Additionally, small changes were applied to modify the PGSE sequence to reduce the acquisition time (T_A) and that sequence was used to compare as well. DKI imaging protocols are summarized in Table 3.5. It should be noted that all the factors used in each protocol have been chosen to be the same or similar as possible depending on the device/software possibilities.

The methodology is to evaluate DKI data (diffusion coefficients, kurtosis and signal attenuation curves) and the reliability of kurtosis estimates (pseudo-kurtosis) using different sequences and scanners using phantoms. Image quality was compared between the protocols used in images acquired with each b-value from both manufacturers. Particular emphasis was given to identifying spatial distortions and signal losses from susceptibility artefacts or RF inhomogeneities in the images.

Thus, this part includes the following steps;

- Estimation of $D_{(1)}$, $D_{(2)}$, and *K* for each protocol used,
- Evaluating the image qualities for each b-value used (from 0 to 4000 s/mm^2 in intervals of 500) to obtain possible artifacts,
- Evaluating "signal vs b-value" plots to check noise floor effect on calculated $D_{(2)}$ and *K* values and defining "the correct" and "pseudo" kurtosis.

4. RESULTS AND DISCUSSION

In multimodal imaging phantoms, there are crucial parameters to achieve a well-designed, proper, cost-effective, and robust phantom in terms of calibration, QA tests, sequence development, and protocol use. These qualitative and quantitative parameters are of great importance for target volume as explained in Chapter 1. The goal of this study is the evaluation and optimization of DKI sequences/protocols, and specifically the development of suitable phantoms for other advanced imaging modalities used in BT. Compared to previous work detailed in Chapter 2, the most important difference of this study was the development and characterization of a simple phantom that was both suitable for various imaging methods (including advanced modalities) and that yields kurtosis values that can approximate tissues of interest. The results obtained in the light of the categorized methods in Chapter 3 are summarized in four main headings as mentioned below.

- Section 4.1 presents the main physical parameters with qualitative image results for CT and US/Elastography methodologies. Attention has been paid to the use of different devices or methods to try to broaden the range of successes in the areas of phantom use and the results have been stated.
- Section 4.2 shows the results of the relaxometry experiments, i.e. the T_1 and T_2 times and corresponding relaxation rates of the gel phantoms.
- Diffusivity properties of the gel phantoms are presented and discussed for both Gaussian and non-Gaussian diffusion methodologies in Section 4.3.
- The significance of “pseudo-kurtosis” is demonstrated and discussed in Section 4.4 with the results of different DKI protocols used in different scanners. Protocol comparison results have been evaluated.

4.1. Physical Properties of the Phantoms using CT and US/Elastography

4.1.1. Physical Properties of the Phantoms using CT

The CT scans are solely used to obtain HUs as one of the physical parameters as well as to assess the consistency of the phantoms, which are not designed to be tissue-mimicking CT phantoms. Density and HU values of the gel phantoms are shown in Table 4.1 and 4.2 for plain and gm added gel phantoms.

Table 4.1. Density and HU values of plain gel phantoms

Gel Phantom Material	Density (kg/m^3)	$HU_{(1)}$	$HU_{(2)}$
1.0% Agar	1016	5 ± 3	5 ± 2
1.5% Agar	1021	6 ± 3	6 ± 2
2.0% Agar	1026	8 ± 3	8 ± 1
2.5% Agar	1031	9 ± 3	8 ± 2
3.0% Agar	1036	11 ± 3	11 ± 2
3.5% Agar	1041	13 ± 2	13 ± 2
0.5% Agarose	1011	3 ± 3	1 ± 1
1.0% Agarose	1016	4 ± 3	2 ± 1
1.5% Agarose	1021	6 ± 3	5 ± 2
2.0% Agarose	1026	8 ± 3	6 ± 1
2.5% Agarose	1031	10 ± 3	5 ± 4
3.0% Agarose	1036	12 ± 3	7 ± 2
10.0% PVA-C (2ft)	1056	21 ± 1	19 ± 2
10.0% PVA-C (3ft)	1056	21 ± 1	16 ± 2
10.0% PVA-C (4ft)	1056	22 ± 2	16 ± 4
10.0% PVA-C (5ft)	1056	21 ± 1	16 ± 1
15.0% PVA-C (4ft)	1066	29 ± 3	28 ± 2
20.0% PVA-C (4ft)	1106	37 ± 3	40 ± 4

Table 4.1 shows the HU values obtained from Definition AS ($HU_{(1)}$) and Sensation 64 ($HU_{(2)}$), respectively, using both Siemens CT scanners. HU values achieved from both scanners slightly increase with the concentration of plain gels. It is seen that there is not a big difference between the HUs depending on the scanner used, the HUs of agar phantoms are quite similar (Fig 4.1).

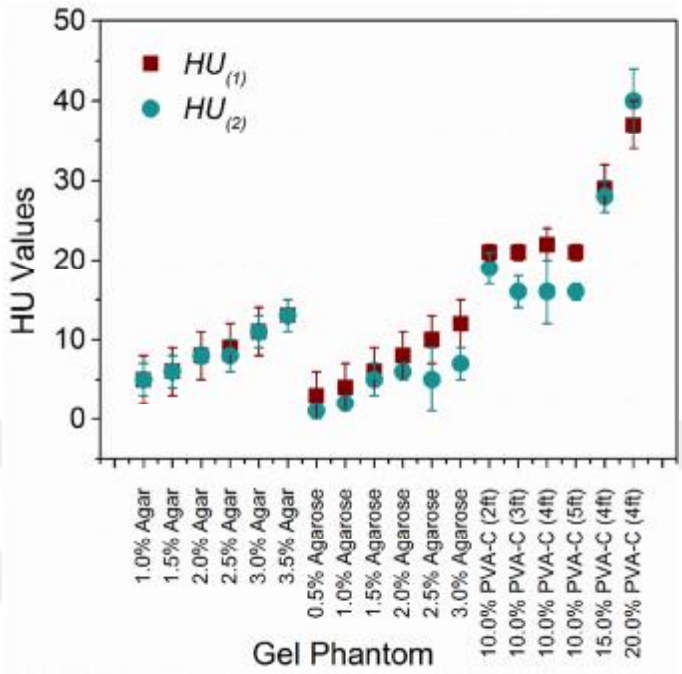

Figure 4.1. HUs of each plain gel phantoms according to the scanner type

When Table 4.1 and Fig 4.1 are examined, it is seen that the HU values of the agar and agarose gel phantoms are very low and even close to the water, whereas the HU values of the PVA gel phantoms are higher. This is an expected situation because agar and agarose gels are prepared in very low concentrations. They can be considered approximately water equivalent, and the densities are also very close to the water. These HU values of plain agar and agarose gel phantoms are smilar to those of various lymph nodes which define breast cancer metastasis (Urata et al., 2014). The HU range of PVA phantoms are close to those of kidney, spleen, liver, and prostate (Lamba et al., 2014; In, 2016).

HU values of the gel phantoms including gm were achieved by using Siemens Somatom Definition AS (Table 4.2). The values of agar and agarose gels with gm are almost stable for the ones with the same amount of gm. However, it is observed that HU decreases linearly when the concentration of microspheres is increased for agar gels but it is almost stable for the agarose ones (Fig 4.2).

Table 4.2. Density and HU values of gel phantoms including gm

Gel Phantom Material with gm	Density (kg/m^3)	HU
1.0% Agar 2.0g gm	1036	-60 ± 7
1.5% Agar 2.0g gm	1041	-59 ± 5
2.0% Agar 0.1g gm	1027	8 ± 2
2.0% Agar 0.3g gm	1029	7 ± 4
2.0% Agar 1.0g gm	1036	-22 ± 4
2.0% Agar 2.0g gm	1046	-58 ± 4
2.0% Agar 3.0g gm	1056	-90 ± 4
2.5% Agar 2.0g gm	1051	-61 ± 4
3.0% Agar 0.05g gm	1036	11 ± 3
3.0% Agar 0.1g gm	1037	9 ± 2
3.0% Agar 1.0g gm	1046	-16 ± 3
3.0% Agar 2.0g gm	1056	-56 ± 3
3.0% Agar 3.0g gm	1066	-97 ± 3
3.5% Agar 2.0g gm	1061	-56 ± 7
1.0% Agarose 0.1g gm	1017	5 ± 3
1.0% Agarose 0.5g gm	1021	7 ± 3
1.0% Agarose 1.0g gm	1026	8 ± 3
1.0% Agarose 2.0g gm	1036	10 ± 6
2.0% Agarose 0.1g gm	1027	10 ± 3
2.0% Agarose 1.0g gm	1036	8 ± 4
2.0% Agarose 2.0g gm	1046	-12 ± 15
3.0% Agarose 1.0g gm	1046	7 ± 5
Water	1000	0 ± 3

These negative values, which extend up to -100, generally correspond to fat tissue (In, 2016). The decrease to the negative values is because the bulk of low-density gm is air. For this reason, as the amount of gm increases, the amount of air in the gel increases and the HU value decreases to the negative (HU_{air} = -1000).

An inhomogeneous agar gel phantom was also scanned to test its image quality (see Fig 4.3).

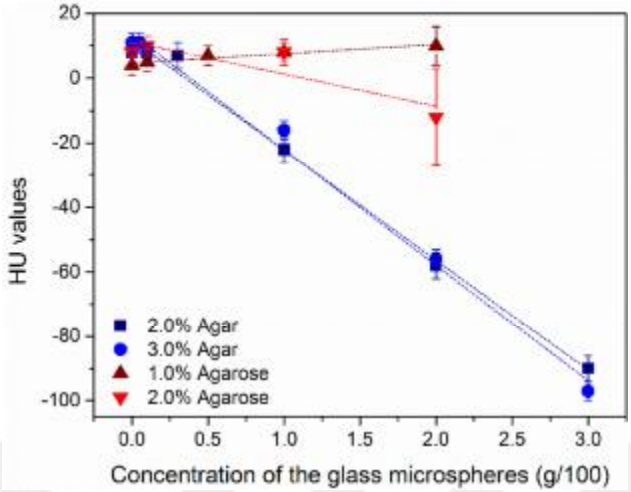

Figure 4.2. HU values as a function of concentration of the glass microspheres

Despite the fact that the density and HU differences are quite small for the heterogeneous agar phantom, the visual separation can easily be done by changing the window level or threshold in the software used (ImageJ).

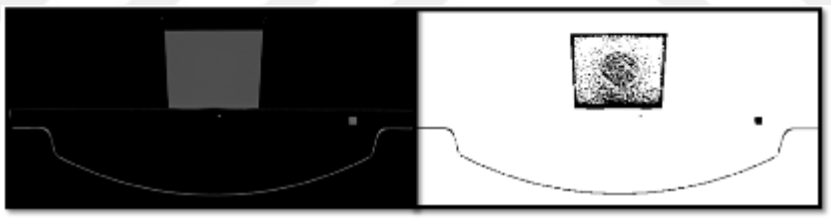

Figure 4.3. CT DICOM image of inhomogeneous agar gel phantom (left), image achieved by changing the threshold in ImageJ (right)

Furthermore, all gel phantoms were re-scanned after 6 months. It has been observed that agar and agarose gel phantoms gave similar results and stayed stable. However, water release over time was observed in PVA-C phantoms. PVA-C can be used to mimic soft tissue (e.g., prostate), but it has the clear disadvantage of being time-consuming to prepare and susceptible to dehydration effects. CT results suggest that it is possible to obtain stable and homogeneous phantoms using agar and agarose geling agents with varying concentrations of glass microspheres.

4.1.2. Physical Properties of the Phantoms using US/Elastography

Propagation speed and Young's modulus results of each prepared gel phantom using US/Elastography are summarized in Table 4.3, 4.4, and 4.5 for agar, agarose, and PVA-C, respectively. The main focus here was on characterization of plain gel phantoms. Then, a sample including glass microsphere was also tested to determine whether the values differ from the plain ones.

Table 4.3. Propagation and mechanical properties of agar gel phantoms

Concentration (%w,v)	Propagation Speed (m/s)	Young's Modulus (kPa)
1.0	3.13 ± 1.32	36.3 ± 23.8
1.5	3.41 ± 1.28	41.4 ± 26.5
2.0	3.69 ± 1.39	47.7 ± 29.2
2.0 (with gm)	3.34 ± 1.68	44.1 ± 32.5
2.5	3.74 ± 1.82	52.5 ± 37.2
3.0	4.26 ± 1.91	59.3 ± 38.2
3.5	4.41 ± 2.02	68.2 ± 42.0

Table 4.4. Propagation and mechanical properties of plain agarose gel phantoms

Concentration (%w,v)	Propagation Speed (m/s)	Young's Modulus (kPa)
1.0	1.55 ± 1.29	19.1 ± 15.7
1.5	1.89 ± 1.50	20.4 ± 24.0
2.0	1.91 ± 1.38	19.5 ± 21.4
2.5	2.14 ± 1.50	22.4 ± 22.3
3.0	2.22 ± 1.38	23.3 ± 23.4

Table 4.5. Propagation and mechanical properties of plain PVA-C gel phantoms

Concentration (%w,v)	Propagation Speed (m/s)	Young's Modulus (kPa)
10.0 (2ft)	2.01 ± 1.15	22.4 ± 20.4
10.0 (3ft)	2.31 ± 1.29	23.7 ± 20.7
10.0 (4ft)	2.43 ± 0.81	20.3 ± 13.4
10.0 (5ft)	3.10 ± 1.02	33.3 ± 18.3
15.0 (4ft)	1.69 ± 0.98	15.9 ± 12.8
20.0 (4ft)	2.03 ± 1.11	18.7 ± 14.7

As mentioned above, the scans were repeated to test both operator and positioning of the probe. Young's Modulus and propagation speed of agar gels showed a slight increase while those of agarose and PVA-C did not show much change as the concentration increased. Since SDs of the both Young's Modulus and propagation speed are too high for a proper quantitative analysis between the values and the concentration that can be seen in Fig 4.4 below, priority was given to a qualitative analysis of the images obtained.

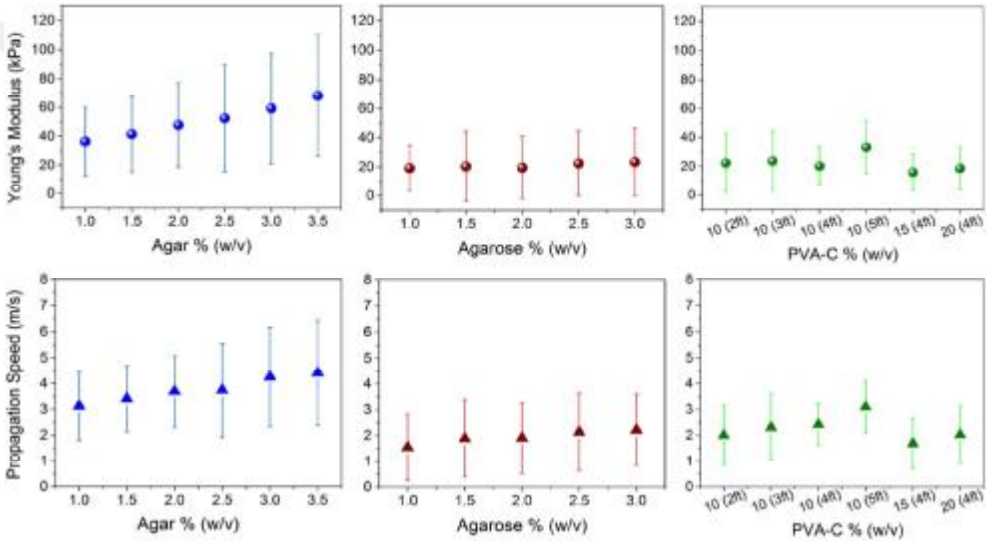

Figure 4.4. Young's Modulus (top) and propagation speeds (bottom) values of plain gel phantoms

Thus, image quality of the gel phantoms were evaluated. Agar and PVA-C phantoms exhibited better SWE image quality than the agarose phantoms. Especially, images of plain agarose gel phantoms with low concentrations were of bad quality due to the presence of air bubbles. Fig 4.5 shows images for 2.0% agar, 2.0% agarose, and 10.0% PVA (5ft) including shear wave propagation directions.

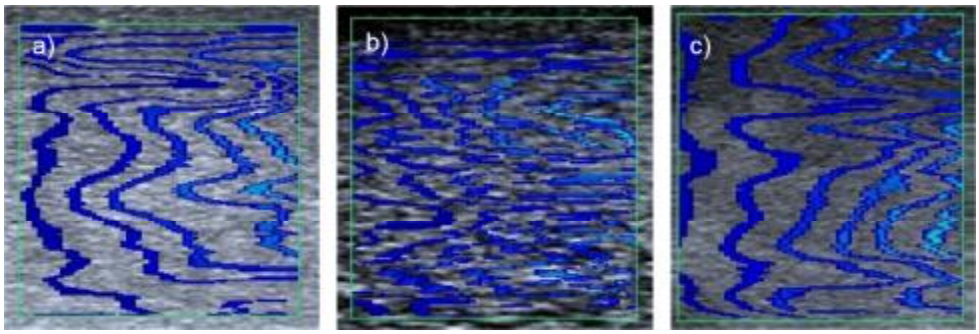

Figure 4.5. SWE images of a) agar, b) agarose, and c) PVA-C gel phantoms with their propagation speed directions

Note that, shear waves are different from compressional ultrasonic waves in several ways. The propagation velocity of a shear wave is much slower than the compressional wave and is dependent on the longitudinal modulus of elasticity of the biological tissue. The shear wave is the resulting disturbance that affects the surrounding tissue, in a direction parallel to the probe. Propagation and elasticity maps are formed when shear wave propagation speed is parallel to the direction of applied pulses. It is clearly seen that propagation speed directions are parallel in the large part of the images of agar and PVA-C phantoms.

In the second part of the US/Elastography evaluation, one of the phantoms including gm and one of the inhomogeneous phantoms were tested. Since plain agar and PVA-C gave better results than agarose, it was planned to prepare these additional two gels using agar and PVA gelling agents. However, PVA gelling agent could not be used due to the change in the structure occurred when the gm was added into the PVA solution. The quantitative repeated results of the 2.0% agar gel phantom including gm are presented in also Table 4.3. It is seen that gm addition did not change either propagation speed or Young's Modulus significantly which means the microspheres used do not affect the stiffness of the gel phantom.

For the inhomogeneous agar gel phantom (2.0% background and 3.0% inclusion part), both Shear wave and strain elastography methods were used to evaluate its image qualitatively (Fig 4.6 and 4.7).

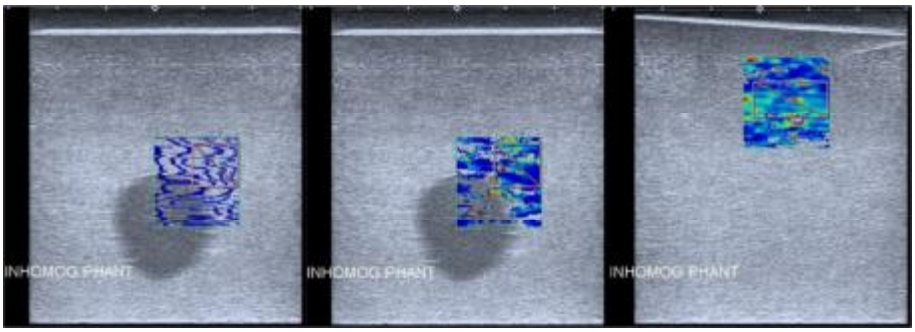

Figure 4.6. Propagation speed direction (left), coulor map by separating the areas having different elasticity properties (middle), and colour map of the background only (right)

Here in the Fig 4.6, darker area contains denser (3.0% agar) gel in which shear waves do not propagate. As mentioned in Chapter 3, the inclusion part was added within the background by removing the rod inside it after the background part (2.0% agar) was manufactured. Visual determination can be made easily for the areas with the different densities on the image. The background part of the phantom is quite homogeneous and the colour map is excellent (Fig 4.6, right).

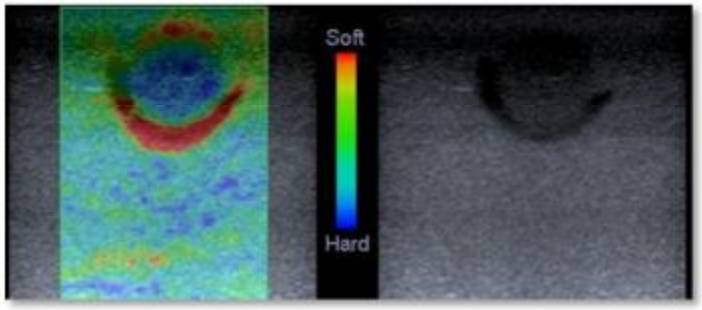

Figure 4.7. Strain Elastography scan of inhomogeneous agar gel phantom by applying a manual palpation

Smilarly, Strain Elastography image was obtained with a distinguishable image quality as seen in Fig 4.7. Thus, a successful image was achieved with inhomogeneous agar gel phantom for the US/elastography. It is seen that agar is a useful gelling agent in this advanced imaging modality.

4.2. Relaxation Properties of the Phantoms

T_1 and T_2 times of all prepared gel phantoms were calculated with an exponential fit by using Signal vs T_R and Signal vs T_E plots as explained in Section 3.4.1. One sample of agar gel results representing fitting plots is shown in Fig 4.8.

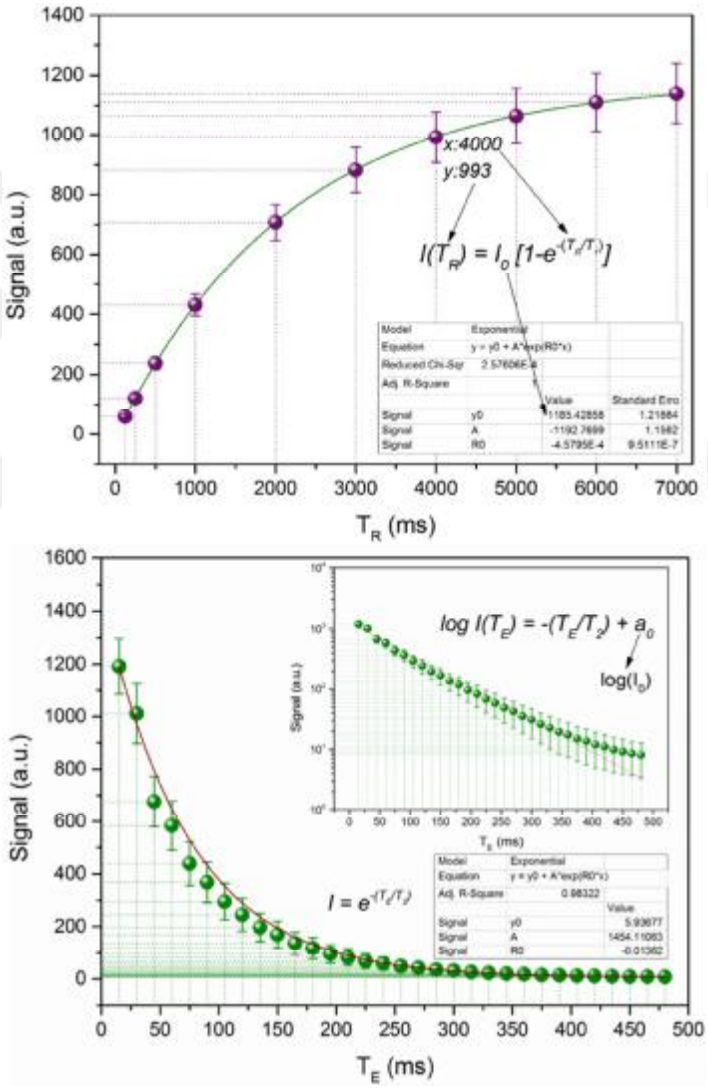

Figure 4.8. Mean signal over ROI as a function of T_R (by exponential fit) (top), T_E (by exponential and linear fits) (bottom) for 1.0% agar with 2.0g gm

Table 4.6 shows calculated T_1 and T_2 relaxation times of all prepared gel phantoms by comparing with the water.

Table 4.6. Relaxation times of the gel phantoms and the water

Gel Phantom Material	T_1 (ms)	T_2 (ms)	Gel Phantom Material with gm	T_1 (ms)	T_2 (ms)
1.0% Agar	2750±90	153±6	1.0% Agar, 2.0g	2230±77	75±8
1.5% Agar	2559±75	169±4	1.5% Agar, 2.0g	2341±65	62±3
2.0% Agar	2515±64	125±1	2.0% Agar, 0.1g	2397±154	82±1
2.5% Agar	2432±58	109±3	2.0% Agar, 0.3g	2637±53	83±1
3.0% Agar	2397±68	103±5	2.0% Agar, 1.0g	2304±90	86±3
3.5% Agar	2254±51	76±6	2.0% Agar, 2.0g	2153±50	59±3
0.5% Agarose	2862±83	204±3	2.0% Agar, 3.0g	2113±36	58±3
1.0% Agarose	2840±84	117±4	2.5% Agar, 2.0g	2101±26	49±10
1.5% Agarose	2707±73	83±1	3.0% Agar, 0.05g	2440±59	76±2
2.0% Agarose	2576±82	64±1	3.0% Agar, 0.1g	2438±52	76±2
2.5% Agarose	2544±74	53±3	3.0% Agar, 1.0g	2180±31	48±3
3.0% Agarose	2500±65	46±4	3.0% Agar, 2.0g	1951±33	40±4
10.0% PVA-C 4ft	1452±82	159±3	3.0% Agar, 3.0g	1882±24	35±3
15.0% PVA-C 4ft	1120±62	88±2	3.5% Agar, 2.0g	2088±29	49±9
20.0% PVA-C 4ft	936±42	73±1	1.0% Agarose, 0.1g	2760±178	103±1
Water	2825±365	2010±179	1.0% Agarose, 0.5g	2969±202	93±1
			1.0% Agarose, 1.0g	2934±228	82±1
			1.0% Agarose, 2.0g	2878±227	242±4
			2.0% Agarose, 0.1g	2800±170	55±1
			2.0% Agarose, 1.0g	2820±171	45±3
			2.0% Agarose, 2.0g	2695±108	42±5
			3.0% Agarose, 1.0g	2493±78	32±4

Table 4.6 and Fig 4.9 shows that T_1 decreases almost linearly with the concentration of the gelling agent for all of them (agar, agarose, and PVA-C). T_2 is also decreasing, which is not linear, as a function of the concentration for each gel phantom (Fig 4.10).

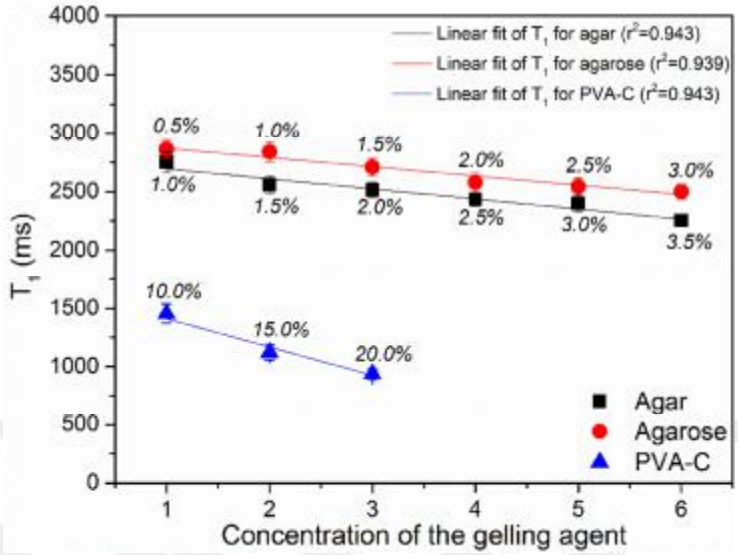

Figure 4.9. T_1 as a function of gelling agent concentration with a linear fit

It may be physically more meaningful to draw a plot of spin-spin relaxation rate, $R_2(1/T_2)$, as a function of gelling agent concentration than a plot of spin-spin relaxation time, T_2, shown in Fig 4.10 to get a connection between the parameters. Thus, the evaluation is done by R_2 versus the gelling agent concentration. R_2 increases almost linearly for each gelling agent, as expected.

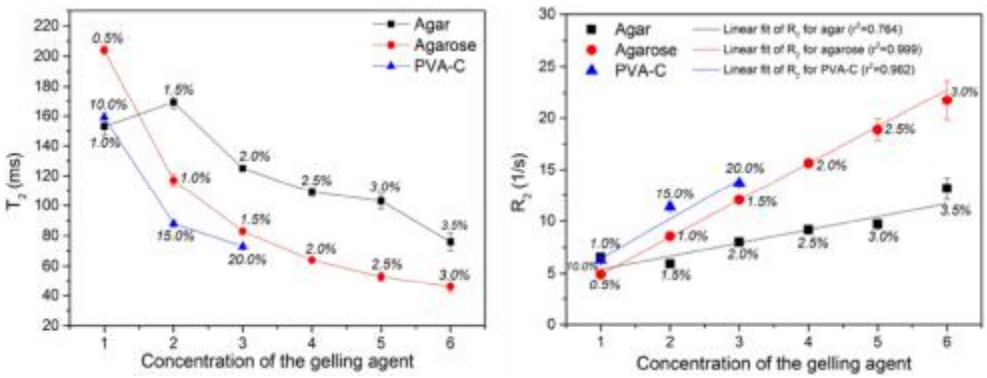

Figure 4.10. T_2 (left) and R_2 (right) as a function of gelling agent concentration

In agar and agarose gels including gm, two plots of T_1 and R_2 were drawn while the combined effect of microsphere addition and gel concentration was examined. Firstly, the relations between T_1 and R_2 corresponding to the gel concentration while the gm amount is fixed were achieved using agar gels with 2g gm and agarose ones with 1g gm (Fig 4.11 and 4.12).

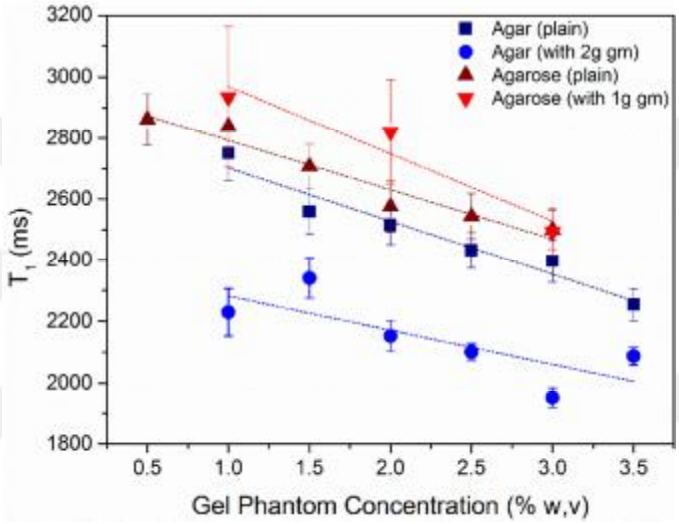

Figure 4.11. T_1 as a function of concentration of gelling agent with and without gm

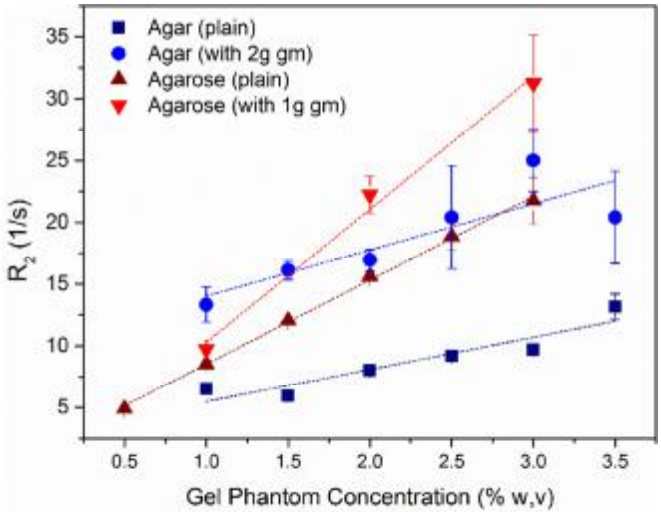

Figure 4.12. R_2 as a function of concentration of gelling agent with and without gm

As seen in Fig 4.11 and 4.12, the addition of gm decreases both T_1 and T_2 (increases R_2) for agar gelling agent while increases T_1 and decreases T_2 (increases R_2) for agarose if the concentration of the glass microspheres is kept fixed.

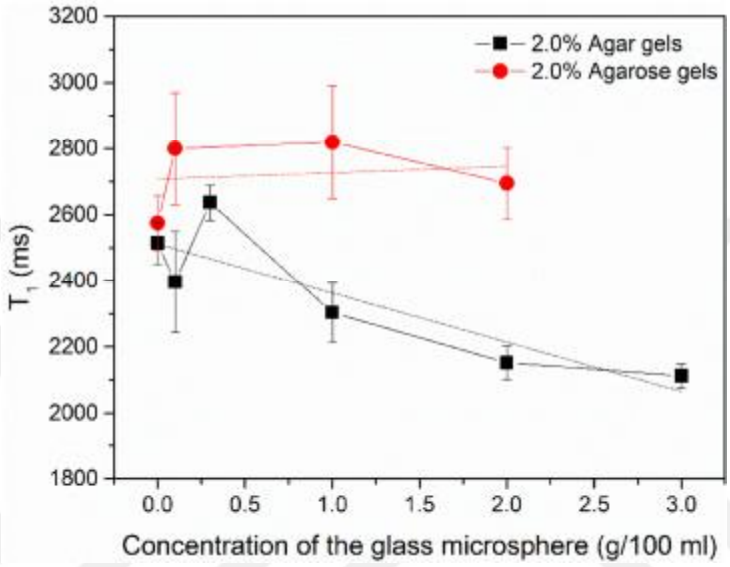

Figure 4.13. T_1 as a function of concentration of the glass microspheres

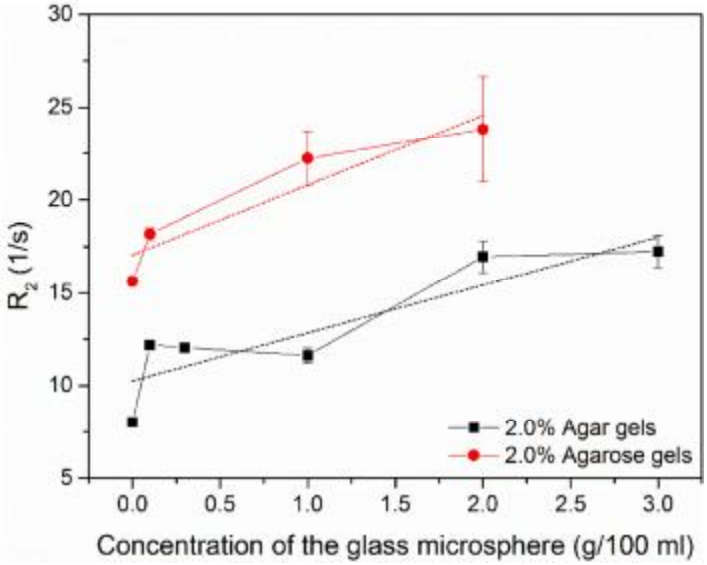

Figure 4.14. R_2 as a function of concentration of the glass microspheres

Fig 4.13 and 4.14 also show that when the concentration of the gelling agent is fixed, T_1 decreases while R_2 increases with increasing microsphere concentration for agar gels. For agarose gel phantoms, T_1 tends to increase with increasing microsphere concentration while R_2 also increases. T_2 decreases for each gelling agent as a function of gm, which can be understood from the Fig 4.14 with the increase of R_2. In general, the effect of gm addition on relaxation times is less pronounced for agarose than for agar.

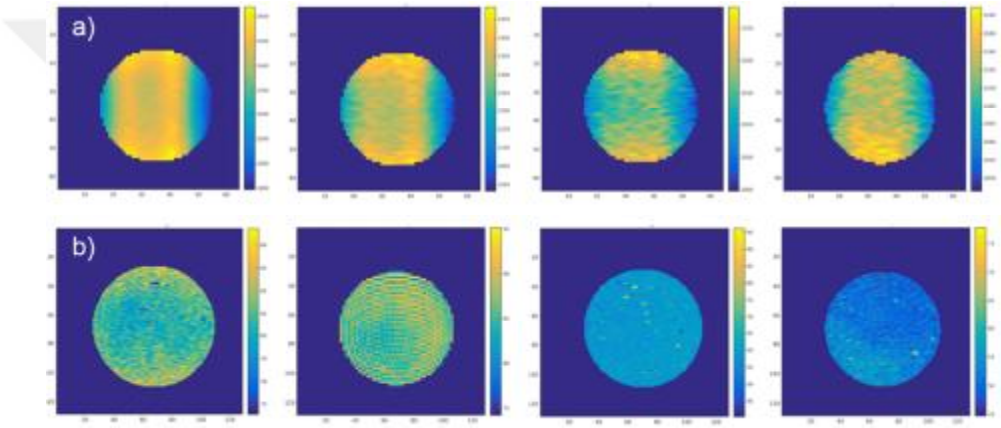

Figure 4.15. a. T_1, b. T_2 maps of 2.0% agar gels including gm with concentrations of 0.1, 1.0, 2.0, and 3.0 g, respectively.

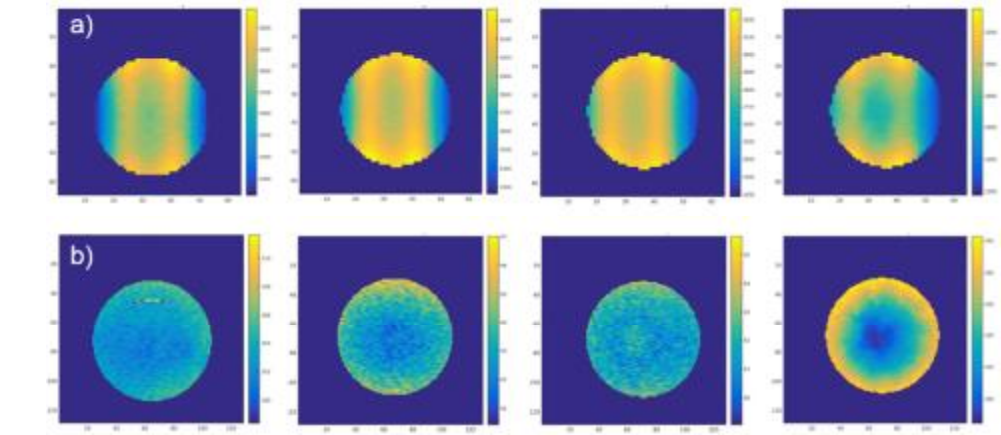

Figure 4.16. a. T_1, b. T_2 maps of 1.0% agarose gels including gm with concentrations of 0.1, 0.5, 1.0, and 2.0 g, respectively.

T_1 and T_2 maps were generated by fitting the signal intensities of each pixel within the defined ROI in the scanned image of each gel phantom using a coronal slice (Fig 4.15 and 4.16). As can be seen, when the expected relaxation time maps were obtained for the both two gel phantoms, a different T_2 map was achieved for 1.0% agarose phantom with 2g gm. In addition, the only different result shown in Table 4.6, which contains the general relaxation time results, belongs to this phantom. In 1.0% agarose gel phantom, T_2 decreased when the amount of added gm increased, but a substantial increase in the value was observed with the result of this phantom. For this reason, the relaxation scan was repeated and another gel phantom with the same concentration was prepared. The same results were found. While there is no considerable difference in spin-lattice relaxation time, such a difference in spin-spin time is interesting because external factors (such as magnetic field inhomogeneity) can reduce the T_2 time but generally do not increase it. Furthermore, small and rapidly rotating molecules (like free water) have long T_1 and T_2 times, T_2 shortents when molecular motion slows as in dense solids (web 8, 2018). Thus, further evaluations are done in the following section.

Characterization of the gel phantoms using relaxometry to quantify the effect of the gm on the T_1 and T_2 times suggests that high gm concentrations tend to modify the relaxation times/rates slightly. The relaxation times are appropriate for tissue-mimicking phantoms and they could easily be controlled by arranging the gelling agent concentration or the addition of T_1 or T_2 contrast agents.

As mentioned in Chapter 1, relaxation times of the soft tissue are in the range of 1412–1820 ms and 42–99 ms for T_1 and T_2, respectively. Pursuant to the achieved results, they were found for T_1 and T_2 as 1882–2750 and 35–169 ms, 2493–2969 and 32–242 ms, 936–1452 and 73–159 ms for all agar, agarose, and PVA-C gel phantoms, respectively. All prepared phantoms can represent soft tissue from T_2 time. However, it is seen that T_1 times were found close to the soft tissue with agar and PVA gels but very different for agarose ones. Thus, denser or more gm added agar gel phantoms may easily represent the soft tissue.

4.3. Diffusion Properties of the Phantoms

4.3.1. Results of DW-MRI Sequence Parameter Tests

Before the DW-MRI scans were performed, a series of tests was performed to assess the SNR of the images as a function of various parameters.

Table 4.7. SNR on b = 0 s/mm^2 images of 2.0% agar gel phantom with different Slice thickness (all other factors remain the same)

Slice Thickness (mm)	Signal-to-Noise Ratio (SNR)
20	135.56 ± 22.29
15	112.80 ± 18.32
10	69.60 ± 9.19
5	32.69 ± 5.06

Table 4.8. SNR on b = 0 s/mm^2 images of 2.0% agar gel phantom with different FOV (all other factors remain the same)

FOV (mm)	Signal-to-Noise Ratio (SNR)
100	32.88 ± 17.64
64	32.09 ± 24.18

Table 4.9. SNR on b = 0 s/mm^2 images of 10.0% PVA-C 4ft gel phantom with different T_R (all other factors remain the same)

T_R (ms)	Signal-to-Noise Ratio (SNR)
5000	44.51 ± 29.73
4000	65.39 ± 39.53
3000	59.09 ± 34.58
2000	48.30 ± 23.31
1000	26.84 ± 8.55
500	12.37 ± 2.72

Table 4.10. SNR on b = 0 s/mm^2 images of 10.0% PVA-C 4ft gel phantom with different T_E (all other factors remain the same)

T_E (ms)	Signal-to-Noise Ratio (SNR)
131	59.83 ± 26.27
200	64.67 ± 39.88
250	66.36 ± 44.52
300	79.51 ± 56.13
350	77.69 ± 68.70

As summarized in Tables 4.7 and 4.8, SNR increased when both of FOV and slice thickness increased as explained in Section 3.4.2. For each gel samples, different slice thickness and FOV tests were applied and only one of them is represented in Table 4.7. SNR was improved by increasing slice thickness for all samples and 20 mm was chosen for the further studies. Larger FOV values were also tested (150 and 200 mm) for 10.0% PVA-C 4ft gel phantom but a slight decrease was observed with the FOV increase. Thus, 100 mm was chosen the optimum FOV for each DW-MRI measurement as also shown in Table 4.8. T_R value of 4000 ms supplied the highest SNR (Table 4.9). However, 3000 ms was chosen to reduce acquisition time. As expected, possible shortest T_E time giving a proper SNR was obtained by 131 ms with a low SD value (Table 4.10).

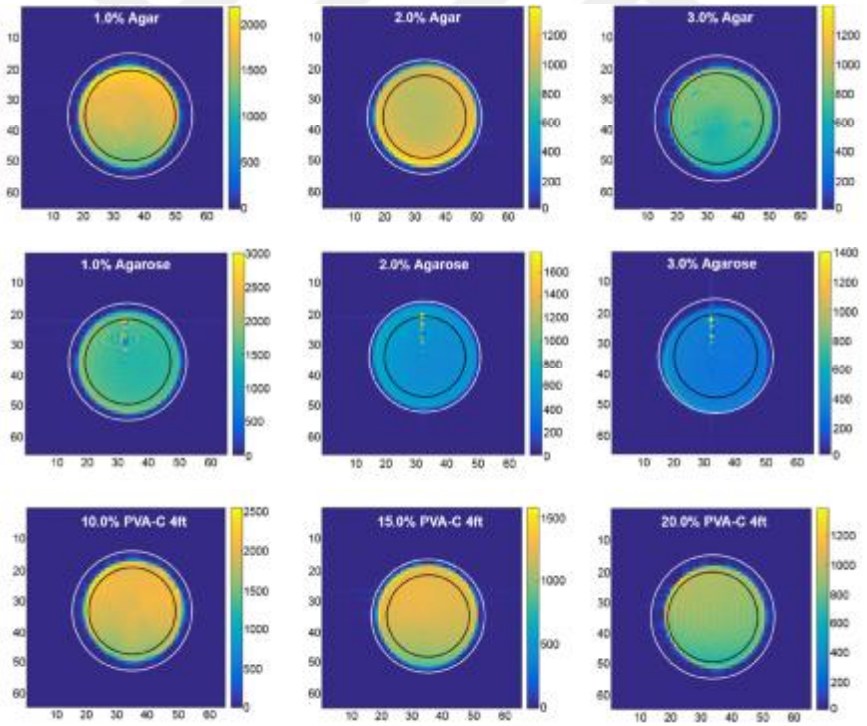

Figure 4.17. Automatically selected ROIs over the signal of the gel phantoms during DW-MRI analysis

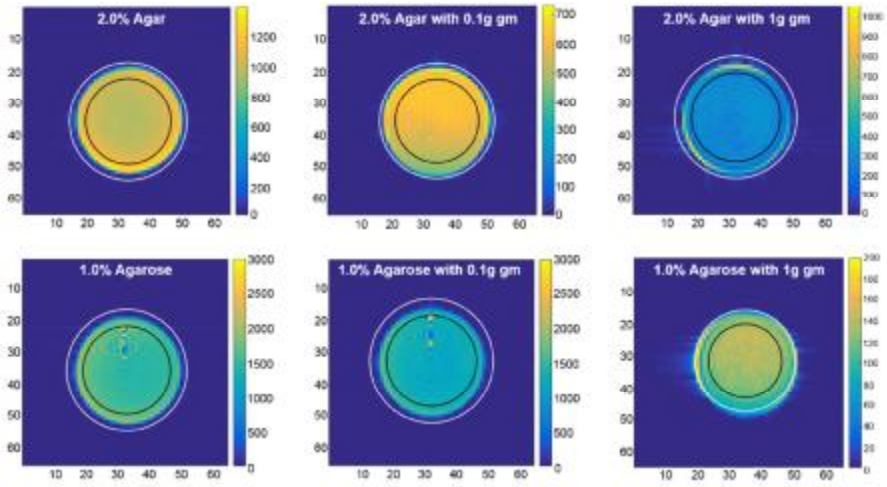

Figure 4.18. Automatically selected ROIs over the signal of the gel phantoms including gm during DW-MRI analysis

All diffusion analyses were achieved by using the signal values within the automated defined ROIs as explained in Section 3.4 (Fig 4.17 and 4.17). Signal loss with the increase of the concentration of both gelling agent and gm is seen.

4.3.2. Results of Calculated Diffusion Coefficients and Kurtosis

The apparent diffusion coefficient, ADC ($D_{(1)}$) obtained from linear exponential fit of the data using Gaussian monoexponential model with diffusion coefficient, $D_{(2)}$ and kurtosis K obtained from the quadratic exponential fit using kurtosis model of the data in the diffusion-weighted image are presented in Tables 4.11 and 4.12. As seen in Fig 4.19, $D_{(1)}$ is lower than $D_{(2)}$ for all gelling agents. $D_{(1)}$ decreases slightly with concentration of the gelling agent for all plain gel phantoms. However, $D_{(2)}$ remains almost constant for agar and agarose but decreases for PVA-C. In general, it is seen that the ADC ($D_{(1)}$) obtained with the monoexponential model is lower than $D_{(2)}$ when bigger b-values are used. This suggests that diffusion does not fit into the Gaussian distribution even though the density of the plain and homogeneous gel phantoms is very similar to the water and the presence of kurtosis increases as the barrier concentration increases.

Table 4.11. Diffusion parameters of plain gel phantoms

	$D_{(1)}$ ($\mu m^2/s$)	$D_{(2)}$ ($\mu m^2/s$)	K
1.0% Agar	2184 ± 44	2288 ± 90	0.050 ± 0.021
1.5% Agar	2133 ± 43	2308 ± 112	0.102 ± 0.021
2.0% Agar	2134 ± 28	2303 ± 91	0.094 ± 0.018
2.5% Agar	2121 ± 61	2329 ± 106	0.124 ± 0.018
3.0% Agar	2078 ± 30	2318 ± 157	0.126 ± 0.026
3.5% Agar	2055 ± 39	2694 ± 484	0.216 ± 0.031
0.5% Agarose	2308 ± 117	2424 ± 69	0.060 ± 0.017
1.0% Agarose	2259 ± 91	2344 ± 61	0.059 ± 0.013
1.5% Agarose	2222 ± 120	2362 ± 47	0.089 ± 0.009
2.0% Agarose	2186 ± 179	2355 ± 94	0.106 ± 0.017
2.5% Agarose	2198 ± 254	2458 ± 247	0.137 ± 0.034
3.0% Agarose	2028 ± 72	2267 ± 179	0.133 ± 0.030
10.0% PVA-C 4ft	1855 ± 28	2210 ± 215	0.200 ± 0.028
15.0% PVA-C 4ft	1631 ± 25	1890 ± 150	0.207 ± 0.030
20.0% PVA-C 4ft	1421 ± 21	1586 ± 102	0.183 ± 0.037

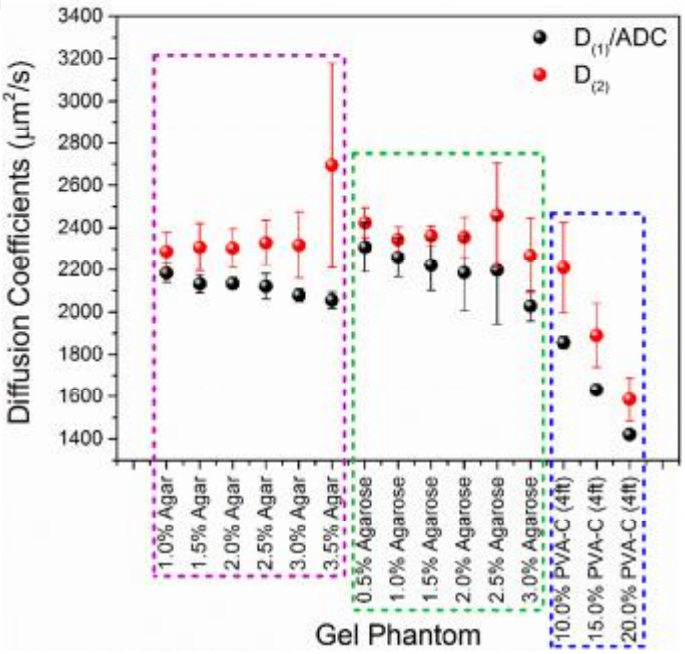

Figure 4.19. $D_{(1)}$ and $D_{(2)}$ as a function of gelling agent concentration

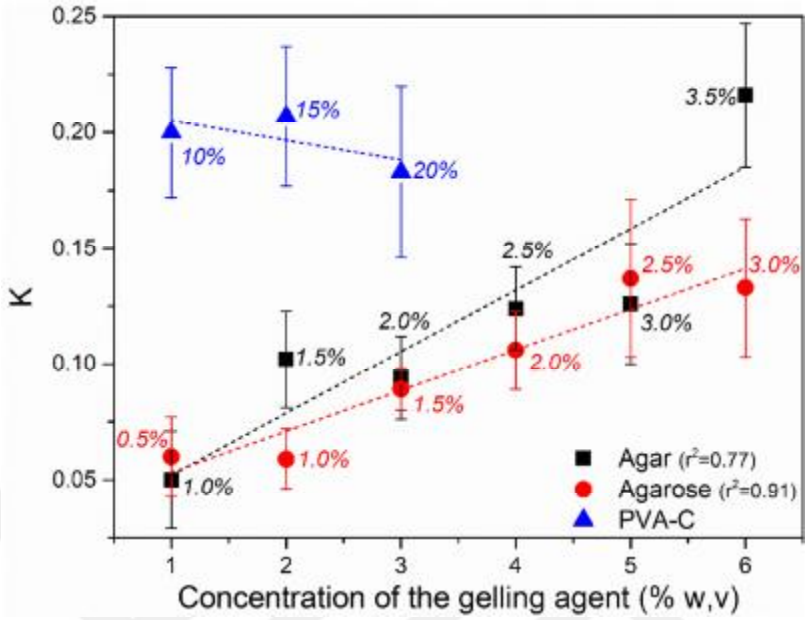

Figure 4.20. *K* as a function of gelling agent concentration

Kurtosis increases approximately linearly when the concentration of agar and agarose gels increases but remains almost constant for PVA-C gels (Table 4.11 and Fig 4.20). It is clearly seen that kurtosis for plain gels is limited and does not cover the full range of values observed for biological tissue stated in Chapter 1 even for high concentrations.

The resuls of agar and agarose gels including various amount of gm are plotted according to the diffusion coefficients $D_{(1)}$ and $D_{(2)}$ in Figs 4.21 and 4.22, and kurtosis *K* in Figs 4.23 and 4.24. In Fig 4.21, both diffusion coefficients $D_{(1)}$ and $D_{(2)}$ decrease with the amount of gm added into agar gels at both concentrations (2.0 and 3.0%) increases. This relation was observed better in 2.0% agar gels. In agar gel phantoms with the same amount of gm added, $D_{(1)}$ and $D_{(2)}$ decreased as the concentration increased. It can be seen as the amount of gm added in both agar gels increases, kurtosis *K* increases directly proportional. Even the relationship between them is linear and this linearity is better for 2.0% agar gel phantoms (Fig 4.23).

Table 4.12. Diffusion parameters of gel phantoms including gm

	$D_{(1)}$ ($\mu m^2/s$)	$D_{(2)}$ ($\mu m^2/s$)	*K*
1.0% Agar, 2.0g	1372 ± 349	1573 ± 130	0.435 ± 0.020
1.5% Agar, 2.0g	923 ± 141	1030 ± 47	0.449 ± 0.027
2.0% Agar, 0.1g	2066 ± 51	2421 ± 204	0.177 ± 0.023
2.0% Agar, 0.3g	1945 ± 137	2215 ± 73	0.189 ± 0.010
2.0% Agar, 1.0g	1498 ± 238	1723 ± 101	0.330 ± 0.006
2.0% Agar, 2.0g	986 ± 232	1115 ± 89	0.466 ± 0.035
2.0% Agar, 3.0g	818 ± 233	898 ± 79	0.523 ± 0.058
2.5% Agar, 2.0g	1097 ± 476	1202 ± 179	0.518 ± 0.052
3.0% Agar, 0.05g	2012 ± 71	2326 ± 123	0.190 ± 0.015
3.0% Agar, 0.1g	1913 ± 101	2200 ± 77	0.212 ± 0.009
3.0% Agar, 1.0g	1227 ± 216	1366 ± 66	0.351 ± 0.020
3.0% Agar, 2.0g	979 ± 303	1102 ± 88	0.523 ± 0.033
3.0% Agar, 3.0g	1124 ± 204	1231 ± 162	0.449 ± 0.006
3.5% Agar, 2.0g	1082 ± 246	1223 ± 110	0.476 ±0.033
1.0% Agarose, 0.1g	2061 ± 123	2340 ± 88	0.168 ± 0.011
1.0% Agarose, 0.5g	2252 ± 34	2547 ± 192	0.126 ± 0.025
1.0% Agarose, 1.0g	1962 ± 97	2227 ± 102	0.196 ± 0.013
1.0% Agarose, 2.0g	2257 ± 139	2562 ± 159	0.127 ± 0.009
2.0% Agarose, 0.1g	2158 ± 46	2542 ± 177	0.182 ± 0.017
2.0% Agarose, 1.0g	1890 ± 79	2181 ± 98	0.203 ± 0.013
2.0% Agarose, 2.0g	1617 ± 169	1824 ± 44	0.262 ± 0.008
3.0% Agarose, 1.0g	1355 ± 159	1499 ± 141	0.289 ± 0.041

In agarose gel phantoms, the relations between the gm concentration vs diffusion coefficients and kurtosis are slightly different. In Fig 4.22, both diffusion coefficients $D_{(1)}$ and $D_{(2)}$ decrease as the amount of gm added into 2.0% agarose gels increases. However, almost no change was observed for 1.0% agarose gels. Thus, the relation was observed better in 2.0% agarose gels. In agarose gel phantoms with the same amount of gm added, $D_{(1)}$ and $D_{(2)}$ decreased as the concentration increased like the agar ones. It can be seen as the amount of gm added in 2.0% agar gels increases, kurtosis *K* increases aproximetly linear (Fig 4.24).

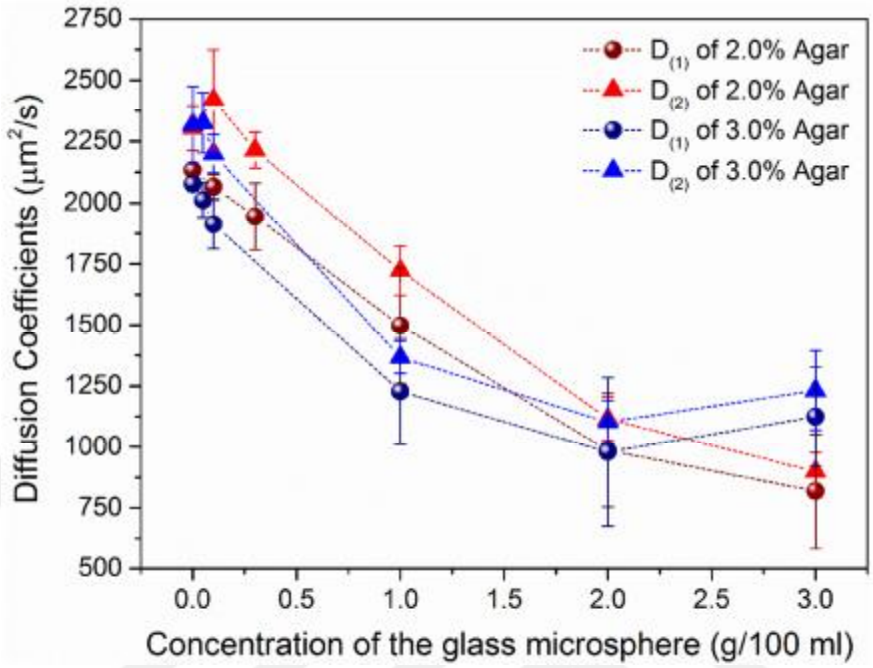

Figure 4.21. $D_{(1)}$ and $D_{(2)}$ as a function of gm for 2.0 and 3.0% agar gel phantoms

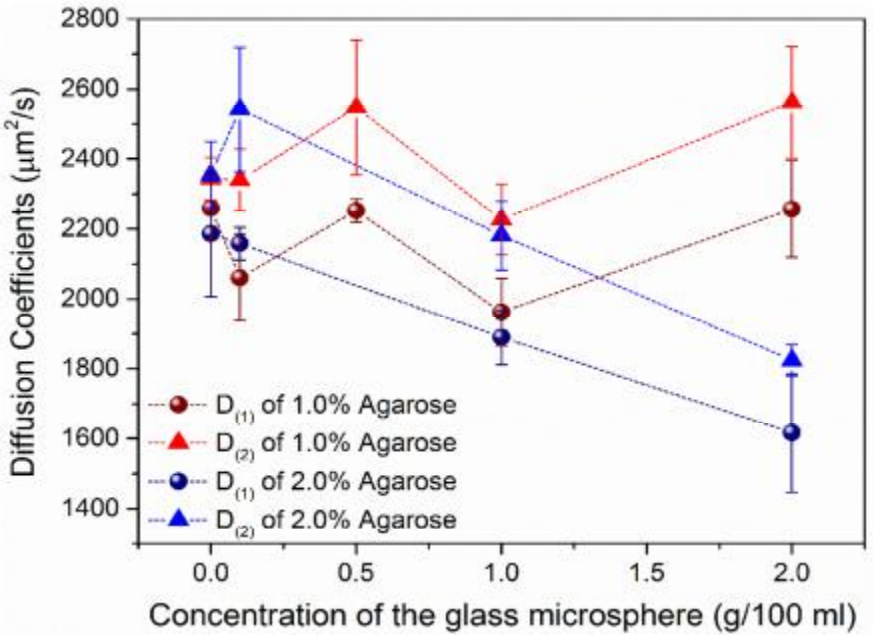

Figure 4.22. $D_{(1)}$ and $D_{(2)}$ as a function of gm for 1.0 and 2.0% agarose gel phantoms

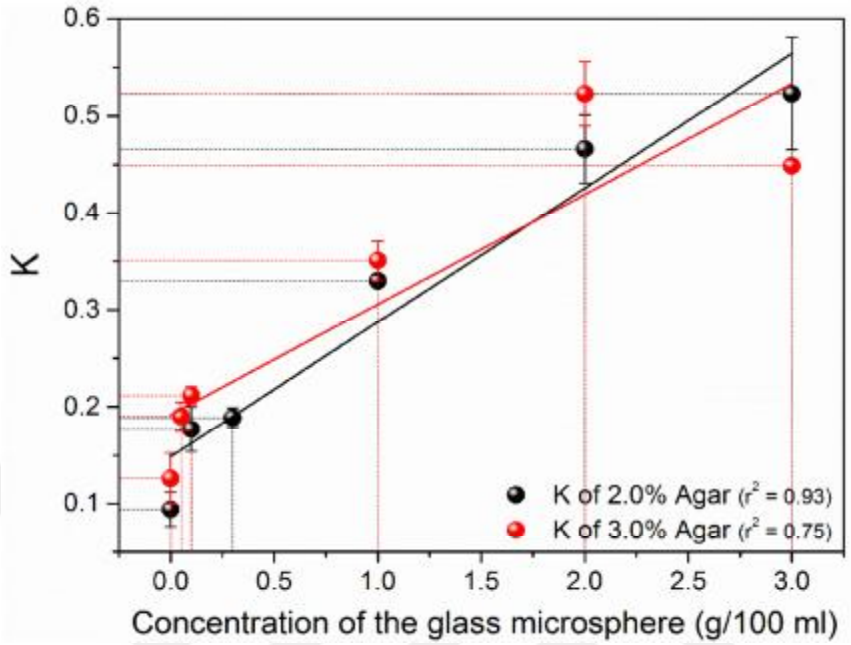

Figure 4.23. *K* as a function of gm for 2.0 and 3.0% agar gel phantoms

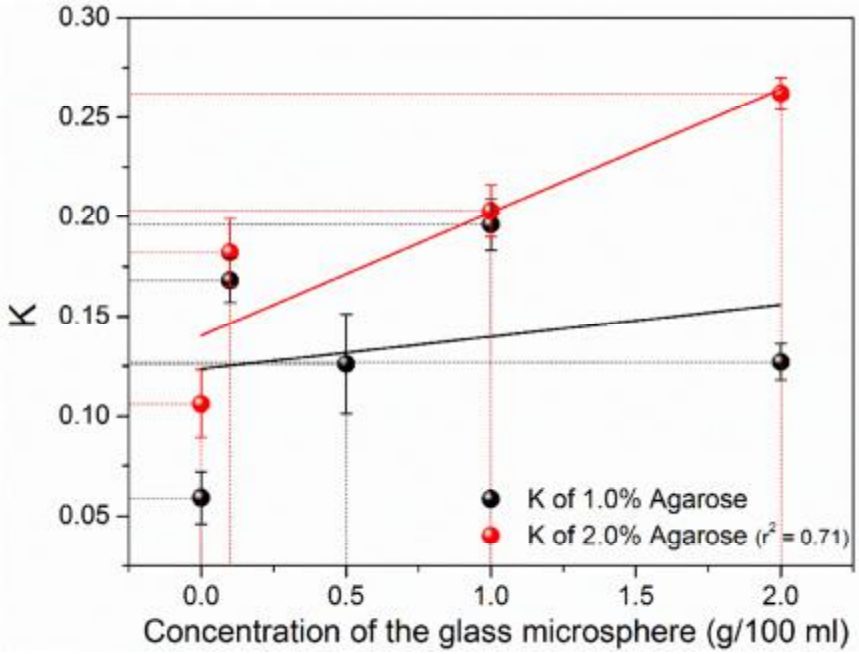

Figure 4.24. *K* as a function of gm for 1.0 and 2.0% agarose gel phantoms

As it is clearly seen, non-Gaussian diffusion is more pronounced for all agar gel phantoms than the agarose ones. This may be because of the fact that agarose, one of the two principal components of agar, forms thermos reversible gels consisting of thick bundles of agarose chains linked by hydrogen bonds, with large pores holding water. Water in the large pores tends to relax more slowly than water in small pores due to the different relative amounts surface and bulk water (Thus, T_1 and T_2 are longer than those of agar are). It is also stated that diffusion of particles in agarose gels (Fig 4.25, left) is anomalous, with a deviating fractal dimension of diffusion when large particles become entrapped in the pores of the gel (Narayanan et al., 2006; Fatin-Rouge et al., 2004; Ioannidis, 2009).

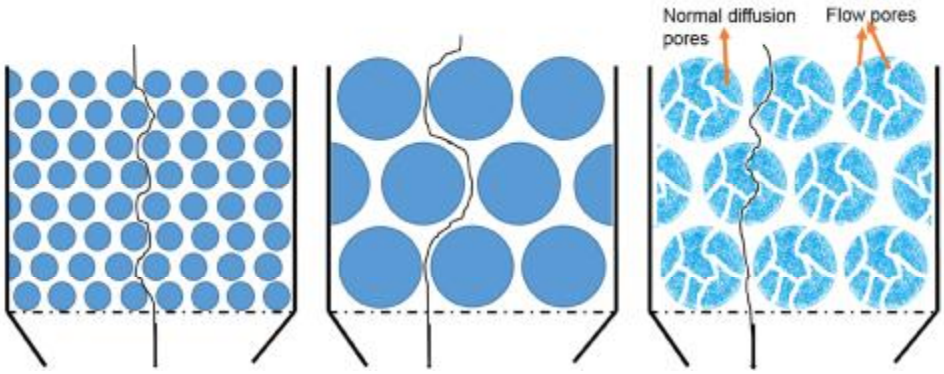

Figure 4.25. Comparison of small (right), large (middle), and large superporous (left) particles with short, long, and short diffusion, respectively (redrawn from Gustavsson and Larsson, 1996)

Agar is the dried hydrophilic, colloidal substance with a complex mixture of polysaccharides consisting of agarose and agaropectin as two major fractions. An agarose chain is a neutral alternating copolymer of β1,3-linked D-galactose and α-1,4-linked 3,6-anhydro-L-galactose. Agarose (including superporous particles) represents about two-thirds of the agar as the gelling fraction. (Zucca et al., 2016). Flow through the superpores (or flow pores) of agarose is governed by convection rather than diffusion (Ioannidis, 2009).

Thus, agar gel phantoms including gm in principle are promising materials for DKI with proper diffusive properties. When we examine the kurtosis in 2.0% agar gels including microspheres, it clearly increases in a linear fashion with the concentration of glass microspheres. A barrier concentration required giving a particular value of kurtosis may be evaluated (Fig 4.26).

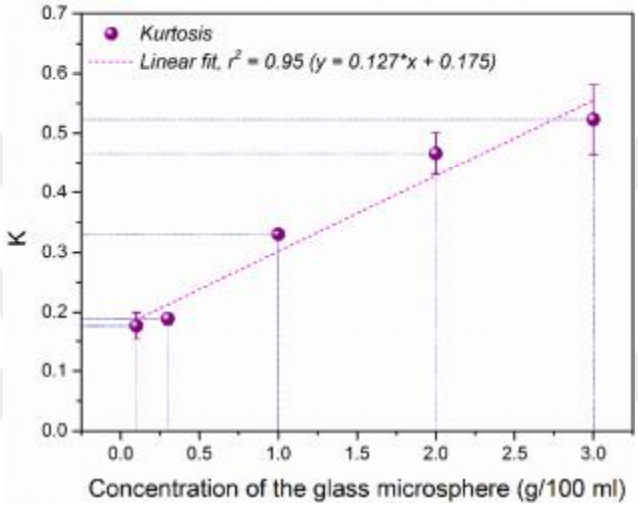

Figure 4.26. K as a function of gm concentration for the 2.0% agar gel phantoms

Thus, the linear fit relating kurtosis to microsphere concentration (C_{gm}) can be represented in Eq. 4.1.

$$K = \left(0.127\ x\ C_{gm}\right) + 0.175 \tag{4.1}$$

However, it is not correct to generalize this equation for all gm added 2.0% agar gel phantoms. As will be explained in detail in the following section, it is necessary to avoid inflated kurtosis values (pseudo-kurtosis) and to consider the noise floor. This equation only reflects the controlled values. The fact that 2.0% agar gel phantoms have results that are more successful by representing the highest kurtosis is emphasized here.

As mentioned in Chapter 1, kurtosis values for soft tissue reported in the literature are in the range of 0.34 – 0.65 and 0.22 – 1.05 for healthy and diseased tissue, respectively. Plain gels represent very low kurtosis with the maximum value of 0.216. However, kurtosis values for agar and agarose gels including gm are in the range of 0.177 – 0.523 and 0.126 – 0.289, respectively. As mentioned before, PVA-C gel phantoms cannot be interpreted in this section since both the structure is deteriorated by the addition of gm and the dehydration occurs rapidly even when the gels are stored in the refrigerator when not used. Thus, agar gel phantoms may easily represent a valuable range of healthy and diseased soft tissue.

4.4. Effects of Noise Floor Suppression on DW-MRI and DKI Data

4.4.1. Comparison of Diffusion Coefficients and Kurtosis

All plain and gm added 2.0% agar gel phantoms were scanned using different scanners (1.5 and 3T) and different protocols (vendor-suplied and modified ones) to compare diffusive properties in terms of various factors. $D_{(1)}$, $D_{(2)}$, and K results are presented in Table 4.13, 4.14, and 4.15, respectively.

Table 4.13. Comparison of $D_{(1)}$ values of plain and gm added agar gel phantoms according to the protocol used

Agar Gel Phantom (% w,v)	1.5T SS-SE-EPI (FOV 100)	3T SS-SE-EPI (FOV 100)	3T SE-ST (PGSE) (FOV 100)	3T SE-ST (PGSE) (FOV 64)
	$D_{(1)}$ ($\mu m^2/s$)			
1.0%	2008 ± 46	2201 ± 15	2184 ± 44	2081 ± 13
1.5%	1899 ± 39	2156 ± 9	2133 ± 43	2150 ± 18
2.0%	1947 ± 72	2127 ± 12	2134 ± 28	2174 ± 28
2.5%	1817 ± 48	2078 ± 13	2121 ± 61	2106 ± 22
3.0%	1802 ± 61	2042 ± 13	2078 ± 30	2089 ± 27
3.5%	1820 ± 98	2007 ± 18	2055 ± 39	2002 ± 30
2.0% + 0.1g gm	1815 ± 77	2037 ± 23	2066 ± 51	2106 ± 44
2.0% + 0.3g gm	1812 ± 84	1966 ± 34	1945 ± 137	2050 ± 35
2.0% + 1.0g gm	1408 ± 106	1462 ± 57	1498 ± 238	1407 ± 56
2.0% + 2.0g gm	767 ± 222	907 ± 226	986 ± 232	876 ± 192
2.0% + 3.0g gm	449 ± 191	852 ± 312	818 ± 233	684 ± 233

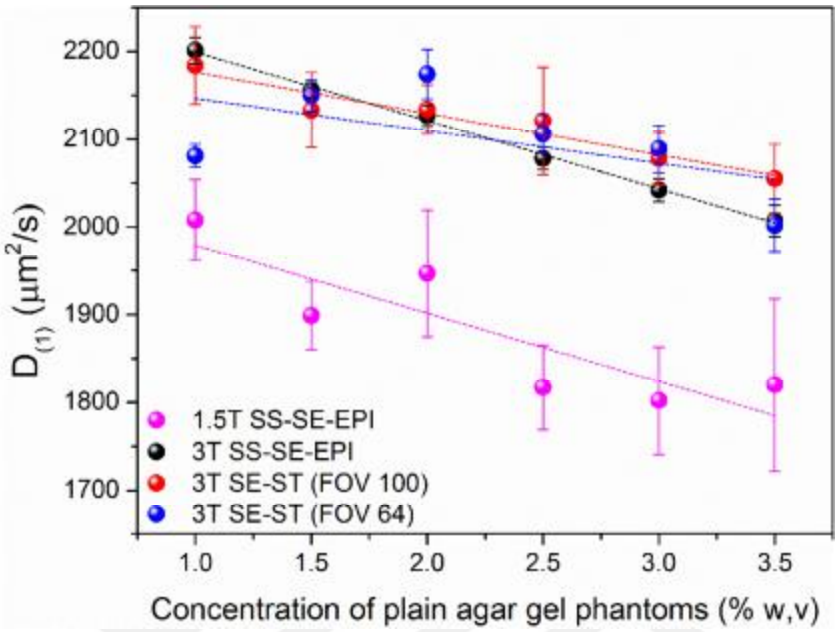

Figure 4.27. Comparison of $D_{(1)}$ values obtained by each protocol for plain agar gel phantoms

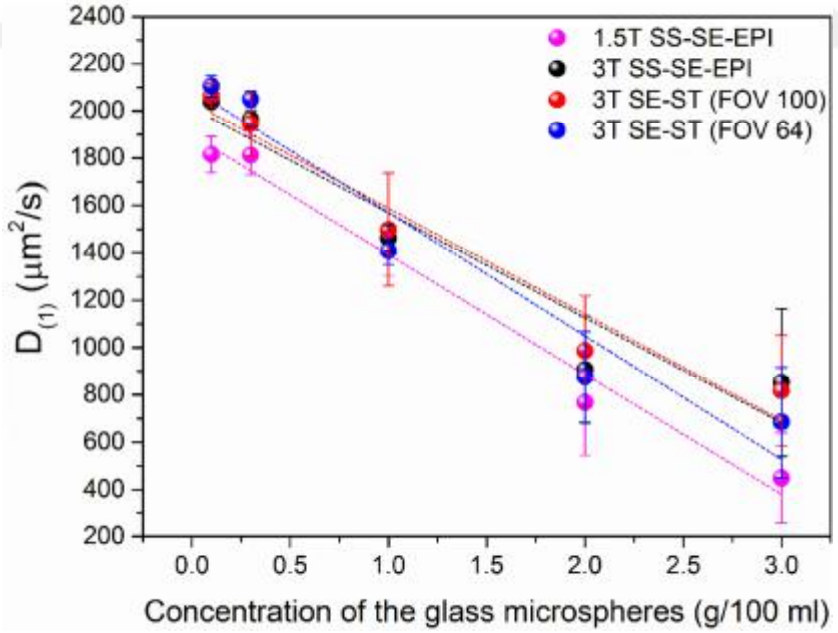

Figure 4.28. Comparison of $D_{(1)}$ values obtained by each protocol for 2.0% agar gel phantoms with gm

The dependence of the acquired diffusion coefficient $D_{(1)}$ achieved by monoexponential model with maximum b-value of 1500 s/mm^2 on the protocol used is summarized in Fig 4.27 and 4.28 for plain and 2.0% with gm agar gels, respectively. For increasing gel concentration, $D_{(1)}$ decreases in all applied protocols as shown in Fig 4.27. These decreases are expected however, $D_{(1)}$ obtained at 1.5T are lower. This case is similar for the $D_{(1)}$ values obtained by each protocol as the amount of added gm increases (Fig 4.28).

According to the EPI results, the percentage difference of the ADC ($D_{(1)}$) values are between 8.84 – 13.40 and 3.76 – 61.95 for plain and gm added 2.0% agar gel phantoms, respectively. In theory, the ADC ($D_{(1)}$) values should be independent of the field (Lavdas et al., 2014). However, 2.0% agar gel phantoms incluging gm in particular show significant differences in $D_{(1)}$ between field strengths. This might be explained by an increased noise floor bias due to lower SNR at 1.5T (Shaw et al., 2017). This situation will be explained in the following section in detail.

Table 4.14. Comparison of $D_{(2)}$ values of plain and gm added agar gel phantoms according to the protocol used

Agar Gel Phantom (% w,v)	1.5T SS-SE-EPI (FOV 100)	3T SS-SE-EPI (FOV 100)	3T SE-ST (PGSE) (FOV 100)	3T SE-ST (PGSE) (FOV 64)
	$D_{(2)}$ ($\mu m^2/s$)			
1.0%	2609 ± 165	2792 ± 149	2288 ± 90	2237 ± 91
1.5%	2379 ± 150	2660 ± 137	2308 ± 112	2359 ± 109
2.0%	2619 ± 185	2806 ± 147	2303 ± 91	2550 ± 156
2.5%	2336 ± 160	2635 ± 144	2329 ± 106	2377 ± 161
3.0%	2380 ± 158	2606 ± 142	2318 ± 157	2409 ± 162
3.5%	2478 ± 201	2635 ± 157	2694 ± 484	2343 ± 162
2.0% + 0.1g gm	2417 ± 185	2605 ± 141	2421 ± 204	2526 ± 207
2.0% + 0.3g gm	2417 ± 181	2460 ± 144	2215 ± 73	2406 ± 163
2.0% + 1.0g gm	1843 ± 193	1688 ± 112	1723 ± 101	1663 ± 123
2.0% + 2.0g gm	1077 ± 308	1113 ± 247	1115 ± 89	1121 ± 243
2.0% + 3.0g gm	662 ± 247	918 ± 273	898 ± 79	983 ± 302

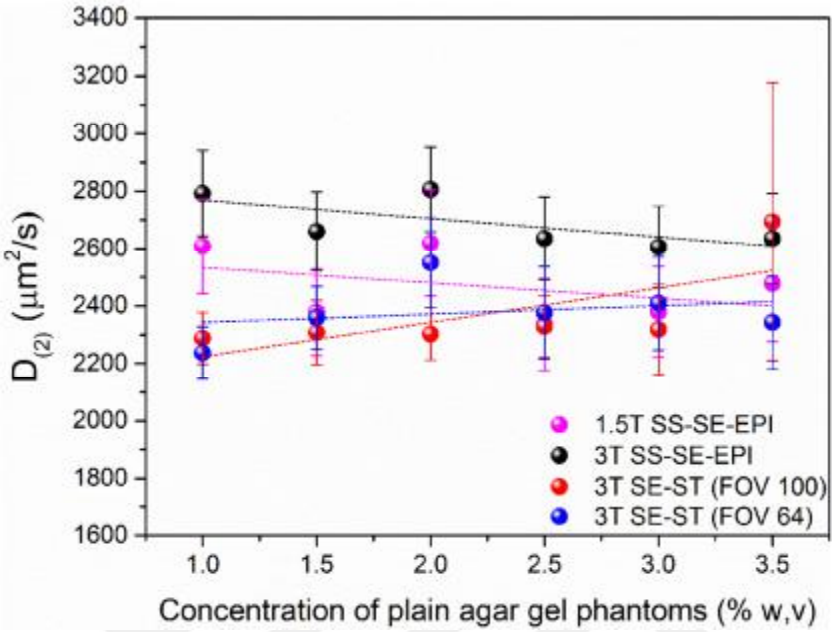

Figure 4.29. Comparison of $D_{(2)}$ values obtained by each protocol for plain agar gel phantoms

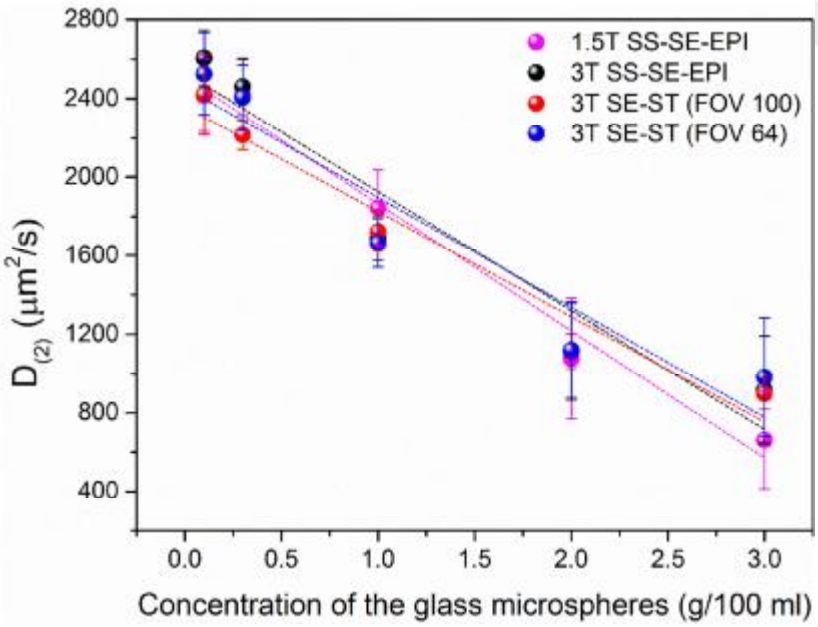

Figure 4.30. Comparison of $D_{(2)}$ values obtained by each protocol for 2.0% agar gel phantoms with gm

The dependence of the diffusion coefficient $D_{(2)}$ obtained by the kurtosis model with the higher b-values on the protocol used is summarized in Fig 4.29 and 4.30 for plain and 2.0% with gm agar gels, respectively. For increasing gel concentration, $D_{(2)}$ remains almost constant in all applied protocols as shown in Fig 4.29. However, $D_{(2)}$ decreases similar for each protocol as a function of gm concentration (Fig 4.30). Even though $D_{(2)}$ values and the relations between each other seen similar, it must be examined whether they are affected by the noise floor which occurs when high b-values are used as mentioned earlier.

Previously, it was emphasized that kurtosis values were expected in a sufficient range because the gel phantoms were designed and manufactured to represent a range of healthy and diseased tissues. It was mentioned that plain agar gel phantoms have very low kurtosis values observed in the modified ST-SE sequence and it is seen once again in Fig 4.31. However, vendor-suplied EPI redout results (especially those of 1.5T scanner) shows even higher *K* was obtained but once again, the Signal vs b-value plots must be evaluated to see whether these values are due to pseudo-kurtosis or not.

Table 4.15. Comparison of *K* values of plain and gm added agar gel phantoms according to the protocol used

Agar Gel Phantom (% w,v)	**1.5T SS-SE-EPI (FOV 100)**	**3T SS-SE-EPI (FOV 100)**	**3T SE-ST (PGSE) (FOV 100)**	**3T SE-ST (PGSE) (FOV 64)**
	K			
1.0%	0.286 ± 0.03	0.175 ± 0.02	0.050 ± 0.02	0.090 ± 0.04
1.5%	0.263 ± 0.05	0.167 ± 0.02	0.102 ± 0.02	0.114 ± 0.04
2.0%	0.350 ± 0.03	0.207 ± 0.02	0.094 ± 0.02	0.173 ± 0.04
2.5%	0.314 ± 0.04	0.197 ± 0.02	0.124 ± 0.02	0.144 ± 0.06
3.0%	0.348 ± 0.04	0.209 ± 0.02	0.126 ± 0.03	0.172 ± 0.05
3.5%	0.407 ± 0.03	0.232 ± 0.02	0.216 ± 0.03	0.191 ± 0.05
2.0% + 0.1g gm	0.374 ± 0.03	0.229 ± 0.02	0.177 ± 0.02	0.218 ± 0.06
2.0% + 0.3g gm	0.374 ± 0.03	0.232 ± 0.02	0.189 ± 0.01	0.206 ± 0.05
2.0% + 1.0g gm	0.491 ± 0.07	0.306 ± 0.04	0.330 ± 0.01	0.334 ± 0.06
2.0% + 2.0g gm	1.209 ± 6.00	0.562 ± 0.14	0.466 ± 0.04	0.591 ± 0.24
2.0% + 3.0g gm	2.081 ± 1.43	0.893 ± 0.33	0.523 ± 0.06	0.909 ± 0.40

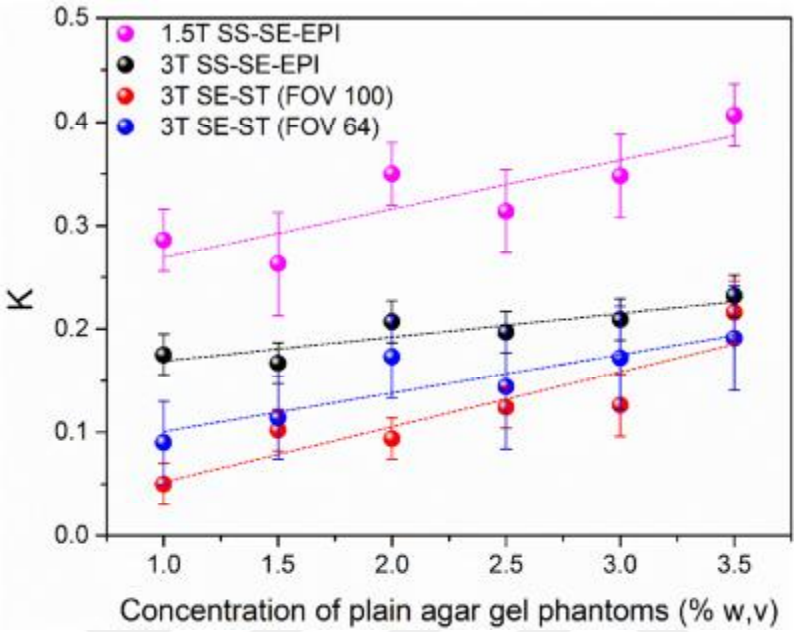

Figure 4.31. Comparison of *K* values obtained by each protocol for plain agar gel phantoms

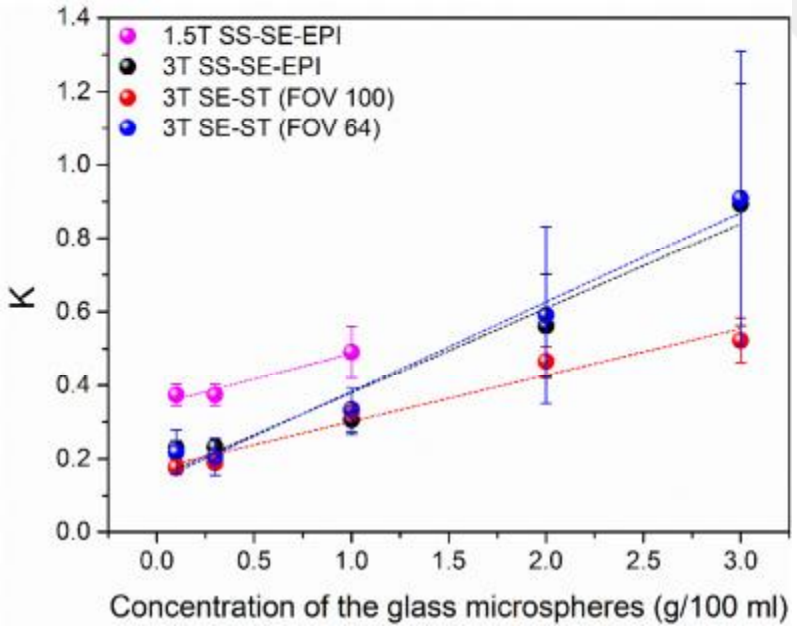

Figure 4.32. Comparison of *K* values obtained by each protocol for 2.0% agar gel phantoms with gm

In Fig 4.32, *K* results of 2 and 3g gm added 2.0% agar gel phantoms obtained by SS-SE-EPI protocol with 1.5T scanner are eliminated due to their odd values with extremely large SD values. However, it is seen that the current values shown are giving high results. In addition, other two protocols (in blue and black) give higher *K* than the one used in this study (in red). The much higher *K* values obtained with the 1.5T and 3T EPI sequence or smaller FOV require further investigation. Thus, both image quality and signal vs b-value plots of each phantom were examined and the results are presented in Sections 4.4.2 and 4.4.3.

4.4.2. Image Quality

Scanned images acquired with selected b-values of 0, 1000, 2000, 3000, and 4000 s/mm^2 are shown for 100 ml plain 2.0% agar gel phantom obtained by using each protocols in Fig 4.33. It is seen that the resulting b=0 and 1000 s/mm^2 images are almost free of distortions and signal losses for both manufacturers and different scan protocols. However, signal and the image quality begin to decrease at b=2000 s/mm^2 for the EPI readout at both field strenghts but mostly for 1.5T. There is almost no signal after b=3000 s/mm^2 for both manufacturers. When modified SE-ST scan protocols are analysed, it is clearly seen that distortions are lower than the SS-SE-EPI images at b=2000 s/mm^2 and the image quality is better. For the modified SE-ST protocol with FOV=100 mm, a signal can still be obtained even at b=4000 s/mm^2 while it is not visible for the one with FOV=64 mm.

Fig 4.34 represent the images of 100 ml 2.0% agar gel phantoms including 1g gm in the same format. As can be seen, the protocols applied in the 3T scanner provide better visual results than in the 1.5T scanner. SS-SE-EPI protocol applied in 1.5T scanner loses signal quality from b=2000 s/mm^2. Distortions are lower for those applied in 3T scanner and signal can be obtained even at b=4000 s/mm^2 for each. However, modified SE-ST protocol with FOV=100 mm represents the best image quality. Quantitative data is presented in Section 4.4.3.

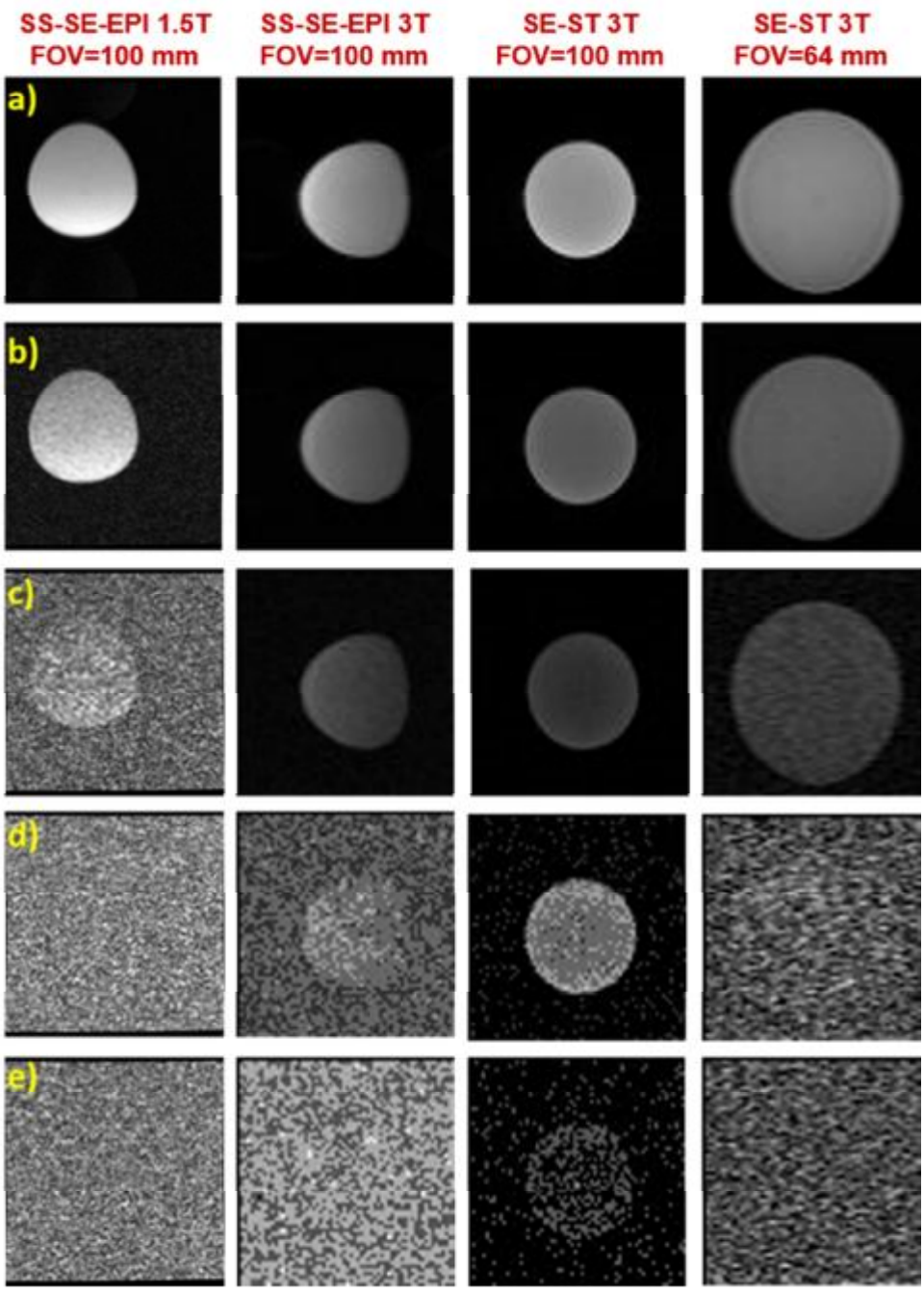

Figure 4.33. Images of plain 2.0% agar gel phantom vs b-values of a) 0, b) 1000, c) 2000, d) 3000, and e) 4000 s/mm^2

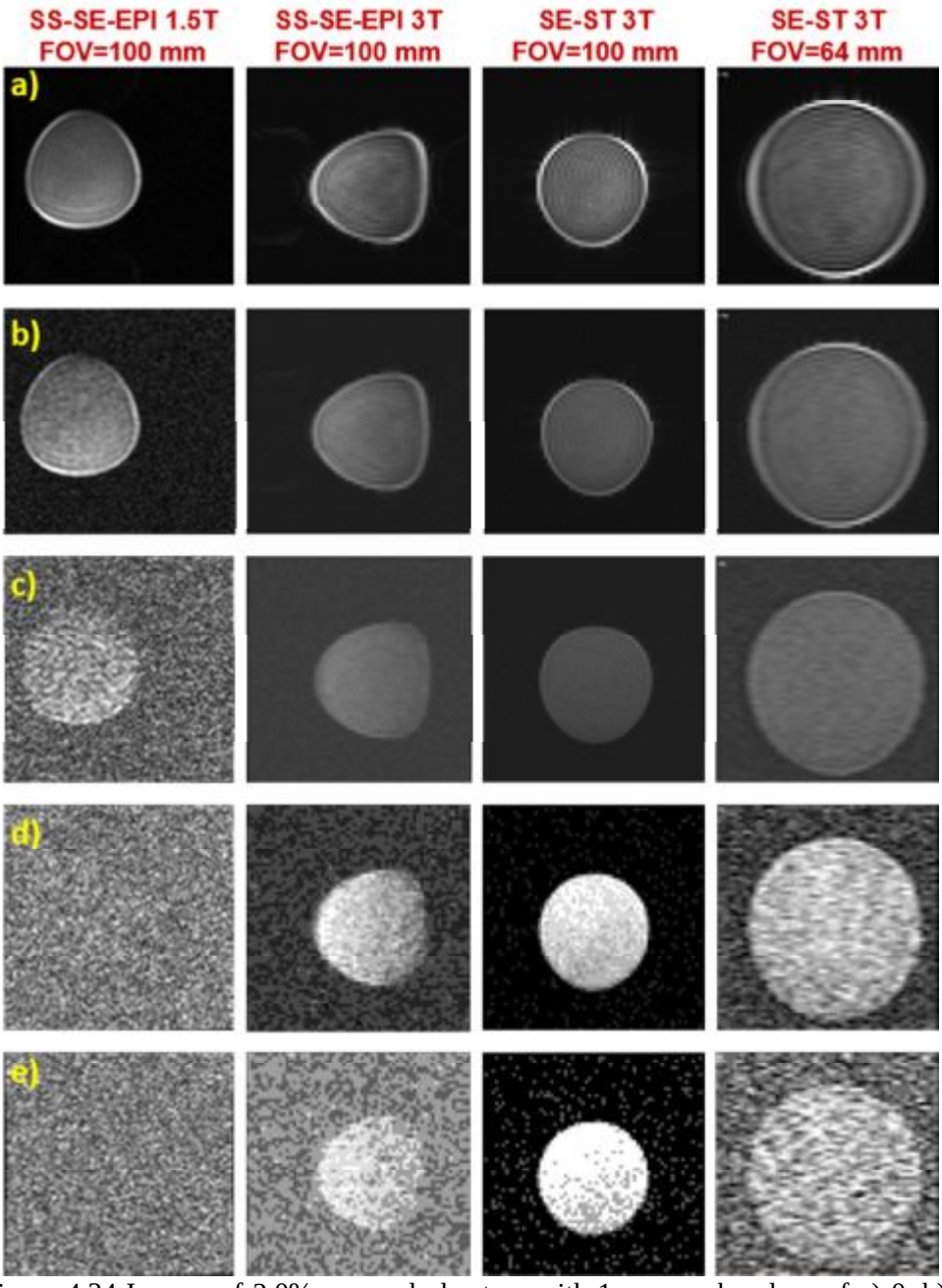

Figure 4.34 Images of 2.0% agar gel phantom with 1g gm vs b-values of a) 0, b) 1000, c) 2000, d) 3000, and e) 4000 s/mm^2

4.4.3. Noise Floor Suppression on the Signal

Signal values as a function of applied b-value were plotted including the excess noise floor by applying each protocol for all 6 plain and 5 gm added agar gel phantoms. Noise floors of each method are presented in Fig 4.35 and 4.36 for the samples of plain and 1g gm added 2.0% agar gel phantoms. In general, the modified SE-ST sequence shows a lower noise floor level than the SS-SE-EPI sequence for all phantoms. The plots obtained with the modified SE-ST sequence with FOV=100 mm have the highest quality in terms of SNR, artifacts, and distortion. The highest noise floor was obtained with SS-SE-EPI sequence applied by 1.5T scanner.

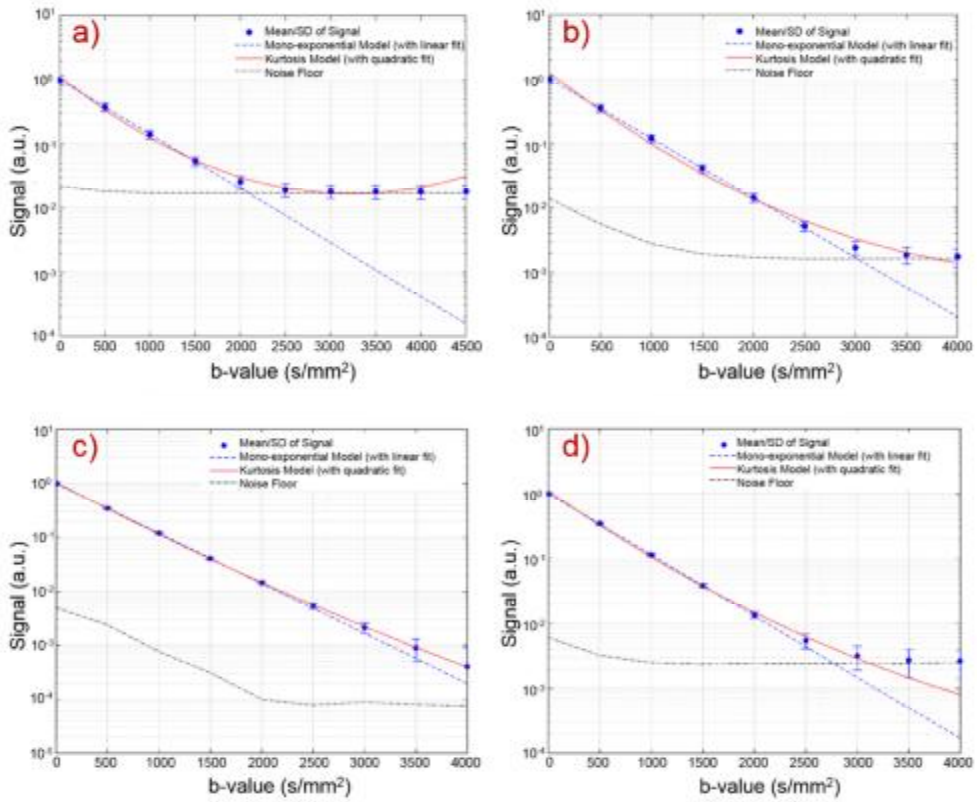

Figure 4.35. Signal vs b-value plots of plain 2.0% agar for a) SS-SE-EPI at 1.5T, b) SS-SE-EPI at 3T, c) modified SE-ST at 3T (FOV=100 mm), and d) modified SE-ST at 3T (FOV=64 mm)

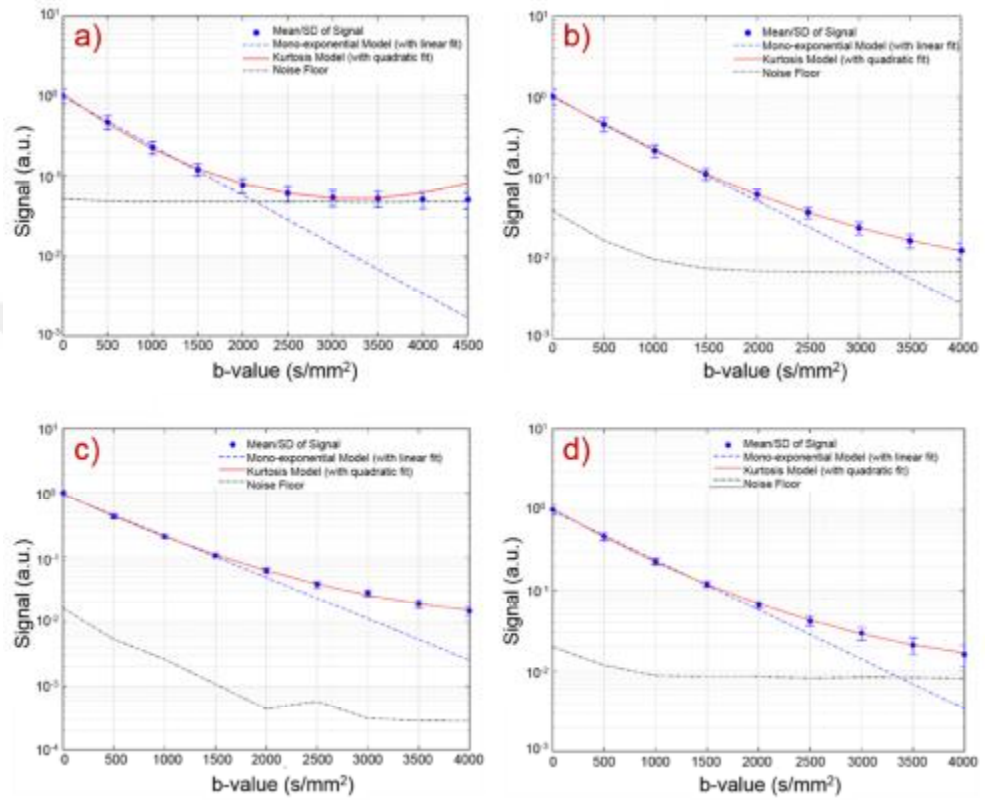

Figure 4.36. Signal vs b-value plots of 2.0% agar with 1g gm for a) SS-SE-EPI at 1.5T, b) SS-SE-EPI at 3T, c) modified SE-ST at 3T (FOV=100 mm), and d) modified SE-ST at 3T (FOV=64 mm)

The results shown in section 4.4.2 and 4.4.3 discuss in detail the accuracy of the results represented in section 4.4.1. Accordingly, the comparisons of the results are carried through the steps summarized below;

§ It was found that the noise floor is much higher in the 1.5T than 3T scanner when the same sequence (SS-SE-EPI) is applied for each sample. While $D_{(1)}$, calculated by using b_{max}=1500 s/mm^2, are free of

distortions for both manufacturers and field strengths, the signal begins to be affected by the noise floor from b=2000 s/mm^2 for 1.5T. Thus, the calculated $D_{(2)}$ and *K* are influenced by the noise and cannot represent the correct values. Therefore, *K* values presented in section 4.4.1 as the highest ones for both samples do not represent true values but are inflated by pseudo-kurtosis. In addition, there is no interaction with the noise floor for gm added agar gel phantom when the plain one is affected by the noise wall after b=3000 s/mm^2 in 3T scanner. Nevertheless, the confidence of the values of $D_{(2)}$ and K obtained for each sample without control should not be trusted. Two kinds of deduction can be made to correct the effect of pseudo-kurtosis. Either the diffusion parameters must be calculated be choosing b-values for which the signal is well above the noise floor or the noise correction is performed.

- The parameters for the vendor-supplied SS-SE-EPI sequences were chosen to be as the software permits. However, there are still some differences between them, which must be considered. The main differences are matrix size and slice differences. The matrix size is four times smaller while the slice thickness is half for the sequence used in the 3T scanner. As explained in Eq. 3.4 in Chapter 3, the difference between the protocols actually is not important because the effect that each factor has on the SNR compensate each other mathematically.
- When the same magnetic field strength (3T) was used, it is seen that signal obtained by modified SE-ST sequence is generally less affected by the noise floor than the signal obtained by vendor-suplied EPI redout. In addition, the signal for both samples remains well above the noise floor (background signal) for all b-values and thus we are more confident that the $D_{(2)}$ and *K* values obtained with this sequence are

accurate and not artificially inflated due to noise floor contamination.with modified SE-ST sequence with FOV=100 mm.

- Comparing both modified SE-ST protocols, the differences are FOV, matrix size, and slice thickness. Again, if we check the SNR equations, both the increase of FOV and slice thickness increases the SNR proportionally for the one with FOV = 100 mm. The decreasing effect of matrix size on SNR is lower than the other two factors due to its expression in the square root. Thus, the SNR and hence the image quality is much better.
- Acquisition time is another important issue especially in the clinic routine. The total time spent scanning gel phantoms with different protocols was reported as 6.45, 6.07, 27.81, and 11.97, respectively. Modified SE-ST sequence with 100 mm FOV has the most successful results but the longest time with only one N_A while, the sequences including vendor-suplied EPI readout show that the acquisition time is much shorter even they have multiple N_A, which is 8. Multiple slices can be composed in the same time without loss of higher b-value contrast for the SE sequence. With a repetition time of T_R = 3000 ms, it could be possible to squeeze in 15-20 slices before we need to increase the scan time even for the long T_E required for the large gradients. However, for the EPI sequence the length of the echo train and the need for multiple averages limit the number of slices that can be acquired concurrently. The crux of the study is to emphasize though is that we did not optimize the acquisition time, as the latter is irrelevant if there is no contrast at high-enough b-values to detect kurtosis.

The results of this study show that the use of b-values as high as possible would significantly enhance DKI. However, there are two limitations for this. First

is the interference from higher terms of diffusion, and the second one is the noise constrains of the scanners at high b-values.

As mentioned before, the b-value depends on the duration, strength and spacing of the puls gradients. In this thesis study, a larger b-value was achieved by increasing the gradient amplitude. SNR is reduced due to the application of larger diffusion gradients with the use of high b-values. This effect is lower in 3T system due to its greater diffusion sensitivity.

All signal vs b-value plots of the gel phantoms obtained using the modified SE-ST protocol with 100 mm FOV, represented in Figs 4.37 – 4.41, demonstrate that the signal is virtually unaffected by the noise floor.

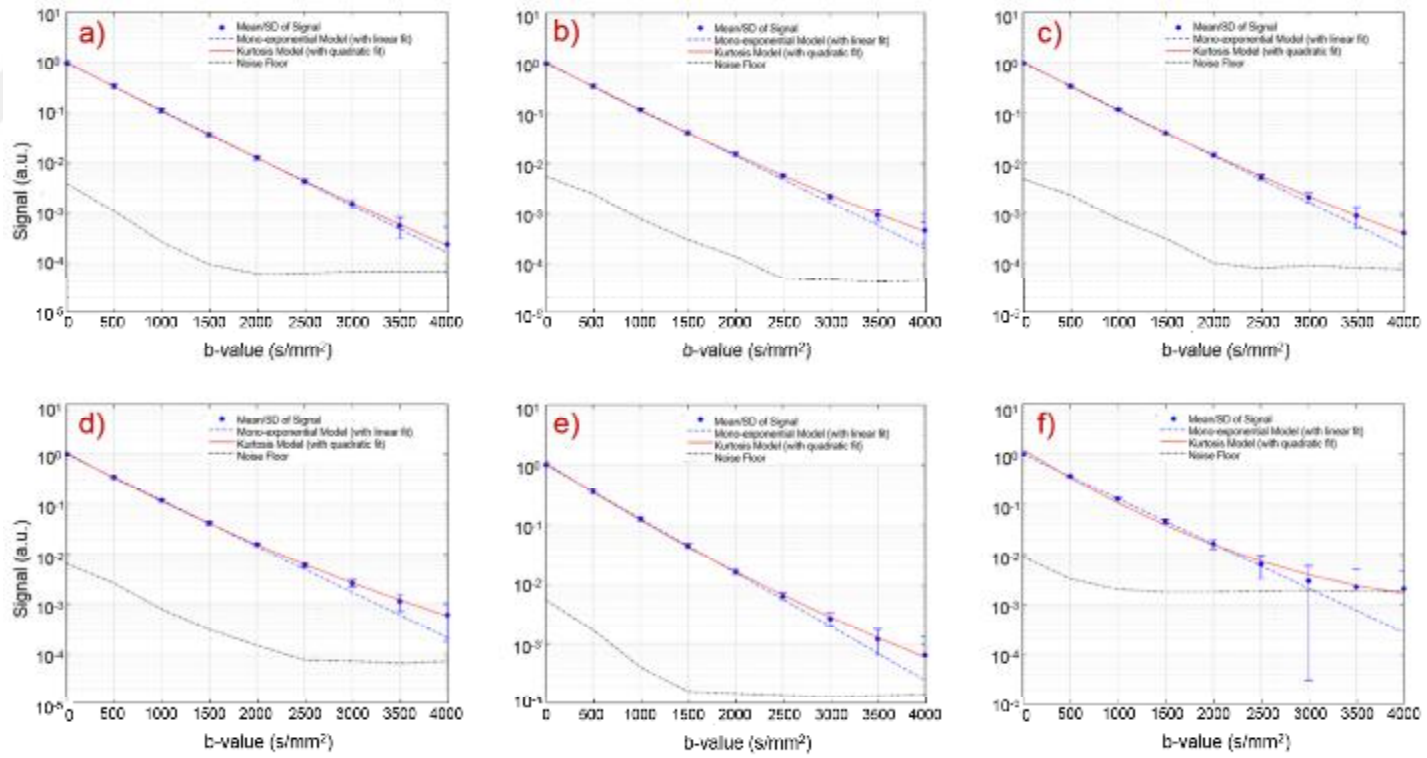

Figure 4.37. Signal vs b-value plots of a. 1.0, b. 1.5, c. 2.0, d. 2.5, e. 3.0, and f. 3.5 % plain agar gels using modified SE-ST (FOV=100 mm)

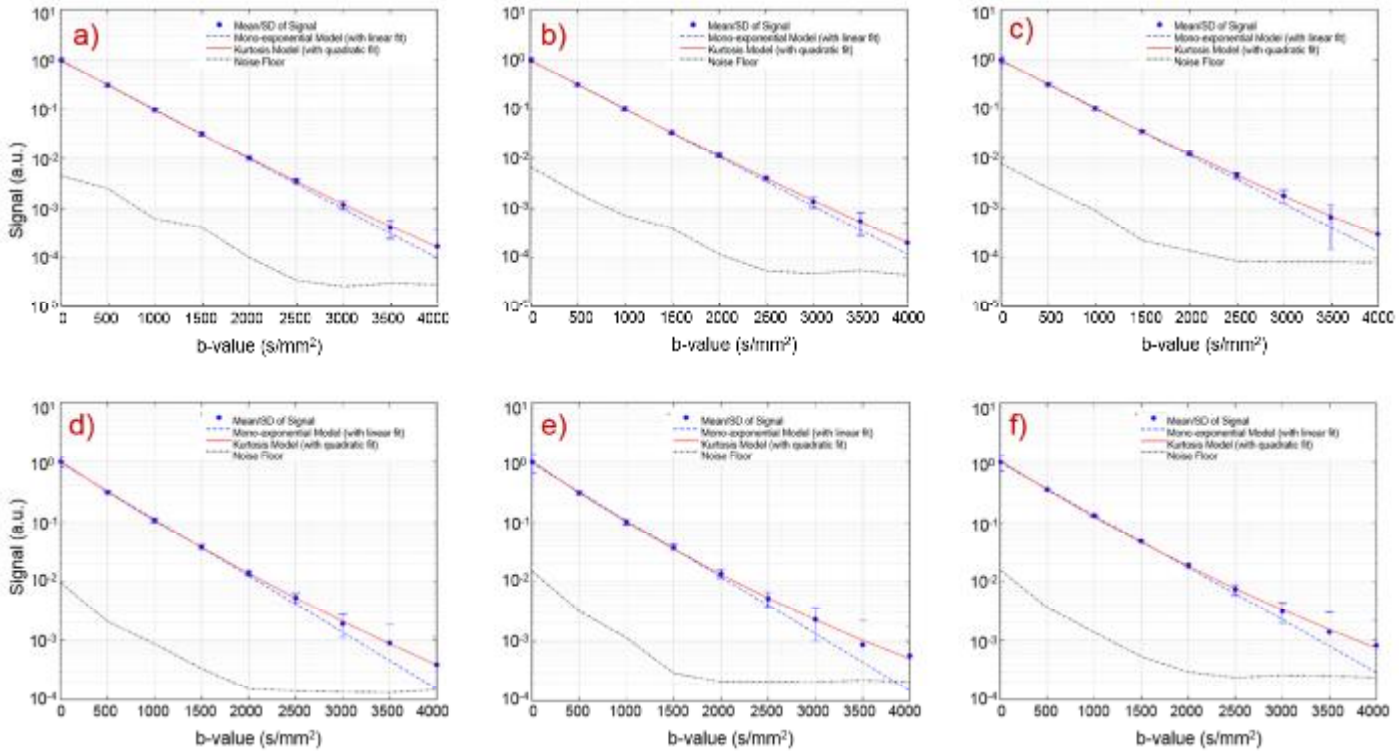

Figure 4.38. Signal vs b-value plots of a. 0.5, b. 1.0, c. 1.5, d. 2.0, e. 2.5, and f. 3.0 % plain agarose gels using modified SE-ST (FOV=100 mm)

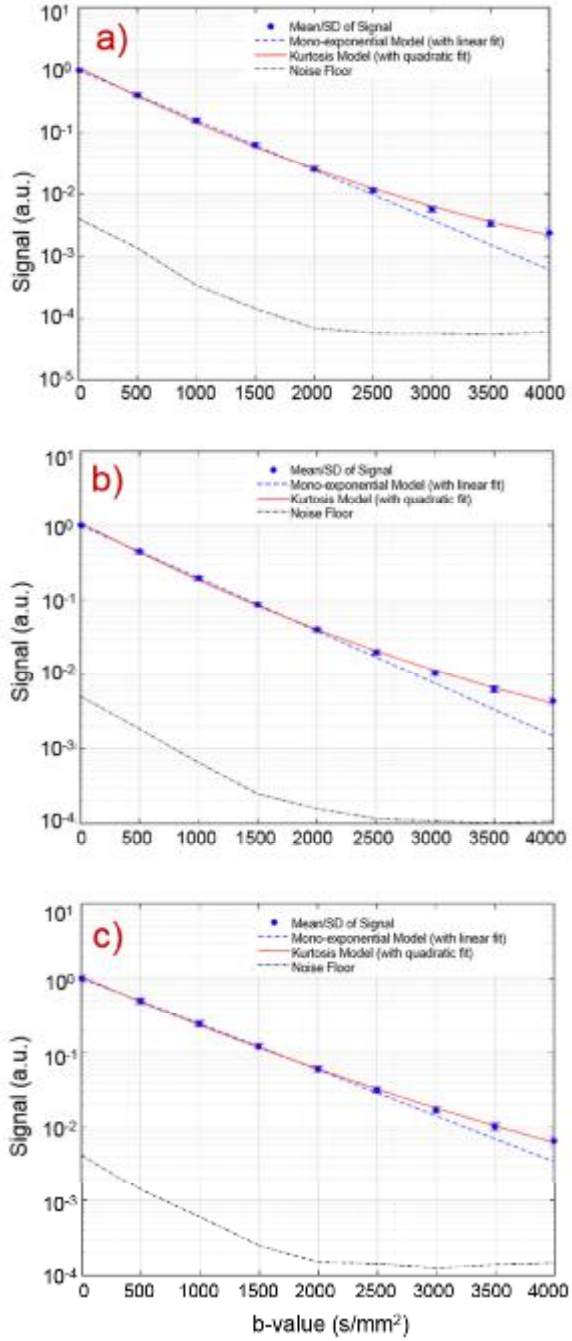

Figure 4.39. Signal vs b-value plots of a. 10.0, b. 15.0, and c. 20.0 % plain PVA-C gels using modified SE-ST (FOV=100 mm)

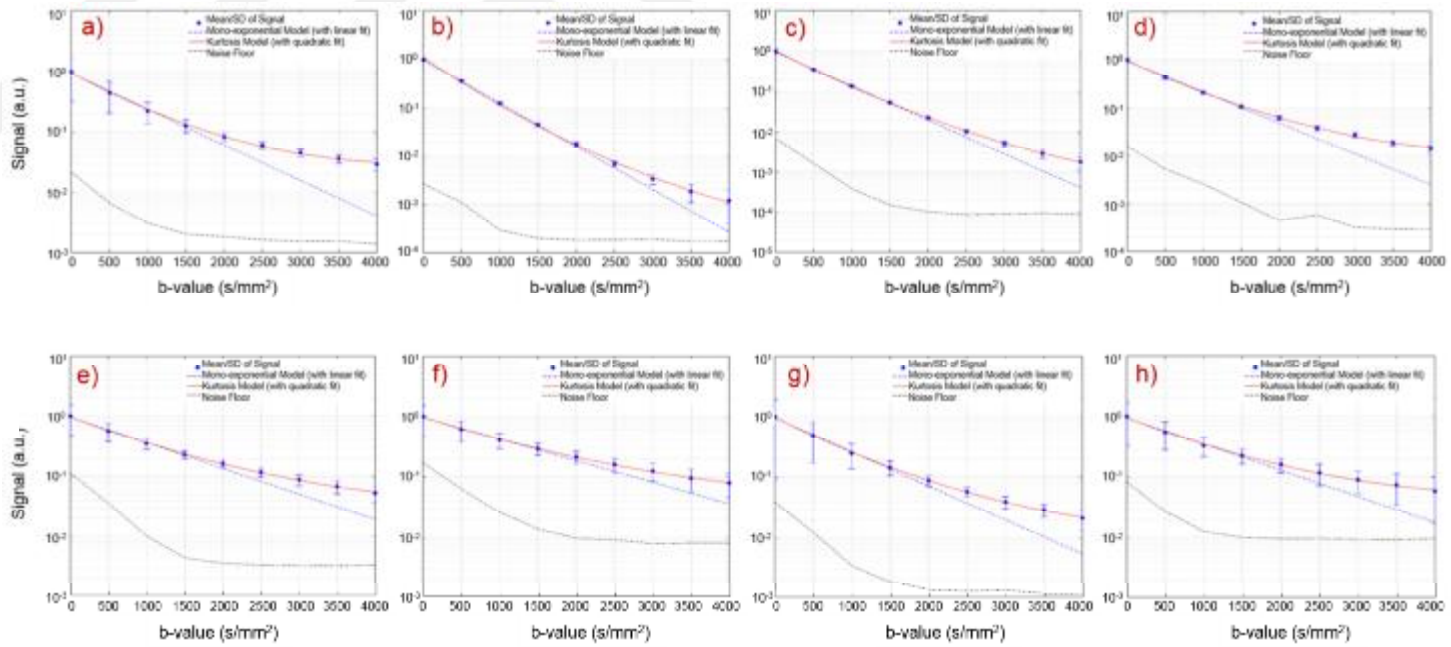

Figure 4.40. Signal vs b-value plots of a. 1.0% agar with 2g gm, b. 2.0% agar with 0.1g gm, c. 2.0% agar with 0.3g gm, d. 2.0% agar with 1g gm, e. 2.0% agar with 2g gm, f. 2.0% agar with 3g gm, g. 3.0% agar with 1g gm, and h. 3.0% agar with 2g gm using modified SE-ST (FOV=100 mm)

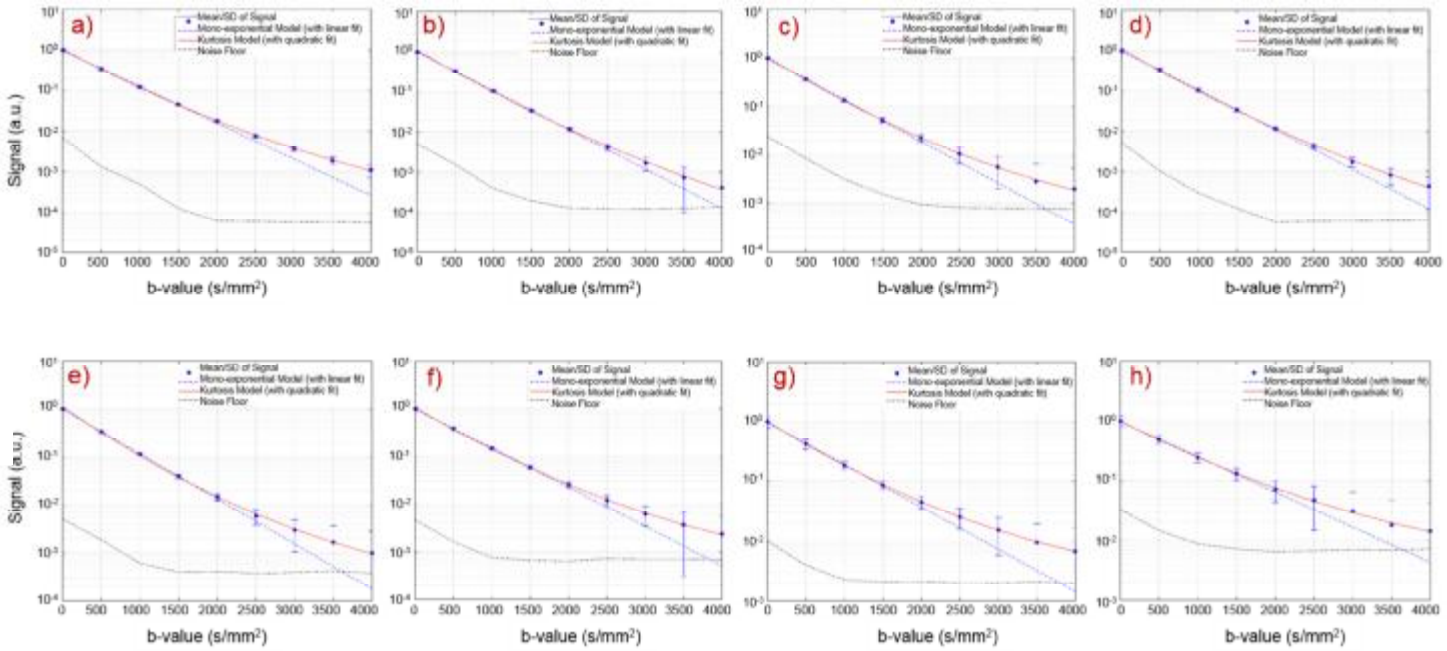

Figure 4.41. Signal vs b-value plots of a. 1.0% agarose with 0.1g gm, b. 1.0% agarose with 0.5g gm, c. 1.0% agarose with 1g gm, d. 1.0% agarose with 2g gm, e. 2.0% agarose with 0.1g gm, f. 2.0% agarose with 1g gm, g. 2.0% agarose with 2g gm, and h. 3.0% agarose with 1g gm using modified SE-ST (FOV=100 mm)

As seen in the figures, Our priority was to improve the accuracy of kurtosis estimates and minimize pseudo-kurtosis. The analysis of the results presented suggests the modified SE-ST sequence with a FOV of 100 mm was successful in achieving this aim, the only exception being the 3.5% plain agar, which proved challenging. This is an expected situation due to the viscous extracellular space.

It is emphasized in this thesis that the modified SE-ST is preferable to the vendor-supplied SS-SE-EPI sequences tested for the purpose of estimating kurtosis. Although the acquisition time is an issue for clinical applications, accuracy and reproducibility are crucial, as kurtosis value inflated by pseudo-kurtosis have no clinical value and could in fact lead to misadiagnosis. It may be possible to improve EPI readout sequences to reduce the effects of pseudo-kurtosis by optimization of the sequences and protocols, e.g., the use of carefully designed segmented EPI sequences to reduce acquisition times.

5. CONCLUSION AND FUTURE STUDIES

In this thesis, a gel phantom study was carried out for target volume optimization in HDR and/or LDR brachytherapy using advanced imaging techniques. Sequence development, protocol optimization, correct calibration, QA/QC are of great significance in terms of delivering radiation directly to the correct area during the treatment, which requires a detailed study. Phantoms are essential for QA, sequence testing and protocol development to minimize the effects of biological variability that is inevitable in patient and volunteer studies and avoid exposure of patients and volunteers to unnecesary risks. In addition, phantoms should be useful for each imaging modalities such as US, MRI and CT. Thus, gels were found to be the best option as phantoms as they are durable, robust, cost-effective, easy to manufacture and proper for multimodal imaging modalities.

To determine the best gelling agent and the concentration, two natural (agar and agarose) and the one synthetic (PVA) materials were used with various concentrations. A preservative material was used to prevent from bacterial growth and a test phantom prepared without preservative showed a formation two days after the preparation. In addition to pure, homogeneous gel phantoms, gels with glass microspheres to increase barrier concentration and heterogenous phantoms were created to achieve the aim of creating phantoms that are tissue-mimicking with regard to multiple MR relevant properties including kurtosis. Since, the purpose includes creating tissue mimicking (e.g. soft tissues) gel phantoms proper to use in various advanced imaging modalities to define target volume better for a successful BT treatment.

First, the gel phantoms prepared were characterized by using CT, US/Elastography, and MRI (relaxometry and diffusion studies). Second, a detailed DW-MRI and DKI analysis were conducted. Last, the importance of pseudo-kurtosis in DKI was investigated via protocol comparison.

The main conclusions can be summarized as follows:

I. Characterization of the Gel Phantoms

- While HU values of the agar and agarose gel phantoms are very low and close to the water, these values of plain agar and agarose gel phantoms are smilar to those of various lymph nodes which define breast cancer metastasis. HU values of the PVA-C phantoms are higher and the range is close to those of kidney, spleen, liver, and prostate. For the phantoms with gm, HU stayed almost constant for the agarose gels but decreased linearly to minus 100 (corresponding to fat tissue) for the agar gels when the concentration of microspheres was increased. Thus, a wide range of HU values were obtained that can represent different tissues. In addition, heterogeneous phantom could successfully be visualized.
- Preliminary data on the elasticity of the phantoms were collected by using shear wave and strain elastography modalities both qualitatively and quantitatively. These advanced US/Elastography imaging modalities are being increasingly developed and having a curicial place for the image-guided BT. Thus, it is important to evaluate prepared gel phantoms using them. The image qualities achieved were good for agar and PVA-C phantoms but less so for agarose-based gel pantoms. Thus, both gm added and heterogeneous gel phantoms were created using agar gelling agent due to the problem with preparing PVA-C with gm. Due to too high SDs of the elasticity values, the attention was given to the qualitative evaluation of the gel phantoms. Reasonably homogeneous images and excellent colour maps were obtained by both elastography techniques for the heterogeneous gel phantom.

- A relaxometry analysis was performed by using 3T MRI device to obtain further physical parameters, T_1 and T_2 relaxation times, of the gel phantoms. These parameters are also significant to demonstrate whether phantoms can mimic the tissue when MRI is used. It is found that all phantoms can represent soft tissue in terms of T_2 time. However, it is seen that T_1 times were found close to the soft tissue with agar and PVA-C gels but very different for agarose ones. Thus, it is emphasized that denser or more gm added agar phantoms may easily represent soft tissue.

II. DW-MRI and DKI Analysis

ADC ($D_{(1)}$) obtained from linear exponential fit (by Gaussian monoexponential model), $D_{(2)}$ and kurtosis K obtained from the quadratic exponential fit (by kurtosis model) of the data in DW-MRI show that $D_{(1)}$ is lower than $D_{(2)}$ for all gelling agents. $D_{(1)}$ decreases slightly with concentration of the gelling agent for all plain gel phantoms. However, $D_{(2)}$ remains almost constant for agar and agarose but decreases for PVA-C. In general, it is seen that the ADC ($D_{(1)}$) is lower than ($D_{(2)}$) when bigger b-values are used.

While plain gels were found to have low kurtosis values, we demonstrated that the kurtosis can be increased significantly by the addition of glass microspheres and controlled by varying the microsphere concentration without significant changes to the consistency, homogeneity or relaxometry properties of the phantoms.

Fig 5.1 displays the K, ADC ($D_{(1)}$), $D_{(2)}$ as a function of glass microsphere concentration. With the increase of the concentration, $D_{(1)}$ and $D_{(2)}$ converge suggesting that inclusion of the fourth moment is more significant at lower concentrations if a better estimate for the correct diffusion coefficient of the gel phantom is expected. $D_{(2)}$ is of great importance in DW-MRI and it is required to

assess $D_{(2)}$ over the widespread use of the ADC in clinical studies. Furthermore, the errors are generally lower for the $D_{(2)}$ values than the ADC values.

More restrictions to the water diffusion occur when the concentration of glass microspheres increases. Thus, kurtosis increases because the non-Gaussian character of the diffusion propagator increases. The SD of the pixels in the ROI, also increases for increasing concentration but only modareted. The reason is that acquisitions at higher b-values are needed to better approximate the quadratic fit of the signal attenuation at higher concentrations.

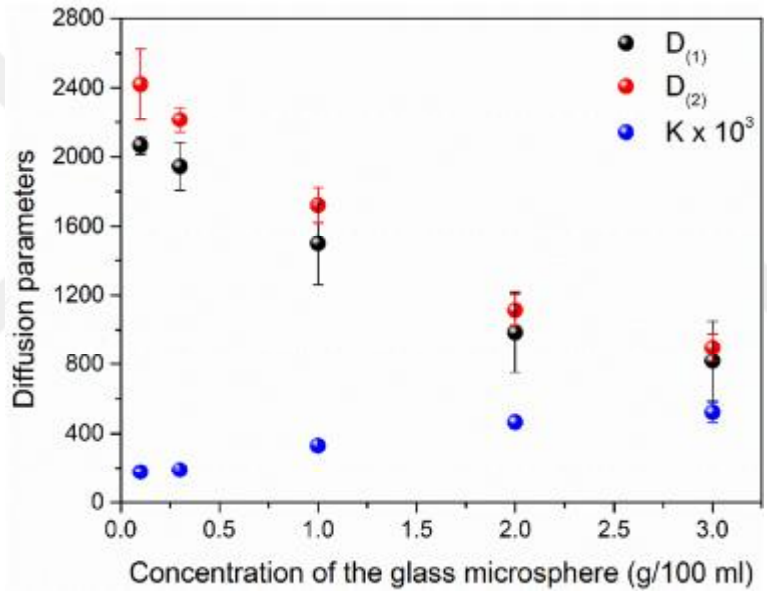

Figure 5.1. *K* (multiplied by 1000), $D_{(1)}$, and $D_{(2)}$ as a function of gm concentration

However, the possibility of fitting the noise floor could be problematic. Errors in measuring both $D_{(2)}$ and *K* will depend both on noise in the signal and in the choice of b-values.

III. DKI Protocol Comparion and Pseudo-Kurtosis Effect

It is presented the effect of noise floor fitting using gel phantoms for the assessment of isotropic diffusion kurtosis to investigate its potential in the optimization of target volume treated by LDR and/or HDR brachytherapy. We have shown that the rectified noise floor, which exists in standard magnitude data, increases the systematic error of the diffusion parameters. To minimize the impact of noise floor in DKI, high SNR at high b-values are needed. Although conventional readout is unfavourable compared to EPI in terms of acquisition times for single slice imaging, significant gains can be made for multi-slice imaging by interleaving the slices. Fast EPI results are useless if they are not accurate. A pseudo-kurtosis effect can be observed even in plain agar gel phantoms showing more free water diffusion than the ones with gm. It has been shown that the term K makes D more reliable however noise floor suppression must be taken into account.

Gel phantoms described in this work yields kurtosis values in the range $0 \leq K \leq 0.523$, covering a partial range of healthy and diseased soft tissues considered in the literature with the written modified ST-SE sequence. The work suggests that agar gel phantoms with glass microspheres in particular are promising materials for in-expensive but durable gel phantoms for DKI with tuneable diffusive and relaxometric properties. Tissue-mimicking DKI phantoms are an important tool to assess the diagnostic accuracy of DKI, e.g., for cancer patient screening, and to evaluate potential associations between DKI and other clinical parameters.

Future work includes the study of the effects of different types of glass microspheres and the design of more complex structured phantoms with non-isotropic, non-Gaussian diffusion for multimodal imaging to optimize target volume for the BT treatment. Multicenter studies of novel materials for DKI phantoms will be required to assess interplatform variability and establish reliable material characteristics. In addition, these gels are quite useful for further investigations in the developing imaging modalities such as MR Spectroscopy (MRS). Thus, next step may be to create a tissue-mimicking phantom (specific to a

tissue) appropriate for relaxometry, non-Gaussian diffusion imaging, and spectroscopy to investigate potential relationships between quantities accessible from multimodal MRI modalities by adding specific metabolite chemicals into the phantoms.

On the other hand, there are several strategies, which could potentially increase SNR of the image (i.e. higher field magnets, stronger gradients, better coils). Thus, acquisition time, which is also important factor in the clinic, could be optimized with further parameter tests.

BIBLIOGRAPHY

Ai, T., Morelli, J.N., Hu, X., Hao, D., Goerner, F.L., Ager, B., and Runge, V.M., 2012. A Historical Overview of Magnetic Resonance Imaging, Focusing on Technological Innovations. Invest Radiol, 47: 725–741.

Andre, E., 2014. Improvement of data quality for Diffusion Kurtosis Imaging and application to clinical neurological research. University of Liege and Maastricht University. PhD Thesis, Belgium and Netherlands, 121p.

Bammer, R., Holdsworth, S.J., Veldhuis, W.B., and Skare, S.T., 2009. New methods in diffusion weighted and diffusion tensor imaging. Magn Reson Imaging Clin N Am, 17:175–204.

Banerjee, S., Kataria, T., Gupta, D., Goyal, S., Bisht, S.S., Basu, T., and Abhishek, A., 2017. Use of ultrasound in image-guided high-dose-rate brachytherapy: enumerations and arguments. J Contemp Brachytherapy, 9(2):146–150.

Barr, R.G., Memo, R., and Schaub, C.R., 2012. Shear Wave ultrasound elastography of the prostate initial results. Ultrasound Quarterly, 28:13–20.

Barrett, T., McLean, M., Priest, A.N., Lawrance, E.M., Patterson, A.J., Koo, B.C., Patterson, I., Warren, A.Y., Doble, A., Gnanapragasam, V.J., Kastner, C., and Gallagher, F.A., (Epub ahead of print, 2017). Diagnostic evaluation of magnetization transfer and diffusion kurtosis imaging for prostate cancer detection in a re-biopsy population. Eur Radiol.

Bibic, A., 2006. Denoising of Complex MRI Data by Wiener-like Filtering in the Wavelet Domain: Application to High b-value Diffusion Weighted Imaging. Lund University. MSc Thesis, Sweeden, 30p.

Bitar, R., Leung, G., Perng, R., S. Tadros, Moody, A.R., Sarrazin, J., McGregor, C., Christakis, M., Symons, S., Nelson, A., and Roberts, T.P., 2006. MR Pulse Sequences: What Every Radiologist Wants to Know but Is Afraid to Ask. RadioGraphics, 26(2):513–537.

Brady, L.W., Combs, S.E., and Lu, J.J., 2016. Brachytherapy: An International Perspectice (P. Montemaggi, M. Trombetta, and L.W. Brady, Eds.), Springer International Publishing, Switzerland, 408p.

Brown, S., Bailey, D.L., Willowson, K., and Baldock, C., 2008. Investigation of the relationship between linear attenuation coefficients and CT Hounsfield units using radionuclides for SPECT. Applied Radiation and Isotopes, 66:1206–1212.

Cannon, L.M., Fagan, A.J., and Browne, J.E., 2011. Novel tissue mimicking materials for high frequency breast ultrasound phantoms. Ultrasound in Medicine and Biology, 37:122–135.

Cao, R., Huang, Z., Varghese, T., and Nabi, G., 2013. Tissue mimicking materials for the detection of prostate cancer using shear wave elastography: A validation study. Medikal Physics, 40(2):022903.

Constantinou, C., Harrington, J.C., and DeWerd, L.A., 1992. An electron density calibration phantom for CT-based treatment planning computers. Med Phys, 19:325–337.

Correas, J.M., Mejean, A., Helenon, O., and Bercoff, J., 2011. ShearWaveTM Elastography Prostate. Super Sonic Imagine, the Theragnostic Company, White Paper.

Cozzi, L., Fogliata, A., Buffa, F., and Bieri, S., 1998. Dosimetric impact of computed tomography calibration on a commercial treatment planning system for external radiation therapy. Radiother Oncol, 48:335–338.

Çelik, A. and Elmaoğlu, M., 2012. MRI Handbook: MR Physics, Patient Positioning, and Protocols. Springer, New York, USA, 318p.

D'Souza, W.D., Madsen, E.L., Unal, O., Vigen, K.K., Frank, G.R., and Thomadsen, B.R., 2001. Tissue mimicking materials for a multi-imaging modality prostate phantom. Medical Physics, 28(4):688–700.

Davis, B.J., Horwitz, E.M., Lee, W.R., Crook, J.M., Stock, R.G., Merrick, G.S., Butler, W.M., Grimm, P.D., Stone, N.N., Potters, L., Zietman, A.L., and Zelefsky, M.J., 2012. American brachytherapy society consensus guidelines for transrectal ultrasound-guided permanent prostate brachytherapy. Brachytherapy, 11:6–19.

De Bazelaire, C.M.J., Duhamel, G.D., Rofsky, N.M., and Alsop, D.C., 2004. MR Imaging Relaxation Times of Abdominal and Pelvic Tissues Measured in Vivo at 3.0 T: Preliminary Results. Radiology, 230:652–659.

De Brabandae, M., Kirisits, C., Peeters, R., Haustermans, K., and Van den Heuvel, F., 2006. Accuracy of seed reconstruction in prostate postplanning studied with a CT- and MRI-compatible phantom. Radiotherapy and Oncology, 79:190–197.

DeCarlo, L.T., 1997. On the meaning and use of kurtosis. Psychol Meth, 2:292–307.

Duboeuf, F., Basarab, A., Liebgott, H., Brusseau, E., Delachartre, P., and Vray, D., 2009. Investigation of PVA cryogel Young's modulus stability with time, controlled by a simple reliable technique. Medical Physics, 36:656–661.

Dwihapsari, Y., Sari, D.P., and Darminto, 2012. The Assessment of Consistency using Penetrometer and Apparent Diffusion Coefficient (ADC) Value using Diffusion Weighted Magnetic Resonance Imaging (DW-MRI) from Polyvinyl Alcohol (PVA) Formed by Freezing-Thawing Cycle. AIP Conf. Proc., 1454:53–56.

Earle, M., De Portu, G., and DeVos E., 2016. Agar ultrasound phantoms for low-cost training without refrigeration. African Journal of Emergency Medicine, 6:18–23.

Erickson, B.A., Demanes, D.J., Ibbott, G.S., Hayes, J.K., Hsu, I.C., Morris, D.E., Rabinovitch, R.A., Tward, J.D., and Rosenthal, S.A., 2011. American Society for Radiation Oncology (ASTRO) and American College of Radiology (ACR) practice guideline for the performance of high-dose-rate brachytherapy. Int. J. Radiat. Oncol., Biol., Phys., 79:641–649.

Farzaneh, F., Riederer, S.J., and Pelc, N.J., 1990. Analysis of T_2 limitations and offresonance effects on spatial resolution and artefacts in echo-planar imaging. Magn Reson Med, 14:123–139.

Fatin-Rouge, N., Starchev, K., and Buffle, J., 2004. Size Effects on Diffusion Processes within Agarose Gels. Biophysical Journal, 86:2710–2719.

Fieremans, E., Pires, A., and Jensen, J.H., 2012. A Simple Isotropic Phantom for Diffusional Kurtosis Imaging. Magnetic Resonance in Medicine 68:537–542.

Garcia, L., 2011. The assessment of tumour boundaries using ultrasound elastography. University of London. PhD Thesis, United Kingdom, 275p.

Gennisson, J.L., Deffieux, T., Fink, M., and Tanter, M., 2013. Ultrasound Elastography: Principles and Techniques. Diagnostic and Interventional Imaging, 94:487–495.

Ginat, D.T., Destounis, S.V., Barr, R.G., Castaneda, B., Strang, J.G., and Rubens, D.J., 2009. US Elastography of Breast and Prostate Lesions. Radiographics, 29(7):2007–2016.

Glenn, G.R., Tabesh, A., and Jensen, J.H., 2015. A Simple Noise Correction Scheme for Diffusional Kurtosis Imaging. Magn Reson Imaging, 33(1): 124–133.

Grebenkov, D.S., 2007. NMR survey of reflected Brownian motion. Rev. Mod. Phys., 79:1077.

Gustavsson, P.-E. and Larsson, P.-0, 1996. Superporous agarose, a new material for chromatography. Journal of Chromatography A, 743:231–240.

Hahn, E.L.,1950. Spin echoes. Phys. Rev., 80:580–594.

Hattori, K., Ikemoto, Y., Takao, W., Ohno, S., Harimoto, T., Kanazawa, S., Oita, M., Shibuya, K., Kuroda, M., and Kato, H., 2013. Development of MRI phantom equivalent to human tissues for 3.0-T MRI. Med Phys, 40:032303.

Holm, Å., 2013. Mathematical Optimization of HDR Brachytherapy. Linköping University. PhD Thesis, Sweden, 165p.

Hrinivich, W.T., 2017. Tools for improving high-dose-rate prostate cancer brachytherapy using three-dimensional ultrasound and magnetic resonance imaging. The University of Western Ontario. PhD Thesis, Canada, 191p.

Hu, N., Downey, D.B., Fenster, A., and Ladak, H.M., 2003. Prostate boundary segmentation from 3D ultrasound images. Medical Physics; 30:1648–1659.

Huber, J.S., Peng, Q., and Moses, W.W., 2010. Multi-modality Phantom Development. IEEE transactions on nuclear science, 56(5):2722–2727.

ICRU 38, 1985. Bethesda, MD: International Commision for Radiation Units and Measurements Report No. 38, Dose and Volume Specification for Reporting Intracavitary Therapy in Gynecology.

In, E., 2016. Development of Polymer-based Gels for Multimodal Medical Imaging Phantoms. University of Toronto. PhD Thesis, Canada. 122p.

Ioannidis, N., 2009. Manufacturing of Agarose-Based Chromatographic Media with Controlled Pore and Particle Size. The University of Birmingham. PhD Thesis, UK. 194p.

Jensen, J.H. and Helpern, J.A., 2010. MRI quantification of non-Gaussian water diffusion by kurtosis analysis. NMR in Biomedicine, 23:698–710.

Jensen, J.H., Helpern, J.A., Ramani, A., Lu, H., and Kaczynski, K., 2005. Diffusional Kurtosis Imaging: The Quantification of Non-Gaussian Water Diffusion by Means of Magnetic Resonance Imaging. Magnetic Resonance in Medicine, 53:1432–1440.

Jansen, J.F.A., Stambuk, H.E., Koutcher, J.A., and Shukla-Dave, A., 2010. Non-gaussian analysis of diffusion-weighted MR imaging in head and neck squamous cell carcinoa: a feasibility study. Am J Neuroradiol, 31:741–748.

Joslin, C.A., Flynn, A., and Hall, E.J., 2001. Principles and Practice of Brachytherapy: Using Afterloading Systems. Published by London, UK: Arnold (Hodder Headline Group)/New York, NY, USA: Oxford University Press Inc., 455p.

Lamba, R., McGahan, J.P., Corwin, M.T., Li, C.S., Tran, T., Seibert, J.A., and Boone, J.M., 2014. CT Hounsfield Numbers of Soft Tissues on Unenhanced Abdominal CT Scans: Variability Between Two Different Manufacturers' MDCT Scanners. AJR Am J Roentgenol., 203(5): 1013–1020.

Laubach, H.J., Jakob, P.M., Loevblad, K.O., Baird, A.E., Picone Bovo, M., Edelman, R.R., and Warach, S., 1998. Aphantom for Diffusion Weighted Imaging of Acute Stroke. JMRI, 8:1349–1354.

Lavdas, I., Behan, K.C., Papadaki, A., McRobbie, D.W., and Aboagye, E.O., 2013. A Phantom for Diffusion-Weighted MRI (DW-MRI). J. Mag. Reson. Imag. 38:173–179.

Lavdas, I., Miquel, M.E., McRobbie, D.W., and Aboagye, E.O., 2014. Comparison Between Diffusion-Weighted MRI (DW-MRI) at 1.5 and 3 Tesla: A Phantom Study. Journal of Magnetic Resonance Imaging, 40:682–690.

Le Bihan, D., 2013. Apparent diffusion coefficient and beyond: what diffusion MR imaging can tell us about tissue structure. Radiology, 268(2):318–322.

Lee, C.D., 2014. Recent developments and best practice in brachytherapy treatment planning. Br. J. Radiaol., 87(1041):20140146.

Lerner, R.M., Huang S.R., and Parker K.J., 1990. "Sonoelasticity" images derived from ultrasound signals in mechanically vibrated tissues. Ultrasound Med Biol, 16(3):231–239.

Marcon, P., Bartusek, K., and Cap, M., 2011. Sensitivity of the Diffusion Coefficients Measurement to Gradient Field Changes. PIERS Proceedings, Suzhou, China, 80–83.

McRobbie, D.W., Moore, E.A., Graves, M.J., and Prince, M.R., 2006. MRI from Picture to proton. 2nd Edition, Cambridge University Press, New York, USA, 393p.

Minati, L., and Weglarz, W.P., 2007. Physical foundations, models, and methods of diffusion magnetic resonance imaging of the brain: a review. Concepts Magn Reson A, 30A:278–307.

Narayanan, J., Xiong, J.Y., and Liu, X.Y., 2006. Determination of agarose gel pore size: Absorbance measurements vis a vis other techniques. Journal of Physics: Conference Series, 28:83–86.

Nath, R., 2005. Overview of Brachytherapy Physics (B. Thomadsen, M. Rivard, and W. Butler, Eds.). Brachytherapy Physics, 2nd Edition, Medical Physics Pub Corp, Madison, WI, 982p.

National Electrical Manufacturers Association (NEMA), 2001. Determination of signal-to-noise ratio (SNR) in diagnostic magnetic resonance imaging. NEMA Standards Publication MS 1-2001, p. 15.

Nogueira, L., Brandão, S., Matos, E., Nunes, R.G., Loureiro, J., Ramos, I., and Ferreira, H.A., 2014. Application of the diffusion kurtosis model for the study of breast lesions. Eur Radiol., 24:1197–1203.

Orsingher, L., Nocetti, L., and Crisi, G., 2016. DKI and pseudo-kurtosıs in phantoms. Abstracts/Physica Medica 32:e132.

Panagiotaki, E., Chan, R.W., Dikaios, N., Ahmed, H.U., O'Callaghan, J., Freeman, A., Atkinson, D., Punwani, S., Hawkes, D.J., and Alexander, D.C., 2015. Microstructural characterization of normal and malignant human prostate tissue with vascular, extracellular, and restricted diffusion for cytometry in tumours magnetic resonance imaging. Invest Radiol, 50(4):218–227.

Park, H., Kim, J.Y., Lee, B.M., Chang, S.K., Ko, S.Y., Kim, S.J., Park, D.S., and Shin, H.S., 2011. A comparison of preplan MRI and preplan CT-based prostate volume with intraoperative ultrasound-based prostate volume in real-time permanent brachytherapy. Radiat Oncol J, 29(3):199–205.

Phillips, J., and Charles-Edwards, G.D., 2015. A simple and robust test object for the assessment of isotropic diffusion kurtosis. Magn Reson Med., 73(5): 1844–1851.

Picard, J.C., Golshayan, A.R., Marshall, D.T., Opfermann, K.J., and Keane, T.E., 2012. The multi-disciplinary management of high-risk prostate cancer. Urologic Oncology: Seminars and Original Investigations, 30(1):3–15.

Portakal, Z.G., Shermer, S., Jenkins, C., Spezi, E., Perrett, T., Tuncel, N., and Phillips, J., 2018. Design and characterization of tissue-mimicking gel phantoms for diffusion kurtosis imaging. Medical Physics, 45(6):2476–2485.

Raab, P., Hattingen, E., Franz, K., Zanella, F.E., and Lanfermann, H., 2010. Cerebral gliomas: diffusional kurtosis imaging analysis of microstructural differences. Radiology, 254:876–881.

Rao, P.B. and Ghosh, S., 2015. Routine use of ultrasound guided tandem placement in intracavitary brachytherapy for the treatment of cervical cancer – a South Indian institutional experience. J Contemp Brachytherapy, 7: 352-356.

Rosenkrantz, A.B., Padhani, A.R., Chenevert, T.L., Koh, D.M., De Keyzer, F., Taouli, B., and Le Bihan, D., 2015. Body diffusion kurtosis imaging: basic principles, applications, and considerations for clinical practice. J. mag. Reson. Imaging, 42(5):1190–1202.

Rosenkrantz, A.B., Sigmund, E.E., Johnson, G., Babb, J.S., Mussi, T.C., Melamed, J., Taneja, S.S., Lee, V.S., and Jensen, J.H., 2012. Feasibility and Preliminary Experience of a Diffusional Kurtosis Model for Detection and Assessment of Aggressiveness of Peripheral Zone Cancer. Radiology, 264(1):126–135.

Rosenthal, S.A., Bittner, N.H., Beyer, D.C., Demanes, D.J., Goldsmith, B.J., Horwitz, E.M., Ibbott, G.S., Lee, W.R., Nag, S., Suh, W.W., and Potters, L, 2011. American Society for Radiation Oncology (ASTRO) and American College of Radiology (ACR) practice guideline for the transperineal permanent brachytherapy of prostate cancer. Int. J. Radiat. Oncol., Biol., Phys., 79:335–341.

Sack, I., Gedat, E., Bernarding, J., Buntkowsky, G., and Braun, J., 2004. Magnetic resonance elastography and diffusion-weighted imaging of the sol/gel phase transition in agarose. Journal of Magnetic Resonance, 166:252–261.

Scheel, M., Hubert, A., and Bartsch, A., 2015. C-1340: diffusion kurtosis imaging and pseudokurtosis in phantom studies. Eur Congr Radiol. , 1–8.

Seco, J. and Evans, P.M., 2006. Assessing the effect of electron density in photon dose calculations. Medical Physics, 33:540–552.

Shaw, C.B., Jensen, J.H., Deardorff, R.L., Spampinato, M.V., and Helpern, J.A., 2017. Comparison of Diffusion Metrics Obtained at 1.5T and 3T in Human Brain With Diffusional Kurtosis Imaging. Journal of Magnetic Resonance Imaging, 45:673–680.

Skrzyński, W., Zielinska-Dabrowska, S., Wachowicz, M., Slusarczyk-Kacprzyk, W., Kukołowicz, P.F., and Bulski, W., 2010. Computed Tomography as a Source of Electron Density Information for Radiation Treatment Planning. Strahlen ther Onkol, 186:327–333.

Stafford, R.J., Brezovich, I.A., and Orton, C.G., 2016. Image-guided prostate brachytherapy should be MRI-based. Med. Phys., 43(12):6213–6216.

Stanisz, G.J., Odrobina, E.E., Pun,J., Escaravage, M., Graham, S.J., Bronskill, M.J., and Henkelman, R.M., 2005. T_1, T_2 Relaxation and Magnetization Transfer in Tissue at 3T. Magnetic Resonance in Medicine, 54:507–512.

Stejskal, E.O. and Tanner, J.E., 1965. Spin diffusion measurements: Spin echoes in the presence of a time dependent field gradient. J Chem Phys, 42:288–292.

Sun, K., Chen, X., Chai, W., Fei, X., Fu, C., Yan, X., Zhan, Y., Chen, K., Shen, K., and Yan, F., 2015. Diffusion Kurtosis MR Imaging—Diagnostic Accuracy and Correlation with Clinical-Pathologic Factors. Radiology, 277(1):46–55.

Surry, K.J.M., Austin, H.J.B., Fenster, A., and Peters, T.M., 2004. Poly(vinyl alcohol) cryogel phantoms for use in ultrasound and MR imaging. Phys. Med. Biol., 49:5529–5546.

Tanderup, K., Viswanathan, A., Kirisits, C., and Frank, S.J., 2014. MRI-guided Brachytherapy. Semin Radiat Oncol., 24(3):181–191.

Tanner, J.E. and Stejskal, E.O., 1968. Restricted self-diffusion of protons in colloidal systems by pulse-gradient, spin-echo methods. J Chem Phys, 49:1768–1777.

Trampel, R., Jensen, J.H., Lee, R.F., Kamnetskiy, I., McGuinness, G., and Johnson, G., 2006. Diffusional Kurtosis Imaging in the Lung Using Hyperpolarized 3He. Magnetic Resonance in Medicine 56:733–737.

Twieg, D.B., 1983. The k-trajectory formulation of the NMR imaging process with applications in analysis and synthesis of imaging methods. Med Phys, 10:610–621.

Urata, M., Kijima, Y., Hirata, M., Shinden, Y., Arima, H., Nakajo, A., Koriyama, C., Arigami, T., Uenosono, Y., Okumura, H., Maemura, K., Ishigami, S., Yoshinaka, H., and Natsugoe, S., 2014. Computed tomography Hounsfield units can predict breast cancer metastasis to axillary lymph nodes. BMC Cancer, 14:730.

Wang, P., Thapa, D., Wu, G., Sun, Q., Cai, H., and Tuo, F., 2018. A study on diffusion and kurtosis features of cervical cancer based on non-Gaussian diffusion weighted model. Magnetic Resonance Imaging, 47:60–66.

Web1,http://www.aboutcancer.com/intracavitary_radiation_treatments.htm, Access time: 08.07.2018.

Web2,https://www.mayoclinic.org/tests-procedures/brachytherapy/multimedia/interstitial-brachytherapy/img-20006362, Access time: 08.07.2018.

Web3,http://biyomedikalmuhendislik.com/wp-content/uploads/2014/10/mr-manyetik-rezonans.pdf, Access time: 12.07.2018.

Web4, https://www.healthcare.siemens.com/, Access time: 30.07.2018.

Web5, http://www.ismrm.org/smrt/chapters/southcarolina/SC2011MR05.pdf, Access time: 13.08.2018.

Web6, https://www.k-space.org/ymk/eq_snr.pdf, Access time: 13.08.2018.

Web7, http://www3.gehealthcare.com/, Access time: 30.07.2018.

Web8, http://mri-q.com, Access time: 09.08.2018.

Yang, J., Xing, L., Pope, C., and Li, Z, 2016. Physics: Low-Energy Brachytherapy Physics (P. Montemaggi, M. Trombetta, and L.W. Brady, Eds.). Brachytherapy: An International Perspectice, Springer International Publishing, Switzerland, p30–31.

Zhai, L., Madden, J., Foo, W.-C., Mouraviev, V., Polascik, T.J., Palmeri, M.L., and Nightingale K.R., 2010. Characterizing stiffness of human prostates using acoustic radiation force. Ultrason. Imaging, 32:201–213.

Zhang, M., Nigwekar, P., Castaneda, B., Hoyt, K., Joseph, J.V., Agnese, A.d.S., Messing, E.M., Strang, J.G., Rubens, D.J., and Parker, K.J., 2008. Quantitative characterization of viscoelastic properties of human prostate correlated with histology. Ultrasound Med. Biol., 34:1033–1042.

Zucca, P., Fernandez-Lafuente, R., and Sanjust, E., 2016. Agarose and Its Derivatives as Supports for Enzyme Immobilization. Molecules, 21:1577.

CURRICULUM VITAE

Ziyafer Gizem Portakal was born on 3rd of September 1986 in İzmir. She studied Physics Education at Dokuz Eylül University in İzmir and received her diploma in 2009 with both B.Sc. and M.Sc. degrees. Then, she started her undergraduate studies at Ege University, Institute of Nuclear Sciences, and Department of Nuclear Technologies in September 2009. After successfully passing the lecture period, she started her thesis phase but continued to study in the Physics Department at Çukurova University when she was entitled to be a Research Assistant there in September 2010. During her M.Sc., she worked as a radiation physicist at Çukurova University, Faculty of Medicine, and Department of Radiation Oncology between October 2010 and June 2012 and graduated from M.Sc. in July 2012. After starting her Ph.D. at Physics Department in September 2012, she went to Medizinischen Fakultät Mannheim der Ruprecht-Karls-Universität Heidelberg, Mannheim, Germany with Erasmus internship mobility program and worked as an IMRT physicist for 4 months. She also dealed with EBT3 Gafchromic film project. After returning, she completed the course phase and started to thesis phase in 2014. She performed the major part of the thesis at Velindre Cancer Centre and Institute of Life Science at Swansea University in Wales, UK between April 2015 and March 2016. She has gained experience by working on brachytherapy, US/Elastography and MRI. Her research areas are radiation physics, medical physics, medical imaging, and dosimetry. In particular, she is working on dosimetry for both medical and environmental purposes.